Generation and characterization of a mouse model for the achalasia, alacrima and mental retardation (AAMR) syndrome

Dissertation

zur Erlangung des akademischen Grades

doctor rerum naturalium (Dr. rer. nat.)

vorgelegt dem Rat der Medizinischen Fakultät

der Friedrich-Schiller-Universität Jena

von Patricia Franzka (Master Biochemistry)

geboren am 24.06.1987 in Berlin, Deutschland

Gutachter

1. Prof. Dr. Christian Hübner

    Institute of Human Genetics, University Hospital Jena, Germany

2. Prof. Dr. Emile van Schaftingen, Université Catolique de Louvain,

    Bruxelles, Belgium

    Institute of Human Genetics, University Hospital Jena, Germany

3. Prof. Dr. Rüdiger Horstkorte

    Institute of Physiological Chemistry, University Halle, Germany

Tag der öffentlichen Verteidigung: 03.03.2020

Table of contents

Abbreviations

α	Alpha
aCSF	Artificial cerebrospinal fluid
AAMR	Achalasia, alacrima, mental retardation
ALG6	α-1,3-glucosyltransferase
Asn	Asparagine
β	Beta
bFGF	Basic fibroblast growth factor
BIP	Binding immunoglobulin protein
BTX	Bungarotoxin
CA	Cornu ammonis
$CaCl_2$	Calcium chloride
CAPZB	Capping actin protein of muscle Z-disc β subunit
CDG	Congenital disorder of glycosylation
CHX	Cycloheximide
CMD	Congenital muscular dystrophy
CO_2	Carbon dioxide
COG	Conserved oligomeric golgi
Con A	Concanavalin A
COS-7	CV-1 in Origin, carrying SV40
Cre	Causes recombination
DAG1	Dystroglycan (precursor protein)
dATP	Deoxyadenosine triphosphate
DG	Dystroglycan
dGTP	Deoxyguanosine triphosphate
DMSO	Dimethyl sulfoxide
DNA	Deoxyribonucleic acid
dNTP	Deoxynucleotide triphosphate
Dol-PP-GlcNAc2Man5	Dolichol-diphosphate-di-*N*-acetylglucosamine-penta-mannose
Dol-PP-Glc*N*Ac2Man9Glc3	Dolichol-diphosphate-di-*N*-acetylglucosamine-nona-mannose-tri-glucose
DPM	Dolichol-phosphate-mannose synthase
DTT	Dithiothreitol
dTTP	Deoxythymidine triphosphate
ECM	Extracellular matrix

EDTA	Ethylenediaminetetraacetic acid
ECL	Enhanced chemiluminiscence
EM	Electron microscopy
ER	Endoplasmic reticulum
ERK	Extracellular-signal regulated kinase
FBA	Foot base angle
fEPSPs	Field excitatory postsynaptic potentials
Flpe	Flippase
FS	First-strand
FKRP	Fukutin-related protein
GalNAc	*N*-acetylgalactosamine
GAPDH	Glyceraldehyde 3-phosphate dehydrogenase
GDP	Guanosine diphosphate
GFAP	Glial fibrillary acid protein
GlcNAc	*N*-acetylglucosamine
GlcNAcT-1	*N*-acetylglucosaminyltransferase 1
GlcNAcT-2	*N*-acetylglucosaminyltransferase 2
GLG1	Golgi glycoprotein 1
GM130	Golgi matrix protein 130
GMPPA	Guanosine-diphosphate-mannose pyrophosphorylase A
GMPPB	Guanosine-diphosphate-mannose pyrophosphorylase B
GPI	Glycosyl-phosphatidylinositol
GRB2	Growth factor receptor-bound protein 2
GST	Glutathione S-transferase
GTP	Guanosine triphosphate
HCl	Hydrochloric acid
HE	Hematoxylin/eosin
HEK	Human embryonic kidney
HEPES	4-(2-hydroxyethyl)-1-piperazineethanesulfonic acid
HFS	Half-maximal intensity
His	Histidine
H_2O	Water
HS	Horse serum
IAA	Iodoacetamide

IF	Immunofluorescence
IgG	Immunoglobuline G
IgM	Immunoglobuline M
IP	Immunoprecipitation
KCl	Potassium chloride
KDN	2-keto-3-deoxy-D-glycero-D-galacto-nononic acid
KO	Knockout
LacZ	β-D-galactosidase
LARGE	Like-acetylglucosaminyltransferase
LB	Lysogeny broth
Lys	Lysine
LTP	Long-term potentiation
MALDI-TOF	Matrix-assisted laser desorption/ionization time of flight
MBP	Maltose binding protein
MEB	Muscle-eye-brain disease
$MgSO_4$	Magnesium sulfate
$MnCl_2$	Manganese chloride
MOPS	3-(N-morpholino)-propanesulfonic acid
MPI	Mannose-6-phosphate-isomerase
MUSK	Muscle-specific kinase
NaCl	Sodium chloride
$NaHCO_3$	Sodium bicarbonate
NaH_2PO_4	Monosodium phosphate
NaOH	Sodium hydroxide
NF200	Neurofilament 200
NMJ	Neuromuscular junction
O_2	Oxygen
OST	Oligosaccharyltransferase
P	Penicillin
P-	Phosphate
PBS	Phosphate buffered saline
PCR	Polymerase chain reaction
PEG	Polyethylene glycol
PFA	Paraformaldehyde
PLA	Proximity ligation assay

PMM2	Phosphomannomutase 2
PNA	Peanut agglutinin
POMGnT1/ 2	Protein-*O*-mannose-β1,4-*N*-acetylglucosaminyltransferase 1 and 2
POMT 1/ 2	Protein *O*-mannosyltransferases 1 and 2
Pro	Proline
PVDF	Polyvinylidene fluoride
qPCR	Quantitative PCR
RbCl	Rubidium chloride
RNA	Ribonucleic acid
RSC1A1	Regulator of solute carriers 1
RT	Room temperature
S	Streptomycin
SDS	Sodium dodecyl sulfate
Ser	Serine
siScr	Scrambled siRNA
SSPE	Sodium chloride-sodium phosphate-EDTA
TAE	Tris-acetate-EDTA
TBS	Tris-buffered saline
TE	Tris-EDTA
TGN38	Trans-Golgi network integral membrane protein 38
Thr	Threonine
Tyr	Tyrosine
UV	Ultraviolet
WGA	Wheat germ agglutinin
WT	Wild-type
WWS	Walker-Warburg-syndrome

Summary

The AAMR syndrome is characterized by mental retardation and gait abnormalities as well as achalasia and alacrima. This disorder is inherited as an autosomal recessive trait and is caused by mutations in the *Guanosine-diphosphate-(GDP)-mannose-pyrophosphorylase A* (*GMPPA*) gene. *GMPPA* encodes the 420 aa protein GMPPA. Its homolog, the GDP-mannose-pyrophosphorylase B (GMPPB), converts mannose-1-phosphate and guanosine triphosphate (GTP) to GDP-mannose, which is an essential substrate for glycosylation. Up to date, 18 patients with inactivating mutations in the *GMPPA* gene have been reported worldwide.

To elucidate the function of GMPPA in more detail we generated a *Gmppa* knockout (KO) mouse model. Importantly, these mice recapitulate many features of human AAMR syndrome patients, e.g. homozygous *Gmppa* KO mice show structural brain alterations. Moreover, *Gmppa* KO mice show a progressive gait disorder with muscle weakness accompanied by centralization of nuclei, alterations of the mean fiber diameter, the distribution of extracellular matrix (ECM) proteins and of the Z-disc related protein α-Actinin. In immunoblot analysis we found hyperglycosylation of proteins, especially hyperglycosylation of alpha-Dystroglycan (α-DG). Hyperglycosylated α-DG shows decreased protein stability and an increased binding to ECM proteins. Suggesting that the observed muscle phenotype is muscle intrinsic, sciatic nerve structure and nerve conduction velocities are normal in *Gmppa* KO mice.

Mechanistically, elevated GDP-mannose levels and a direct interaction of GMPPA with GMPPB support a role of GMPPA as an allosteric feedback inhibitor of GMPPB. *Gmppa* knockdown studies in myoblasts revealed an increased α-DG turnover and activation of ERK signaling.

In mice, a mannose-depleted diet dramatically improved the motor phenotype and almost normalized glycosylation of α-DG and ERK signaling. Thus, we propose that AAMR syndrome caused by *GMPPA* mutations is at least in part a treatable condition.

Zusammenfassung

Beim AAMR-Syndrom leiden Betroffene unter einer geistigen Behinderung, Gangstörungen sowie Achalasie und Alakrimie. Diese autosomal-rezessiv vererbbare Erkrankung wird durch Mutationen im *Guanosin-Diphosphat-(GDP)-Mannose-Pyrophosphorylase A* (*GMPPA*) Gen hervorgerufen, welches das 420 Aminosäuren lange Protein GMPPA kodiert. Das Homolog von GMPPA, die GDP-Mannose-Pyrophosphorylase B (GMPPB), konvertiert Mannose-1-Phosphat und Guanosin-Triphosphat (GTP) zu GDP-Mannose, welches ein essentielles Substrat der Glykosylierungskette darstellt. Bis heute sind nur 18 Patienten mit *GMPPA*-Mutationen beschrieben worden.

Um die Funktion von GMPPA näher zu beleuchten, haben wir ein *Gmppa*-Knockout-(KO)-Mausmodell generiert. Diese Mäuse zeigen ein Krankheitsbild das viele Aspekte der humanen Patienten wiederspiegelt, so zeigen homozygote *Gmppa*-KO-Mäuse kognitive Defekte sowie strukturelle Veränderungen des Gehirns. Des Weiteren zeigen *Gmppa*-KO-Mäuse eine progressive Gangstörung mit zunehmender Muskelschwäche sowie Veränderungen extrazellulärer Matrix-(ECM) und Z-Disk-Proteine. Wir konnten an Gewebe-Lysaten zeigen, dass Proteine von *Gmppa*-KO-Mäusen, insbesondere auch alpha-Dystroglykan (α-DG), hyperglykosyliert sind. Die Hyperglykosylierung von α-DG führt zu einer verminderten Proteinstabilität und einer erhöhten Bindung an ECM-Proteine. Da in *Gmppa*-KO-Mäusen der Ischiasnerv morphologisch unverändert war und die elektrophysiologischen Eigenschaften unauffällig waren, gehen wir von einem muskelintrinsischen Defekt aus.

Da die GDP-Mannose-Spiegel im Gewebe erhöht waren und eine direkte Interaktion von GMPPA mit GMPPB gezeigt werden konnte, vermuten wir, dass GMPPA als allosterischer Inhibitor von GMPPB fungiert.

Gmppa-knockdown-Studien in Myoblasten lassen auf eine Aktivierung des ERK-Signalweges schließen.

Wir konnten durch Gabe einer Mannose-freien Diät eine erhebliche Verbesserung der motorischen Auffälligkeiten sowie eine fast vollständige Normalisierung der Glykosylierung und der ERK-Aktivierung erreichen. Möglicherweise ist eine Mannose-freie Diät auch eine therapeutische Option für Patienten.

This thesis follows the "Guidelines for nomenclature of genes and proteins" from the Mouse Genome Informatics (MGI) and the HUGO Gene nomenclature committee: Human genes are written in uppercase and italics, human proteins are written in uppercase. Mouse genes are written with the first letter in uppercase and the following letter in lowercase, proteins are written in uppercase. Protein names as well as antibodies that are written out completely are written with the first letter in upper case and the following letters in lower case.

Introduction

Glycosylation is the most common post-translational modification of proteins and lipids. It has been reported that more than 50 % of human proteins are conjugated with glycans (Wong 2005). The glycosylation status can affect protein stability and conformation. It plays a prominent role in many biological processes, e.g. cell-to-cell communication, cell-matrix interaction, adhesion, protein targeting and folding, viral or bacterial infection, progression of cancer and aging (Traini et al. 2017, Banerjee et al. 2017, Breloy et al. 2018). Briefly, sugars required for glycosylation are synthesized or isomerized in the cytoplasm, activated and linked to dolichol-phosphate at the endoplasmic reticulum (ER). Linkage of glycans to dolichol enables further use by the glycosylation machinery. Therefore, dolichol-phosphate-sugars are translocated into the ER by flippases and sugars are then added to nascent protein chains. While proceeding from the ER into the Golgi, the glycosylation of proteins becomes eventually highly complex (Fig. 1).

Normally, glycans can be classified into two groups according to their glycan-peptide linkage: Glycans that are linked to asparagine (Asn) residues of polypeptides are termed *N*-glycans, while those that are linked to serine (Ser), threonine (Thr), tyrosine (Tyr), (hydroxyl-) lysine (Lys) and (hydroxyl-) proline (Pro) residues are termed *O*-glycans. In *N*-glycans, the terminal *N*-acetylglucosamine (GlcNAc) is linked to the amide group of Asn. In *O*-glycans, the terminal *N*-acetylgalactosamine (GalNAc) is attached to the hydroxyl group of Ser and Thr residues of polypeptides. However, in addition to the abundant *O*-GalNAc forms, several other subtypes of protein *O*-glycosylation have been reported, such as linkage via *O*-fucose, *O*-glucose, *O*-GlcNAc, *O*-xylose, *O*-galactose on hydroxylysine, and *O*-mannose (Bennett et al. 2012). In mammals, both *N*- and *O*-glycosylation start at the ER site in the cytoplasm with the generation of activated sugar molecules, e.g. GDP-mannose (activated mannose form) by GMPPB.
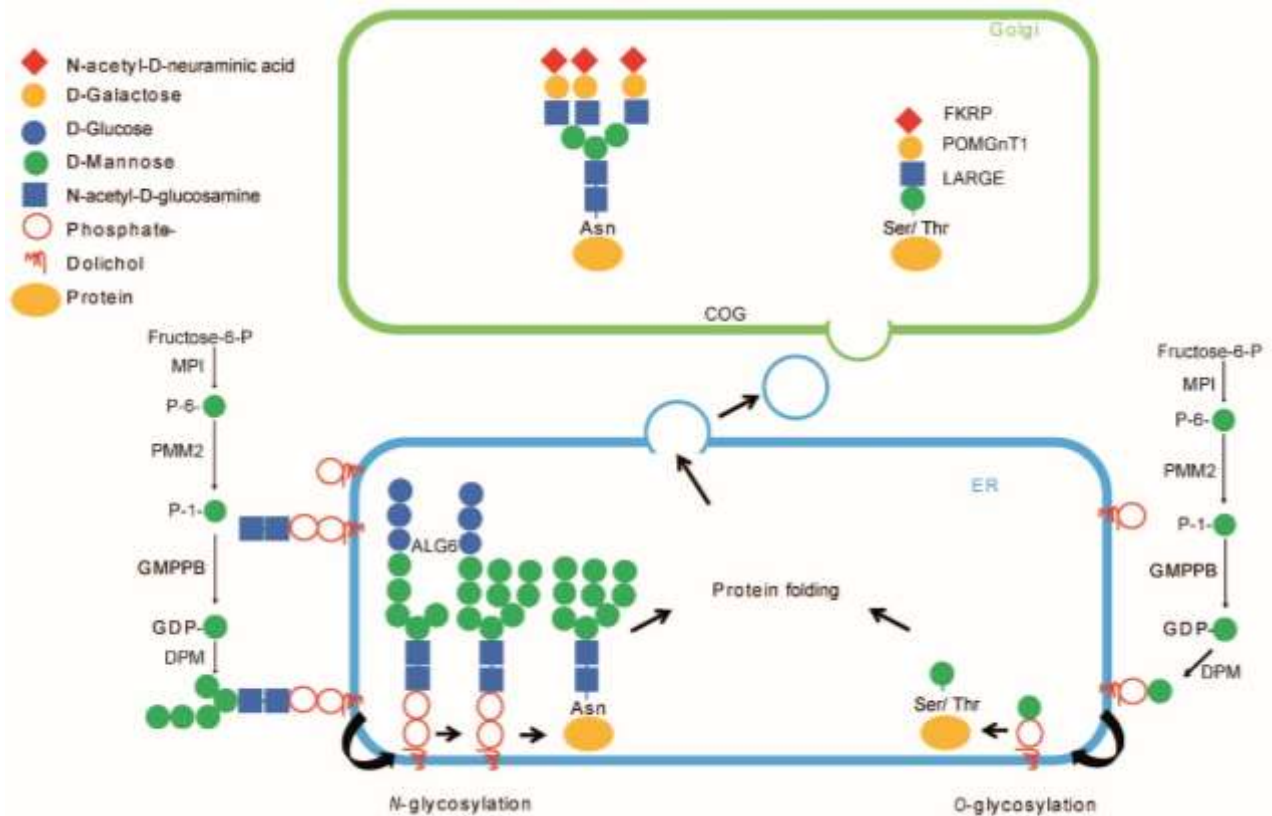
Fig. 1: The glycosylation pathway. *N*-glycosylation and *O*-mannosylation start with the synthesis of mannose-6-phosphate by the Mannose-6-phosphate-isomerase (MPI). Mannose-6-phosphate is converted to mannose-1-phosphate by the Phosphomannomutase 2 (PMM2). Mannose-1-phosphate is converted to GDP-mannose by (Guanosine-diphosphate-mannose-pyrophosphorylase B) GMPPB. GDP-mannose is then transferred to a dolichol-phosphate-molecule by Dolichol-phosphate-mannose synthase (DPM) creating dolichol-phosphate-mannose. The dolichol-phosphate-mannose molecule flips to the lumen of the endoplasmic reticulum (ER) where mannose and glucose molecules are attached. The first glucose residue is attached by the α-1,3-Glucosyltransferase (ALG6). Dol-PP-Glc*N*Ac2Man9Glc3 is transferred onto an asparagine (Asn) residue in case of *N*-glycosylation. In case of *O*-glycosylation, dolichol-phosphate-mannose is transferred normally onto a serine (Ser) or threonine (Thr) residue. Correctly folded proteins exit the ER and move to the Golgi where additional sugar molecules are added and/or modified. COG: Conserved oligomeric golgi, LARGE: Like-acetylglucosaminyltransferase, POMGnT1: Protein-*O*-linked-mannose-β-1,2-*N*-acetylglucosaminyltransferase, FKRP: Fukutin-related protein.

D-Mannose is the 2-epimer of glucose and is transported into mammalian cells via glucose transporters. Hexokinase then phosphorylates mannose to form mannose-6-phosphate. Alternatively, Mannose-6-phosphate is generated by the isomerization of glucose-6-phosphate. Mannose-6-phosphate serves as a substrate for three different enzymes which compete for this substrate. The first enzyme, the Mannose-6-phosphate isomerase catalyzes the conversion of mannose-6-phosphate to fructose-6-phosphate which can be either converted to glucose-6-phosphate or used for glycolysis. The second enzyme, the 2-keto-3-Deoxy-D-glycero-D-galacto-nononic acid-(KDN)-9-phosphate synthase converts mannose-6-

phosphate to KDN-9-phosphate, a sialic acid analog which is used for generation of KDN glycans. The third enzyme, the Phosphomannomutase 2 (PMM2) converts mannose-6-phosphate to mannose-1-phosphate. Mannose-1-phosphate and GTP are converted to GDP-mannose by GMPPB (Sharma et al. 2014).

GDP-mannose is then transferred onto dolichol-phosphate by the enzyme Dolichol-phosphate-mannose synthase (DPM) creating dolichol-phosphate-mannose, which is translocated into the ER lumen, most likely by a flippase. Until today, the exact mechanism of the dolichol-phosphate-mannose translocation into the ER remains unknown. Importantly, GDP-mannose cannot be transported across the ER. Thus, its conversion to dolichol-phosphate-mannose is essential for the glycosylation pathway.

For *N*-glycosylation, the dolichol-linked glycan precursor Dol-PP-GlcNAc2Man5 (dolichol-diphosphate-di-*N*-acetylglucosamine-penta-mannose) is flipped from the cytoplasmic to the luminal side of the ER. In the luminal ER four additional mannose and three glucose residues are attached to the glycan precursor generating Dol-PP-GlcNAc2Man9Glc3 (dolichol-diphosphate-di-*N*-acetylglucosamine-nona-mannose-tri-glucose). Dol-PP-GlcNAc2Man9Glc3 is transferred to the γ-amino-group of a nascent protein by Oligosaccharyltransferase (OST) releasing dolichol-di-phosphate. After the transfer of the precursor Dol-PP-GlcNAc2Man9Glc3 to an Asn residue of a nascent protein chain, further processing of the glycosylation takes place. While α-Glucosidase 1 removes the terminal α1-2 glucose and Glucosidase 2 removes the inner α1-3 glucose residues, Mannosidase 1 removes the terminal α1-2 mannose of some *N*-glycosylated proteins. Correctly folded proteins are transported from ER to Golgi and processing of the glycosylation continues. The enzyme α1-2-Mannosidase removes mannose residues in order to produce GlcNAc2Man5. Some glycoproteins will escape this mannose removal creating oligomannose or so called high-mannose structures. After the *N*-acetylglucosaminyltransferase 1 (GlcNAcT-1) added a *N*-acetylglucosamine residue to the α1-3 mannose, mannose residues are trimmed by α-mannosidase 2 in order to form GlcNAc2Man3 in complex glycoproteins. In hybrid glycans no trimming occurs. A second *N*-acetylglucosamine residue is added to the α1-6 mannose by the *N*-acetylglucosaminyltransferase 2 (GlcNAcT-2). The two *N*-actelyglucosamine residues serve for further branch extension by attachment of fucose, galactose and sialic acid. Complex glycans have more than two branches (Stanley et al. 2009).

For *O*-glycosylation, dolichol-phosphate serves as precursor for activated sugars, e.g. in case of *O*-mannosylation, dolichol-phosphate-mannose flips into the ER lumen and mannose is transferred onto the hydroxyl group of the nascent protein by a heteromeric complex of Protein *O*-mannosyltransferases 1 and 2 (POMT) (Bartels et al. 2016). The first elongation process of *O*-glycans starts in the ER: The Protein-*O*-mannose-β1,4-*N*-

acetylglucosaminyltransferase 2 (POMGnT2) initiates core m3 structures (GlcNAcß1,4Man) which are elongated by β1,3-linked *N*-acetylgalactosamine. The first mannose residue is phosphorylated in the ER and is further modified by disaccharide units (-3-xylose-α1,3-glucuronic acid-β1-) in the Golgi. In the Golgi the Protein *O*-mannose β1,2-*N*-acetylglucosaminyltransferase 1 (POMGnT1) initiates linear core m1 (GlcNAcß1,2Man) and together with β1,6-*N*-acetylglucosaminyltransferase (GnT-Vb/GnT-IX) branched core m2 structures (GlcNAcß1,6GlcNAcß1,2Man). The m1 and m2 core structures are further elongated by ß1,4-linked galactose and neuraminic acid. Similar to *N*-glycosylated proteins only correctly folded proteins are transported from the ER to the Golgi. Misfolded proteins are de-glycosylated in the ER, and degraded by the proteasome and lysosome pathway releasing monosaccharides for re-entering the glycosylation pathway (Martinez-Duncker et al. 2014, Freeze et al. 2012, Cantagrel et al. 2011, Endo 2019, Spiro 2002, Vasconcelos-Dos-Santos et al. 2015).

Similar to *N*- and *O*-glycosylation, the attachment of Glycosyl-phosphatidylinositol (GPI) membrane anchors requires dolichol-phosphate-mannose. Mannose residues that are attached to dolichol-phosphate on the cytoplasmic side of the ER are derived from GDP-mannose. GPI anchor synthesis starts with the transfer of *N*-acetylglucosamine to phosphatidylinositol at the cytoplasmic side of the ER. At the luminal side of the ER the inositol is acylated and mannose and phosphoethanolamine residues are attached. The GPI is then transferred to proteins with a C-terminal GPI signal. GPI anchor synthesis comprises at least 10 reaction steps and more than 20 genes (Kinoshita et al. 2000).

Congenital disorders of glycosylation (CDG)

CDGs appoint mostly to autosomal recessive inherited disorders with mutations in genes encoding proteins essential for the glycosylation pathway and are often associated with brain and eye involvement and muscular dystrophy (Barišić et al. 2011, Engel et al. 2015). In general, CDGs can be divided into two types: CDGs type I are based on defects in the biosynthesis and/or the subsequent transfer of oligosaccharides. CDGs type II are due to defects in oligosaccharide trimming and processing. Among diagnosed CDG patients worldwide, 94 % are represented by CDGs type I and only 6 % by CDGs type II (Péanne et al. 2017).

The most frequent CDG is the PMM2-CDG with over 800 cases out of 1350 CDG cases reported worldwide. The *PMM2* gene encodes for the Phosphomannomutase 2, the enzyme that converts mannose-6-phosphate into mannose-1-phosphate. Mannose-1-phosphate is needed for the formation of GDP-mannose and dolichol-phosphate-mannose (Fig.1). The

reported mutations in the *PMM2* gene lead to a reduced PMM2 activity and less GDP-mannose and dolichol-phosphate-mannose molecules are available, resulting in shortened oligosaccharides and hypoglycosylation. Individuals with the respective mutations show a wide range of affected organs and varying degree of severity depending on the impact of the mutation. Most patients show hypotonia, strabismus, developmental delay, gait ataxia, hypogonadism and abnormal facial gestalt, e.g. high forehead and triangular face. In severe cases, affected children are stillborn or die shortly after birth due to excessive fluid accumulations in the fetal body. Approximately 20 % of affected children die within their first year of life because of organ failure (Péanne et al. 2017, Jaeken 2013).

The second most frequent CDG is reported for mutations in the α-1,3-Glucosyltransferase (ALG6) with over 100 diagnosed cases worldwide. The *ALG6* gene encodes for the α-1,3-Glucosyltransferase which catalyzes the addition of the first glucose residue to the dolichol-phosphate-oligosaccharide in the ER (Fig.1). Mutations in the *ALG6* gene lead to a reduced expression or activity of the glucosyltransferase preventing further processing of the glycosylation. Indeed, patient fibroblasts demonstrated increased Dol-PP-GlcNAc2Man9 levels. Affected individuals show strabismus, hypotonia, ataxia, seizures and mild developmental delay (Jaeken 2013, Péanne et al. 2017).

The Conserved oligomeric golgi (COG) complex is a peripheral Golgi membrane complex composed of 8 subunits. It is crucial for retrograde protein transport from Golgi to ER and for transport processes in the Golgi, thus, allowing proper glycosylation (Fig.1). Thus, mutations in one or more of the COG subunits alters the retrograde and internal Golgi transport as well as ongoing glycosylation processes in the Golgi leading to COG-CDG. It has been shown that mutations in the COG complex lead to a decreased activity of nucleotide-sugar transporters and glycosyltransferases in the Golgi. Patients with COG-CDG suffer from hypotonia, growth retardation, microcephaly, dysmorphism, feeding problems and cerebral atrophy (Jaeken 2013, Wu et al. 2004).

The majority of CDGs is associated with glycosylation defects of α-DG. At least 15 genes are known to cause such α-Dystroglycanopathies. α-DG is an essential linker between the extracellular matrix (ECM) and the muscle fiber sarcolemma. Its proper glycosylation is critical for its ability to bind to ligands in the ECM and for acetylcholine receptor clustering at neuromuscular junctions (NMJ). Its 895 amino acids (aa) precursor protein Dystroglycan (DAG1) is cleaved in the ER into an alpha (α) and a beta (β) subunit (Deyst et al. 1995). The cleavage of Dystroglycan is essential for post-translational modifications, including glycosylation (Esapa et al. 2003). α- and β-DG are both *N*-glycosylated, but α-DG glycosylation is much more complex (Ervasti et al. 1997). α-DG includes two globular domains flanking a central mucin domain which possesses many serine (Ser) and threonine

(Thr) residues which are heavily *O*-glycosylated and, especially, *O*-mannosylated (Stalnaker et al. 2011). This tremendous glycosylation of the mucin domain of α-DG increases its molecular weight significantly. Interestingly, this glycosylation is varying between different tissues and ages. Notably, unglycoslated α-DG has a molecular weight of 74 kDa, while the mature fully glycosylated brain α-DG has a molecular weight of roughly 120 kDa and mature skeletal muscle α-DG shows a molecular weight between 130 and 280 kDa depending on the developmental phase (Gee et al. 1993, Ervasti et al. 1993). Glycosylation of α-DG is necessary for its localization to the cell membrane and its binding to ECM proteins, such as Laminin or Agrin, but it is not essential for β-DG binding (Di Stasio et al. 1999, Michele et al. 2009). As β-DG is non-covalently bound via its N-terminal domain to the C-terminal part of α-DG, β-DG interacts inside the cell with Dystrophin and Growth factor receptor-bound protein 2 (GRB2) and is therefore thought to be involved in cell signaling (Grady et al. 1999, Jung et al. 1995).

Most α-Dystroglycanopathies are classified as CDGs type II and include Muscle-eye-brain disease (MEB), Walker-Warburg-syndrome (WWS), Fukuyama congenital muscular dystrophy (CMD) and limb girdle muscular dystrophy. So far, only α-Dystroglycanopathies due to a reduced glycosylation of α-DG, and not a hyperglycosylation, have been reported.

The *LARGE* gene encodes for the Golgi resident bifunctional glycosyltransferase Like-acetylglucosaminyltransferase (LARGE) which attaches the final xylose and glucuronic acid to α-DG enabling its binding to ECM ligands (Fig.1). Moreover, binding of LARGE to the N-terminal domain of α-DG is crucial for proper α-DG glycosylation (Kanagawa et al. 2004) and mutations in LARGE cause CMD (Brockington et al. 2005). LARGE-deficient mice show similar symptoms compared to human patients, but mice are more severely affected. Strikingly, these mice exhibit a shorted life span due to a severe and progressive CMD with defects in skeletal and cardiac muscles and impaired neuronal migration (Holzfeind et al. 2002). Moreover, LARGE-deficient mice show hypoglycosylated α-DG with decreased molecular weight and reduced ECM ligand binding compared to wild-type (WT) mice. It has been shown that overexpression of LARGE in mouse models with defective glycosyltransferases rescues proper ECM ligand binding (Aguilan et al. 2009, Patnaik et al. 2009, Brockington et al. 2005). Interestingly, LARGE overexpression in mice resulted in hyperglycosylation of α-DG and reduced muscle force (Brockington et al. 2010).

The *POMGNT1* gene encodes for the Golgi resident Protein-*O*-linked-mannose-β-1,2-*N*-acetylglucosaminyltransferase which initiates linear m1 and branched m2 core structures in *O*-glycans (Fig.1). Individuals with mutations in *POMGNT1* suffer from MEB-disease with CMD, eye involvement, mental retardation and type II lissencephaly. Life expectancy of the patients is about 12 years (Dobson et al. 2013). POMGNT1-deficient mice develop MEB

disease with hypoglycosylation of α-DG. Homozygous knockout (KO) mice showed reduced fertility, abnormal eye development, dystrophic muscles with reduced fiber size and centrally located nuclei. Moreover, these mice showed developmental defects in the brain including a smaller cerebellum, thinner cortical layers, cell clumps in the cerebellum due to abnormal cell migration and hippocampal alterations (Liu et al. 2006).

Similar findings have been reported for mutations in the Fukutin-related protein (FKRP) in mice, a putative glycosyltransferase (Fig.1). Affected individuals with a reduced FKRP activity suffer from CMD, limb girdle muscular dystrophy, WWS and MEB. FKRP-deficient mice die during embryonic development. Mice with a *Fkrp*-point mutation display hypoglycosylated α-DG, muscle weakness, ocular and brain abnormalities due to a reduced FKRP activity. Muscular dystrophy of skeletal and heart muscle was indicated by a higher variation in fiber size, more necrotic fibers, more centrally located nuclei and increased fibrosis. Brain abnormalities included a smaller brain size, expanded lateral ventricles, disorganized cortex and cerebellum and hippocampal alterations (Chan et al. 2010).

As described above, α-Dystroglycanophathies show many features overlapping with brain and muscle disorders. In mouse models it has been shown that brain abnormalities include abnormal layering of the cortex, an altered hippocampus and a smaller cerebellum with abnormal cell clusters.

The cortex is the outer layer of the cerebrum of the brain and is connected to several subcortical structures. It consists of motoric, sensory and association areas. Sensory areas, such as primary visual, primary auditory or primary somatosensory cortex, receive and process information. Motoric areas, such as the primary motor cortex, are necessary for voluntary movement. Association areas include areas that do not belong to the primary cortex and are necessary for a perceptual experience (Shipp 2007).

Thalamus, hypothalamus, amygdala and hippocampus form the limbic system which is related to emotions and memory and learning.

The hippocampus is important for declarative memory function. It comprises the dentate gyrus, cornu ammonis (CA) fields and the subiculum. The dentate gyrus receives input from the entorhinal cortex. The CA fields contain pyramidal cells and are divided into three regions (CA1–CA3) (Cohen et al. 1999, Wible 2013).

The cerebellum plays an important role in the control and coordination of movements (Paullin et al. 1993). It consists of the cerebellar cortex, white matter and a fluid-filled ventricle at the base (Braitenberg et al. 1958). The cerebellar cortex is divided into a granule cell layer, a Purkinje cell layer and the molecular layer. Purkinje cells belong to the second largest

neurons in the human brain. It has been reported that Purkinje cell alterations impair voluntary movements (Schmitz-Hübsch et al. 2006).
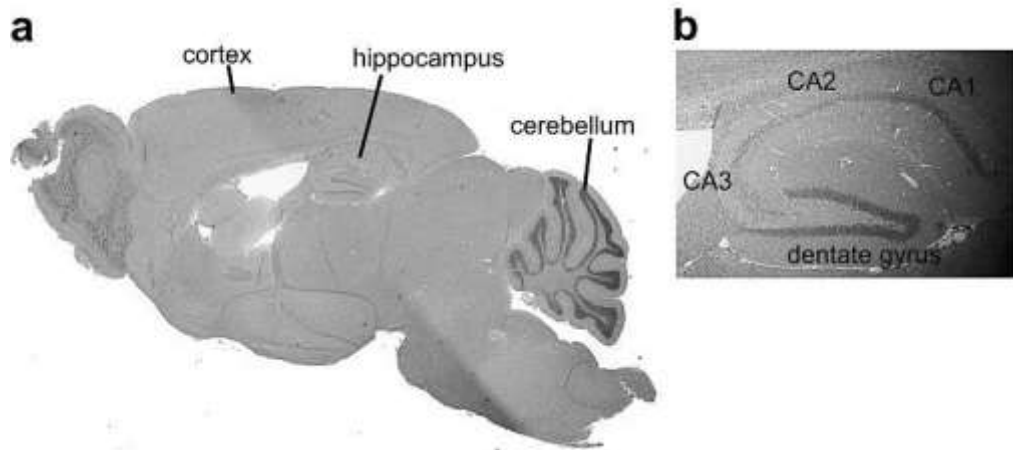

Fig. 2: The murine brain. a) Hematoxylin/esosin (HE) staining showing a sagittal section of a murine brain with cortex, hippocampus and cerebellum. **b)** HE staining of a murine hippocampus showing the different CA fields and the dentate gyrus.

All α-Dystroglycanopathies are connected with CMD. In mouse models muscular dystrophy is reflected by reduced muscle strength, variation in fiber size, necrotic fibers, centralized nuclei and fibrosis.

The muscular system comprises smooth and skeletal muscles as well as the heart. Muscles are involved in manifold functions such as movement, blood circulation, heartbeat, breathing, digestion, temperature regulation and vision. The unique feature of skeletal muscles is their conscious control. In humans, skeletal muscle tissue comprises 40 % of total body weight and approximately 50-75 % of all proteins found in the human body. Skeletal muscle tissue comprises skeletal muscle fibers, blood vessels, nerve fibers, and the ECM. The ECM is divided into different levels: The epimysium surrounds skeletal muscle, the perimysium surrounds fascicles and the endomysium surrounds muscle fibers.

Skeletal muscle cells, also known as myofibers or fibers, are multinucleated and post-mitotic (Hikida 2011) cells. Skeletal muscle cells appear striated under the microscope due to their highly organized structure: Actin (thin filaments) and Myosin filaments (thick filaments) are regularly repeated together with their regulatory proteins Troponin and Tropomyosin forming the functional unit of a fiber, the sarcomere, which is important for contraction. The sarcomere is bordered by Z-discs to which the Actin filaments are anchored. Z-discs contain several proteins, such as α-Actinin or the Capping actin protein of muscle Z-disc β subunit (CAPZB).

Skeletal muscle stem cells, the satellite cells, are located between the sarcolemma, the skeletal muscle cell membrane, and the basal lamina. Satellite cells are important for muscle

growth, repair and regeneration. Upon myogenic signals, satellite cells start to proliferate and differentiate into new fibers (Hikida 2011, Wilkins et al. 2001, Macaluso et al. 2012, Bareja et al. 2014, Frontera et al. 2014).
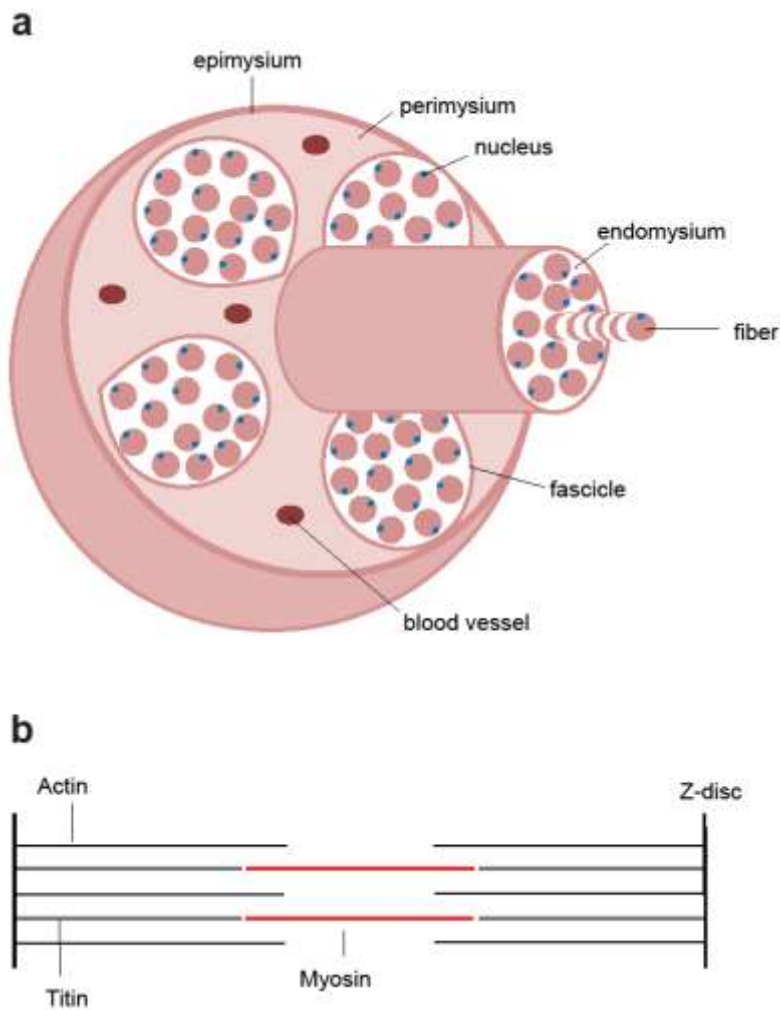

Fig. 3: Schematic structural organization of a skeletal muscle. a) Each skeletal muscle is embedded into the epimysium. Bundles of muscle fibers, named fascicles, are surrounded by the perimysium. Each muscle cell, called fiber, is surrounded by the endomysium. **b)** Schematic overview of the basic muscle contractile unit, the sarcomere: thick Myosin filaments are shown in red, thin contractile Actin filaments are shown in black. The elastic protein Titin is shown in green. Actin and Titin are connected via α-Actinin to the Z-discs, shown as vertical black lines.

Recent studies revealed that mutations in the *Guanosine-diphosphate-(GDP)-mannose-pyrophosphorylase B* (*GMPPB*) causes CMD and MEB with hypoglycosylation of α-DG. GMPPB catalyzes the formation of GDP-mannose (Fig.1), which is required for the glycosylation of proteins and lipids. The GDP-mannose molecule is an essential cellular requirement for a number of glycosylation pathways, including *O*-mannosylation of membrane and secretory glycoproteins, such as α-DG (Stalnaker et al. 2011, Endo 2019).

Our group identified mutations in the homolog of the *GMPPB* gene, the *Guanosine-diphosphate-(GDP)-mannose-pyrophosphorylase A* (*GMPPA*) as the causative genetic

defect for achalasia, alacrima and mental retardation (AAMR) syndrome (Koehler et al. 2013). AAMR syndrome is a rare disease that is inherited as an autosomal recessive trait. Achalasia is the inability to swallow and alacrima is the absence of tear flow. Individuals with mental retardation show deficits in memory and learning, reasoning and adaptive behaviors due to brain alterations (Koehler et al. 2013). Up to now, 18 patients are reported worldwide and only two of them are older adults. Symptoms arise at birth or within the first months of life. Apart from the mentioned symptoms, some AAMR patients show gait abnormalities, muscle hypotonia as well as visual and hearing impairment (Koehler et al. 2013, Gold et al. 2017, Benítez et al. 2018).

The *GMPPA* gene encodes a protein of 420 amino acids (aa). The Guanosine-diphosphate-mannose-pyrophosphorylase A (GMPPA) does not show catalytic activity, but is able to bind GDP-mannose (Ning et al. 2000). These findings suggest that GMPPA might serve as an allosteric feedback inhibitor of GMPPB (Koehler et al. 2013).

Aim of this thesis

Glycosylation is of vital importance as it is the most common post-translational modification of proteins and lipids. While *N*-linked glycans are linked to the nitrogen atom of an asparagine, *O*-linked oligosaccharides are attached to the hydroxyl oxygen group of a serine, threonine, tyrosine, (hydroxl-) lysine or (hydroxl-) proline. Both *N-* and *O*-glycosylation start in the cytoplasm with the generation of activated sugar molecules that are linked to dolichol-phosphate at the ER. Dolichol-phosphate-sugars are then flipped into the ER, more sugar residues are added and subsequently linked to nascent protein chains. The glycosylation process continues while the protein is proceeding into the Golgi apparatus. Perturbations of the glycosylation pathway lead to severe diseases, which are categorized as CDGs.

Our group recently identified that mutations in the *GMPPA* gene cause AAMR syndrome in combination with muscle weakness and hypotonia and gait abnormalities. While the function of GMPPA is unknown, it is known that its homolog GMPPB catalyzes the formation of GDP-mannose, a key substrate for both *N-* and *O*-glycosylation. Because GMPPA does not show catalytic activity itself, but does bind the product of GMPPB, GDP-mannose, we hypothesize that GMPPA serves as an allosteric feedback inhibitor of GMPPB.

To get more insights into the molecular function of GMPPA and to elucidate the pathophysiology of the AAMR syndrome we disrupted the *Gmppa* gene in mice. This thesis addresses the following main questions:

- Does GMPPA interact with GMPPB?
- What are the cellular and subcellular consequences of the disruption of *Gmppa*?
- Are there treatment options?

Material and methods

Material

Chemicals, enzymes and nucleotides

All chemicals were at least of analytical grade and purchased from Sigma, Merck or Roth unless otherwise stated. Solutions were prepared with deionized water. Enzymes were obtained from Roche, Invitrogen, New England Biolabs and Thermo. Oligonucleotides were purchased from MWG-Biotech. Radioactive nucleotides were obtained from Hartmann Analytic.

Bacterial Vectors

The following vectors were used in order to generate plasmids for overexpression:

Vector	Source
pCMV10 3xFLAG	Sigma
pCS2+-myc$_6$	gift from Prof. Dr. Ralph Rupp
pGex4T1	Amersham
pMalC2X	NEB
pEGFP-N3	Clontech
pKO Scrambler 901	Lexicon Genetics

Table 1: List of cloning vectors.

Primer pairs for cloning

The following primer pairs were used to clone GMPPA/GMPPB variants with the respective cDNA expression vector as a template:

Primer sequence	For plasmid
tataGGATCCATGTTGGAGGACTCACCAGGCTT	Myc-GMPPA ΔN
tataGGATCCGAGGATGATCTGGTTGGTGAAG	(aa206-420)
tataGGATCCATGCTGGTGACCAAGGTGGAGG	Myc-GMPPB ΔN
tataGGATCCTCACATGATGATACGAGGCTCTG	(aa133-360)
tataGGATCCATGCTCAAAGCGGTGATCCTG	Myc-GMPPA ΔC
tataGGATCCTTGCCCATCCTGCTGATTACG	(aa1-205)

tataGGATCCATGAAGGCACTGATCTTAGTGGG	Myc-GMPPB ΔC
tataGGATCCGATGGAGCCCTCCTGGC	(aa1-132)
tataAGATCTATGAAGGCACTGATCTTAGTGG	GMPPB-Flag
tataGCGGCCGCCATGATGATACGAGGCTCTG GC	
ggg ACCGGTTCGTGGAGAAGCCA	GMPPB-D334N
gggGAGCTCATTATTAACTATGACGTCCTC	GMPPB-D334N

Table 2: List of primer sequences.

Plasmids containing GMPPA-Myc, GMPPA-D182N-Myc and GMPPA-T334P-Myc were cloned by Sebastian Gießelmann. GST- and MBP-constructs were cloned by Sonnhild Mittag. To generate FLAG-GMPPA, GMPPA was excised from GST-GMPPA with restriction enzymes and inserted into the pCMV103XFlag vector.

Antibodies and lectins

The following primary polyclonal/monoclonal antibodies/lectins were purchased. The respective working concentrations for Western Blot and/or immunohistochemistry are listed in the following table:

Antibodies/lectins (raised in)	Working concentration		Source
	Western Blot	Immunocytochemistry	
rabbit anti-GMPPA	1:500	1:25	Proteintech
rabbit anti-GMPPB	1:500	not used	Abcam
mouse anti-GMPPB	Not tested	1:25	Novus Biologicals
mouse anti-GFAP	1:1000	1:1000	Milipore
rabbit anti-GAPDH	1:1000	not used	Santa Cruz
rabbit anti-Myc Tag	1:1000	1:500	Millipore
mouse anti-Myc Tag	1:1000	1:1000	Sigma

rabbit anti-Flag Tag	1:1000	1:500	Sigma
anti-MBP	1: 4000	not used	Sigma
anti-GST	1: 10000	not used	gift from Prof. Dr. Jürgen Wienand
rabbit anti-Laminin	1:500	1:200	Abcam
rabbit anti-Nidogen	1:500	1:200	Abcam
rabbit anti-Collagen IV	1:500	1:100	Abcam
mouse IgM anti-Oligomannose	1:50	1:50	gift from Prof. Dr. Rüdiger Horstkorte
mouse IgM anti-Paucimannose	1:50	1:50	gift from Prof. Dr. Rüdiger Horstkorte
biotinylated PNA	1:300	1:50	gift from PD Dr. Christian Thiel
biotinylated Concanavalin A	1:300	1:50	gift from PD Dr. Christian Thiel
mouse anti-α-DGIIH6C4	1:250	1:100	Millipore
mouse anti-α-DGVIA4	1:250	1:100	Millipore
sheep anti-core-Dystroglycan	1:1000	1:100	R&D Systems

goat anti-α-DG	1:500	1:100	Abcam
rabbit anti-β-DG	1:500	1:100	Gene Tex
biotinylated anti-Ubiquitin	1:1000	not used	gift from Dr. Sebastian Drube
rabbit anti-TGN38	1:500	1:250	Santa Cruz
rabbit anti-GLG1	1:500	1:250	Abcam
rabbit anti-P-ERK1/2	1:4000	not used	Cell signaling
rabbit anti-ERK 1/2	1:4000	not used	Cell signaling
mouse anti-BIP	1:250	not used	BD Biosciences
mouse anti-GM130	1:500	1:250	BD Biosciences
mouse anti-Histidin Tag	1:1000	not used	R&D Systems
mouse anti-NF200 (2H3 and SV2)	not used	1:2	DSHB
BTX-Alexa 555	not used	1:500	Invitrogen

mouse anti-α-Actinin	not used	1:200	Abcam
ECL Mouse IgG, HRP-Linked	1:4000	not used	Amersham (GE healthcare)
ECL Rabbit IgG, HRP-Linked	1:4000	not used	Amersham (GE healthcare)
ECL Goat IgG, HRP-Linked	1:1000	not used	Sigma
ECL Mouse IgM, HRP-Linked	1:4000	not used	Invitrogen
ECL Sheep IgG, HRP-Linked	1:4000	not used	Sigma
ECL Streptavidin, HRP-Linked	1:10000	not used	Sigma
Hoechst-33258 (DAPI)	not used	1:10 000	Molecular Probes Invitrogen
anti-mouse IgG Alexa Fluor 488, 555	not used	1:1000	Molecular probes Invitrogen
anti-rabbit IgG Alexa Fluor 488, 555	not used	1:1000	Molecular probes Invitrogen
anti-mouse IgM Alexa Fluor 555	not used	1:1000	Molecular probes Invitrogen
anti-goat IgG Alexa Fluor 488	not used	1:1000	Molecular probes Invitrogen
anti-biotin (Streptavidin) IgG Alexa Fluor 488	not used	1:1000	Molecular probes Invitrogen

Table 3. Antibodies used for Western Blotting and Immunocytochemistry.

Methods

All animal experiments were approved by the Thüringer Landesamt für Lebensmittelsicherheit und Verbraucherschutz (TLLV) in Germany (license number 02-013/14). Experiments were performed on a C57BL/6 background. Mice were housed in a 12 h light/dark cycle and fed on a regular diet *ad libitum*. Littermates of the same sex were randomly assigned into experimental cohorts. Experiments were performed at different ages as indicated. Treatment cohorts were fed with nominally mannose-free food (22 % fat, 28 % protein, 50 % carbohydrates; Ssniff) as compared to the normal chow (9 % fat, 24 % protein, 67 % carbohydrates; Altromin).

Targeted inactivation of the murine *Gmppa* gene

To disrupt *Gmppa* in mice, we used the EUCOMM EPD0621_7_G03 embryonic stem cell clone (Source Bioscience). This clone harbours a genetrap cassette following exon 4 and has conditional potential with exon 5 flanked by loxP sites within the *Gmppa* gene. The ES-cell clone was injected into C57BL/6 donor blastocysts and transferred into foster mice by Katrin Schorr. The resulting chimeric mice were mated with C57BL/6 mice to obtain heterozygous gene-trapped mice, which were subsequently mated to obtain homozygously gene-trapped mice. To obtain knockout mice without the LacZ reporter cassette and the removal of exon 5, gene-trapped mice were mated with Flpe deleter mice and then with Cre deleter mice.

Phenoyping

Fear conditioning

In fear conditioning tests, a neutral stimulus, in this case a tone, is paired with an aversive event. The aversive event, an electric footshock, induces fearful behaviour categorized by robust autonomic responses and a cessation of movement or freezing (Fanselow et al. 2005, Smith et al. 2007).

The fear conditioning apparatus (Ugo Basile) consists of 4 identical sound-attenuating chambers (d 55 x w 60 x h 57 cm) with door switch, electrified grid floor, fan, video camera, speaker, infrared and LED light. Animals were video recorded the whole time for automatic detection of freezing by ANY-maze software (Stoelting):

Young (3 months) and aged (12 months) mice were placed in a chamber (d 17 x w 17 x h 25 cm, plexiglas wall, 4 lux light, 70 % ethanol, fan speed 100 %) and allowed to explore the surrounding area for 180 s. A tone was played for the following 20 s (9 kHz, volume 20 %, 80

dB) paired with a foot shock (US, 0.7 mA for 2 s) in the last 2 s applied via the metal grid. After additional 60 s mice were returned to their home cages.

After 24 h, the cued test was performed to determine tone-shock association: Mice were placed in the fear conditioning apparatus in a differently shaped box with altered colour pattern (caro patterned wall, white floor), lightening (2 lux), odour (3 % acetic acid) and fan speed (50 %) compared to the day before. Mice were allowed to explore the new area for 180 s before the tone was applied for 180 s. After additional 60 s mice were transferred back into their home cages and allowed to relax for 2 h. After 2 h they were placed in the same context as the day before, during acquisition (plexiglas walls, metal grid floor, lightening 4 lux, odour 70 % ethanol, fan speed 100 %), and observed for 180 s.

For freezing detection, videos were manually analyzed. Freezing time was presented as percentage of the investigated 60 s intervals:

$$\text{freezing time (\%)} = \left(\frac{\text{freezing time (s)}}{60 \text{ (s)}} \right) *100$$

Fear conditioning experiments were conducted together with Tanja Herrmann. All recorded datasets were manually analysed by Tanja Herrmann.

Beam Walk balance test

Mice were trained to walk on a horizontal 20 cm elevated plastic beam (1000 mm long, 80 mm broad) leading to their home cage (Irintchev et al. 2005). After the initial learning phase mice were video-recorded with a NV-DS12 camera (Panasonic). For quantitative analysis video sequences were digitized using the software *Virtual Dub 1.5.10* (free software available at www. virtualdub.org). In order to quantify the foot base angle (FBA) two video sequences per animal were selected with the mouse walking at least ten consecutive steps (5 left toe, 5 right toe). The FBA at toe-off position of the hind-paws was measured using single video frames from recordings of beam walking mice. The angle was determined with *ImageJ* (free software available at www. fiji.sc). For statistical analysis the mean of two independent trials was taken.

Kondziela´s inverted screen test

The inverted screen is a square of wire mesh consisting of 8 mm squares of 1 mm diameter wire. It is surrounded by a beading to avoid climbing to the other side. The mouse is placed in the center of screen, a stop clock is started and the screen is rotated within 2 s to an inverted

position above a padded surface. The time the mouse is falling off the screen is recorded or it is removed after a criterion time of 70 s (Deacon 2013).

Weights test

The Weights test consists of eleven different weights. Each weight consists of steel wire that is connected to steel chains. The steel chains differ in length between the different weights. The following weights were tested: 2.8, 9.2, 15.4, 19, 34.2, 42.5, 50, 60.4, 73, 86.5 and 103 g, respectively. For the weight test, a mouse is held on its tail base and allowed to grasp the weight. Then a stop clock is started and the mouse is lifted up on its tail until the weight is clear of the bench. After a criterion time of 3 s the mouse is allowed to relax for 10 s. If the mouse was able to hold the weight for 3 s, the same procedure is applied for the next heavier weight. If the mouse failed to hold the weight for 3 s, the procedure for this weight is repeated. If the mouse failed to hold the weight 3 times, the last weight the mouse was able to hold for 3 s is considered the heaviest weight the mouse is able to hold (Deacon 2013).

Electrophysiological measurements

Long-term-potentiation experiments

After decapitation of mice (12-14 weeks of age) the brain was quickly removed, immediately placed in ice-cold artificial cerebrospinal fluid (aCSF: 120 mM NaCl, 3.5 mM KCl, 5 mM $MgSO_4$ x 7 H_2O, 1.25 mM NaH_2PO_4 x H_2O, 0.2 mM $CaCl_2$ x 2 H2O, 10 mM glucose, 25 mM $NaHCO_3$, bubbled with 5 % CO_2, 95 % O_2) and cut into horizontal slices with a vibratome (VT 1200S, Leica Instruments) as described previously (Liebmann et al. 2009). Slices (400 µm) were stored at RT in recording-aCSF (aCSF: 124 mM NaCl, 3 mM KCl, 1.8 mM $MgSO_4$ x 7 H_2O, 1.25 mM NaH_2PO_4 x H_2O, 1.6 mM $CaCl_2$ x 2 H_2O, 10 mM glucose, 26 mM $NaHCO_3$, bubbled with 5 % CO_2, 95 % O_2) for at least 1 h until use. Slices were transferred to an interface-recording chamber allowed to adapt to recording conditions for at least 1 h (oxygenated aCSF, 32 °C, flow 2-3 ml/min). Bipolar stimulating electrodes with a tip diameter of 100 µm (SNE-200X, Science-Products) were placed onto the glutamatergic Schaffer collaterals of the hippocampus CA3 region to stimulate CA1 pyramidal neurons. Upon stimulation (pulse duration 50 µs), field excitatory postsynaptic potentials (fEPSPs) were recorded using glass microelectrodes (2-5 MΩ, filled with recording-aCSF, Model P-97 Micropipette Puller, Sutter Instruments) impaled into the stratum pyramidale or the stratum radiatum of hippocampal CA1 region. Slopes of fEPSPs and amplitudes of population spikes (PS) were analyzed. Data of field potential recordings were collected with an extracellular

amplifier (EXT-02, NPI), low pass filtered at 4 kHz and digitally stored with a sample frequency of 10 kHz. Data acquisition and analysis of population spike amplitudes were performed using the software Signal (Cambridge Electronic Design).

To determine the maximal population spike amplitude or the maximal slope of fEPSP the stimulus intensity was increased in gradual steps of 5 V (range 0-60 V) for each experiment (interstimulus interval 30 s). The relationship between stimulus intensity and the evoked response was fitted by a sigmoid function: $R(i)=R_{max}/1+exp(i-i_h)$, where R(i) is the response at intensity (i), Rmax is the maximal response and ih is the intensity at which half-maximal response was observed.

For investigation of changes in LTP the following protocol was applied: Stimuli with half-maximal intensity were applied (interstimulus interval 20 s) for 30 min to record the baseline. The high frequency stimulus (HFS, 5 x 100 pulses a 100 Hz) induced increasing PS amplitudes and slopes of fEPSPs, which were recorded over 1 h (interstimulus interval 20 s). The amount of potentiation was analysed by comparing baseline values (normalized and averaged 20 min before induction) with those values collected within 60 min after HFS application. LTP measurements were performed by Tanja Herrmann.
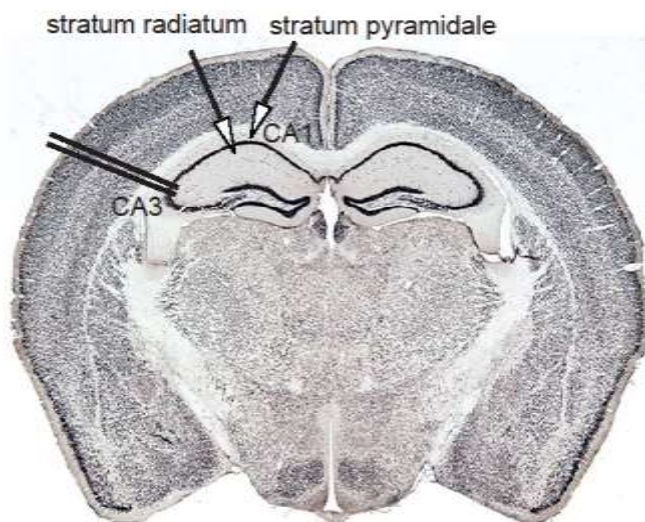

Fig. 4: Recordings of field potentials on coronal murine sections. The stimulation electrode was placed in the stratum radiatum in the CA3 area, while recording electrodes were located in the CA1 region of the hippocampus. The figure was adapted from http://melbournebraincentre.edu.au/content/coronal-section-mouse-brain.

Recording of SSAPs and CMAPs

While under anesthesia, the body temperature of the mice was maintained with a heating pad. Sensory sum action potentials (SSAPs) were recorded near the base of the tail 30 mm proximal of the stimulation site close to the tip of the tail. Compound muscle action potentials (CMAPs) were evoked near the base of the tail and recorded 30 mm distal to the stimulation

site close to the tip of the tail. Electrodes with a tip diameter of 1 μm and an impedance of 0.1 MΩ were used (WE30030.1H10, Science Products). Both SSAPs and CMAPs were evoked with increasing intensities (0-15 V, increment 1 V, 50 μs duration) at a sample frequency of 20 kHz. Signals were processed with an extracellular amplifier (EXT 02F, NPI, high-pass filter: 3 Hz, low-pass filter: 2 kHz). For analysis we used the Signal 3 software (CED). Amplitudes were determined from peak to peak. Recordings were performed by Lutz Liebmann.

Molecular methods

Phenol-chloroform extraction of mouse genomic DNA from tail biopsy

To obtain mouse genomic DNA in high purity from tail biopsies, a phenol-chloroform extraction was performed. Each tail biopsy was incubated in 500 μl lysis buffer (50 mM Tris, 100 mM EDTA, 100 mM NaCl, 1 % SDS, pH 8.0) supplemented with 10 μl of proteinase K (14 mg/ml) at 55 °C overnight. Then, one volume of a phenol-chloroform-isoamylalcohol mixture (25:24:1, Roth) was added and the sample rotated for 5 min at RT. After centrifugation at 14000 rpm for 10 min at 4 °C, the upper aqueous phase was transferred into a new tube and extracted with chloroform-isoamylalcohol mixture (24:1). DNA was precipitated by adding 1 volume isopropanol and 1/10 vol. 3 M sodium acetate pH 5.2. After centrifugation at 14000 rpm for 30 min at 4 °C, the resulting DNA pellet was washed with 70 % ethanol, air dried and dissolved in 150 μl TE buffer overnight at 4 °C. This high-grade DNA was further used for Southern blot analysis.

Southern blot

For Southern blot analysis, phenol-chloroform-purified DNA from tail biopsies was digested overnight with 20-30 units of a suitable restriction enzyme (Thermo) at the appropriate incubation temperature. Resulting fragments were separated by 0.8 % agarose gel electrophoresis. For facilitating the transfer of DNA fragments onto a nylon membrane (Hybond XL, GE Healthcare) the gel was washed several times with distilled water and the DNA fragmented in 0.25 M HCl for 15 min, and washed again with distilled water. After equilibration in 0.4 M NaOH for 20 min, a capillary blot was assembled with 0.4 M NaOH. DNA transfer from the gel to the membrane by capillary forces was performed overnight at RT. After blotting, the membranes were baked for 2 h at 80 °C to crosslink the DNA to the membrane. Before hybridization the membrane was rinsed in 2 x SSC and equilibrated in prehybridization buffer prior to hybridization with the radioactive probe. A probe template of 453 bp mirroring chr1:75546871-75558943 of the mouse genome (mm10) was used for

labelling of the radioactive probe. After gel purification, 25-50 ng of the template were diluted in 45 µl of TE buffer and denatured at 95 °C for 5 min and cooled on ice. The denatured probe was briefly centrifuged down and transferred into a Rediprime II (GE Healthcare) tube containing lyophilized dATP, dTTP, dGTP, and Klenow fragment of DNA polymerase I. Following the addition of radioactive ^{32}P-dCTP the reaction mixture was incubated for 30 min at 37 °C. For the removal of non-incorporated radiolabelled nucleotides the probe mix was purified over a G50 column (GE Healthcare, USA). Using a Beckman scintillation counter, radiolabelling of the probe was tested and a hybridization mix (7 % SDS, 10 % PEG, 1.5 x SSPE, 0.1 mg/ml hering sperm DNA (Roche) with 500,000 cpm/ml was prepared. To block unspecific DNA binding to the membrane, the membrane was prehybridized for 2 h at 68 °C with blocking buffer (7 % SDS, 10 % PEG, 1.5 x SSPE, 0.1 mg/ml hering sperm DNA (Roche) in a rolling bottle. Hybridization with the radio-labelled probe was performed overnight at 68 °C in rolling bottles. The membrane was washed with preheated wash buffer (2 x SSC, 0.1 % SDS) at 68 °C for 20 min several times until radioactivity of the membrane was below 200 cpm. The membrane was covered with saran wrap and exposed to a Phosphor-imager plate (Fuji Films). Southern Blot was performed with the help of Christopher Hennings.

RNA isolation

Mice were sacrificed. Organs were removed and flash frozen in liquid nitrogen. Tissue homogenization was performed with mortar and pestle in liquid nitrogen. After evaporation of liquid nitrogen, 1 ml Trizol (Invitrogen) per 100 mg tissue weight was added. The Trizol-tissue mixture was vortexed and incubated at RT for 5 min. After centrifugation at RT and 4000 g for 5 min, the supernatant was transferred into a new tube. Per 1 ml Trizol 200 µl Chloroform were added and samples were vigorously shaken by hand. After incubation for 2 min at RT, samples were centrifuged at 4 °C and 14000 rpm for 15 min. The aqueous phase was transferred into a new tube. 1 volume isopropanol was added and samples were incubated at RT for 10 min followed by a centrifugation at 4 °C and 14000 rpm for 10 min in order to precipitate the RNA. The RNA pellet was washed with 75 % (v/v) ethanol. After air-drying the RNA pellet was dissolved in RNase free water and stored at -80 °C.

Reverse transcription

Reverse transcription was conducted with 0.5 µg total RNA using the SuperScriptIII reverse transcription kit (Invitrogen):

material	Volume in µl
50 µM Random Primer	1
10 mM dNTPs	1
RNA	1 (0.5 µg)
RNase-free H$_2$O	10

Table 4: Materials and volumes needed for reverse transcription step 1

After incubation at 65 °C for 5 min, the mixture was incubated for 1 min on ice and following components were added:

material	Volume in µl
5 x FS buffer	4
0.1 M DTT	1
RNase Out	1
SuperScript III reverse transcriptase	1

Table 5: Materials and volumes needed for reverse transcription step 2

After incubation at 25 °C for 5 min, the mixture was incubated for 1 h at 50 °C and afterwards for 15 min at 70 °C.

Real time Quantitative PCR

Quantitative PCR (qPCR) was performed with 100 ng final amount of cDNA (assuming reverse transcription 1:1), the innuMix qPCR MasterMix (Analytik Jena) and Taqman Gene Expression Assays (Thermo Fischer) for *Gapdh* (4331182, Assay-identifier: Mm99999915_g) and *Gmppa* (4331182, Assay-identifier: Mm00505084_m1):

material	Volume in µl
2 x innuMix	5
Taqman Gene Expression Assay	0.5
cDNA (22.2 ng/µl)	4.5

Table 6: Materials and volumes needed for quantitative PCR

The qPCR was performed in a thermocycler (BioRad):

step	temperature	time	go back to step	repeat cycles
1	95 °C	3 min		
2	95 °C	5 s		
3	60 °C	30 s	2	40

Table 7: Quantitative PCR cycling temperatures and duration

Extraction of DNA from tail biopsies

Genomic DNA was extracted from tail biopsies using the Hot-Shot protocol: To each tail biopsy (1-3 mm in size) 50 µl of alkaline lysis buffer (25 mM NaOH, 0.2 mM EDTA) were added and incubated for one hour at 95 °C. Afterwards, the samples were cooled down on ice for 5 min and 50 µl of neutralization buffer (40 mM Tris-HCl, pH 5.0) were added. The samples were vortexed, spun down and stored at 4 °C until further use.

Genotyping PCR

Genotyping was performed on genomic DNA obtained from tail biopsies treated with the Hot-Shot protocol. Each reaction was performed in a total volume of 20 µl:

material	Volume in µl
10 pmol primer for (MWG-Biotech): gaccctgtcatcttaggctg	1
10 pmol primer WT rev (MWG-Biotech): gcatatgtgggggtacacaa	0.5
10 pmol primer KO rev (MWG-Biotech): cttgtcagcagtacttctgc	1
10 x PCR buffer	2.0
50 mM MgCl$_2$	0.75
10 mM dNTPs (Invitrogen)	0.5
H$_2$O	12.65
Taq polymerase (Invitrogen)	0.1
DNA	2

Table 8: Material and volumes needed for genotyping PCR

The PCR was performed in a thermocycler (Biometra):

step	temperature	time	go back to step	repeat cycles
1	94 °C	5 min		
2	94 °C	30 s		
3	72 °C	40 s	2	39
4	72 °C	10 min		
5	10 °C	forever		

Table 9: Genotyping PCR cycling temperatures and duration

The primer pair for/wt_rev amplified a 348 bp fragment for the WT allele and the primer pair for/ko_rev a 762 bp fragment for the KO allele.

Agarose gel electrophoresis

PCR products were separated by horizontal gel electrophoresis (Amersham Bio-Sciences). Depending on the size of PCR fragments for separation, agarose concentration in the gels varied between 1-2 %. Briefly, agarose (Invitrogen) was boiled in 1 x TAE buffer (40 mM Tris-acetate, 1 mM EDTA), 0.5 µg/ml ethidium bromide was added and the gel was casted. DNA samples were prepared with 6 x DNA loading buffer (10 mM Tris-HCl, 30 % (v/v) glycerol, 0.25 % (v/v) bromphenol blue, 0.25 % (v/v) xylene cyanol). DNA fragments were separated in an electric field and the DNA with intercalated ethidium bromide was visualized under UV-light.

Cloning

Cloning of DNA fragments Targeting Vector and restriction digests

In order to obtain the DNA fragments of interest, PCR with corresponding primer pairs was performed on either human or mouse cDNA. PCR products were analysed by agarose electrophoresis to verify the correct molecular size. DNA bands of interest were excised and DNA was extracted using a DNA recovery kit (Zymoclean). For the cloning of DNA fragments into the appropriate vector, 1-2 µg of vector and 5 µg of insert were digested with restriction enzymes at the appropriate temperature using enzymes from Thermo Fischer and New England Biolabs. Vector DNA was dephosphorylated with 1000 U of alkaline phosphatase (Roche) for 60 min at 37 °C. Vector DNA was purified similar to the insert by gel electrophoresis and purified using the Zymoclean recovery kit.

DNA Ligation

For cloning DNA fragments into plasmid vectors, insert and vector fragments with compatible ends were ligated. As ligation efficiency depends on the ratio between insert to vector. The optimal ratio (insert:vector = 3:1) was calculated by taking the molecular weight of the respective DNA into account. A typical ligation mixture was performed in a volume of 20 µl with T4 DNA-Ligase (Thermo Fischer). The ligation mixture was incubated overnight at 4 °C and 3 µl of the ligation reaction were transformed into chemo-competent bacteria.

Generation of competent bacteria

For generating chemo-competent bacteria a culture of E. coli XL1 Blue was grown overnight at 37 °C in 2 ml ψ broth medium (LB-broth medium, 4 mM $MgSO_4$, 10 mM KCl, 3 µg/ml tetracycline, pH 7.0). The next day, 1 ml of the culture was inoculated into 500 ml ψ broth medium and grown at 37 °C until an optical density of 600 nm (OD600) was reached. Following cooling of the bacterial culture, bacteria were pelleted by centrifugation at 4000 g for 5 min at 4 °C. The supernatant was discarded and the pellet was resuspended in 150 ml ice-cold TFB1 buffer (15 % glycerol, 10 mM $CaCl_2$, 30 mM potassium acetate, 100 mM RbCl, 50 mM $MnCl_2$, pH 5.8). After incubation on ice for 1 h the bacterial suspension was centrifuged at 3000 rpm for 5 min at 4 °C. The supernatant was discarded and the pellet was resuspended in filtered sterile, ice-cold TFB2 buffer (15 % glycerol, 10 mM MOPS, 75 mM $CaCl_2$, 10 mM RbCl). Competent cells were divided into aliquots on ice and snap-frozen in liquid nitrogen and stored at -80 °C.

Transformation of competent bacteria

Plasmid DNA and 50 µl of chemo-competent bacteria were incubated on ice for 20 min. After a heat shock at 42 °C for 45 s the cells were cooled on ice for 1 min and 250 µl of SOC medium (0.5 % yeast extract, 2 % tryptone, 10 mM NaCl, 2.5 mM KCl, 10 mM $MgCl_2$, 10 mM $MgSO_4$, 20 mM glucose, pH 7.0) were added and incubated at 37 °C on a shaker for 1 h. The mixture was centrifuged at 4000 rpm for 5 min. After removing 250 µl of the supernatant, the pellet was resuspended in the remaining SOC medium and the suspension was plated on LB-Agar plates containing the appropriate antibiotic for plasmid selection. Inverted plates were incubated at 37 °C overnight.

Mini preparation of plasmid DNA from bacterial colonies

A single bacterial colony was inoculated in 2 ml of LB medium containing antibiotics. The culture was grown overnight at 37 °C with shaking. Next day, bacteria were pelleted by

centrifugation and DNA was isolated using the Mini-preparation Kit (Peqlab) following manufacturer´s instructions.

DNA sequencing

To verify that the reading frame and the nucleotide sequence of the cloned construct was correct, DNA samples were sent to Macrogen for Sanger sequencing.

Maxi Preparation of Plasmid DNA

To isolate high DNA quality and yield for transfections a Maxi preparation was performed. Bacterial precultures were inoculated into 250 ml LB medium with the respective antibiotic. After overnight incubation at 37 °C, bacteria were pelleted by centrifugation at 4000 g for 5 min and DNA was prepared using the Midi/Maxi Kit from Qiagen according to the manufacturer's instructions.

Protein isolation of cells and tissue lysates

Human AAMR quadriceps samples were obtained from Dr. Osvaldo Mutchinick (Mexico). Control quadriceps samples were obtained from the Telethon Biobank (Italy). Following the operation the samples were immediately frozen on dry ice and stored at -80 °C.

Cells were harvested and lysed in RIPA buffer (50 mM TRis-HCl pH 7.4, 150 mM NaCl, 1 % NP-40, 1 % Sodium deoxycholate, 0.1 % SDS, 1 mM EDTA, and complete protease inhibitor (Roche). Tissue lysates were prepared with the Ultra-Turrax T8 tissue homogenizer (IKA-WERKE) of quadriceps muscles in RIPA buffer. After sonication homogenates were centrifuged at 14000 rpm to remove nuclei and insoluble debris. The supernatant was stored at -80 °C.

Western Blot

Proteins were denatured at 90 °C for 5 min in 1 x Laemmli sample buffer. After separation via SDS-polyacrylamide gel electrophoresis proteins were transferred onto PVDF membranes (Whatman). Membranes were blocked with 1 % bovine serum albumin (BSA, Sigma) in tris-buffered saline (TBS) buffer (50 mM Tris-Cl, pH 7.6, 150 mM NaCl) supplemented with 0.1 % Tween (Sigma) for 1 h at RT. Membranes were incubated with primary antibodies in according dilutions overnight at 4 °C. Primary antibodies were detected with a horseradish peroxidase-conjugated secondary anti-rabbit antibody (Amersham Bioscience) and the Super

Signal Western Blot Enhancer Kit (Thermo). The quantification of detected protein bands was done with *ImageJ*. All blots were repeated at least once.

Co-Immunoprecipitation

HEK-293T cells were maintained in DMEM (Invitrogen) supplemented with 10 % fetal bovine serum (FBS, Gibco), penicillin (100 UI/ml) and streptomycin (100 mg/ml) (P/S, Gibco). Cells were plated in dishes and after 24 h transfected with 15 µg/dish WT and 20 µg/dish mutant plasmid construct of human GMPPA-Myc, GMPPB-FLAG, GMPPA-T334P-Myc, GMPPA-N182D-Myc, FLAG-GMPPA, GMPPB-FLAG plasmids and/or Myc- tagged DNA constructs missing either the C-terminus or N-terminus: DNA was mixed with 15 µl lipofecftamine 2000 (Invitrogen) and 800 µl Optimem (Gibco) according to manufacturer's instruction. After incubation for 15 min at RT the mixture was added to the cells. After 24 h cells were harvested in lysis buffer (20 mM Imidazol pH 8.0, 150 mM NaCl, 2 mM $MgCl_2$, 300 mM sucrose, 0.25 % Triton X-100) and centrifuged at 14000 rpm to remove nuclei and insoluble debris. The supernatant was incubated with Myc- oder FLAG-coupled agarose beads overnight at 4 °C. The supernatant was then washed with lysis buffer 3 times and beads with bound proteins were boiled at 90 °C for 10 min in 1x Laemmli sample buffer and stored at -80 °C.

GST pull-down

Recombinant human GST-GMPPA, GST-GMPPB and MBP-GMPPA proteins were generated in *E. coli* cells using pGex4T1 and pMalC2X plasmids, harvested in Imidazol buffer and centrifuged at 14000 rpm. The supernatant was incubated with GSH beads for 45 min at 4 °C. The supernatant was then washed 3 times with Imidazol buffer (20 mM Imidazol pH 8.0, 150 mM NaCl, 2 mM $MgCl_2$, 300 mM sucrose, 0.25 % TritonX-100) and beads with bound proteins were boiled at 90 °C for 10 min in 1x Laemmli sample buffer and stored at -80 °C. GST pull-down experiments were conducted by Sonnhild Mittag.

Overlay assays

Tissue lysates were prepared with an Ultra-Turrax T8 tissue homogenizer (IKA-WERKE) of *Quadriceps* muscles in Tris-buffered saline buffer (TBS, 50 mM Tris-Cl, pH 7.6, 150 mM NaCl) supplemented with 1 % Triton X-100 (Sigma). After sonication homogenates were centrifuged at 14000 rpm at 4 °C to remove nuclei and insoluble debris. The supernatant was stored at -80 °C. Dystroglycan was precipitated using the Pierce Glycoprotein WGA or Con A

isolation kit (Thermo Fischer). After separation via SDS-polyacrylamide gel electrophoresis proteins were transferred onto PVDF membranes (Whatman). Membranes were blocked in Laminin-binding buffer (10 mM triethanolamine, 140 mM NaCl, 1 mM $MgCl_2$, 1 mM $CaCl_2$, pH 7.6) containing 5 % non-fat dry milk. Membranes were incubated with either 160 µg Laminin (Sigma) or 40 µg Agrin (LSBio) followed by incubation with primary and secondary antibodies and ECL detection.

Mass spectrometry

Homogenized *Quadriceps* muscle samples were lysed in RIPA buffer followed by reduction, alkylation and subsequent acetone precipitation. Protein pellets were digested into peptides, labeled with 10plex Tandem Mass Tags (Thermo Fisher) and fractionated by high pH reverse phase chromatography, as previously described (Heinze et al. 2018). The resulting fractions were combined into 24 pools and analysed in an Orbitrap Fusion Lumos Tribrid Mass Spectrometer (Thermo Fisher) using a synchronous precursor selection (SPS)/MS3 method (McAlister et al. 2014). Raw data were processed using Proteome Discoverer v2.0 (Thermo Fisher) and searched against a Uniprot mouse database using Mascot v2.5.1 (Matrix Science). Differential expression analysis was performed using limma (Ritchie et al. 2015) and additional procedures written in R. Mass spectrometry was performed by Svenja Schüler.

Histological analysis

Tibialis anterior muscles were sectioned into 5 µm thick sections with a Cryotome (Kryostar NX70, Thermo Scientific). Brain tissue was cryo-sectioned into 8 µm thick sections. For histological analysis sections were stained with hematoxylin/eosin according to the manufacturers' protocols (Sigma-Aldrich). Images were captured with a Zeiss AxioLab A1 microscope and further analyzed by *ImageJ*.

Centralized nuclei and fiber diameter were measured using *ImageJ* software. The fiber diameter of skeletal muscle cross sections from young and old animals was analyzed by Juliane Jung.

Immunofluorescence (IF) stainings were performed in Shandon chambers (Thermo Scientific). Sections were fixed with 4 % paraformaldehyde (PFA) and rinsed in phosphate-buffered saline (PBS). 0.25 % Triton-X in 1x PBS was used to permeabilize the cells. After adding blocking solution (5 % goat serum in PBS or 5 % milk in PBS) for 1 h, primary antibody solution (in 1 % goat serum in PBS or 1 % milk in PBS) was applied overnight and secondary antibody solution (in blocking solution) was applied for 2 h. Nuclei were stained

with DAPI 1:10000 (Invitrogen). Images were taken with a Zeiss LSM880 with Airyscan microscope with the Z-stack module. Z-projections with average intensity processed with *ImageJ* are shown. Images were processed identically for *ImageJ*-analysis.

Human AAMR quadriceps samples were obtained from Dr. Osvaldo Mutchinick (Mexico). Control quadriceps samples were obtained from the Telethon Biobank (Italy). Samples were immediately frozen on dry ice after operation and stored at -80 °C. For IF stainings, samples were cryo-sectioned into 5 µm thick sections and followed normal IF protocol as described above.

NMJ preparation

The *Musculus tibialis anterior* was fixed in 4 % PFA for 30 min and washed with 1 x PBS. Fiber bundles consisting of 4-5 myofibers were prepared and used for further analyses. After permeabilization in PBS with 0.1 % Triton-X 100 overnight samples were incubated with 5 % horse serum for 1 h followed by an incubation with with α-bungarotoxin-Alexa 555 (BTX, Invitrogen) 1:500 and an antibody detecting neurofilament (2H3, DSHB, 1:2) and synaptic vesicle 2 (SV2, DSHB 1:2) overnight at 4 °C. After washing with PBS, single myofiber bundles were incubated with the corresponding secondary antibodies (Invitrogen) in a dilution of 1:1000 for 1 h at RT. Nuclei were stained with DAPI (Invitrogen, 10 µg/ml). Muscles were washed with PBS and mounted with Prolong Gold anti-fade mounting medium (Invitrogen). Images were taken with a Zeiss Axio Observer microscope. NMJ preparation was performed by Julia von Maltzahn.

Skeletal muscle fiber bundle stainings

Muscles (*Musculus Tibialis anterior*) were fixed in 4 % PFA and washed with 1 x PBS. Following incubation in PBS with 0.25 % Triton X-100 (Sigma) overnight at 4 °C, fiber bundles were prepared. After blocking in 5 % normal goat serum fiber bundles were incubated with primary antibodies TGN38, GLG1 and GM130 overnight at 4 °C. After washing with 1 x PBS fiber bundles were incubated with the corresponding secondary antibodies. Fiber bundles were washed with PBS and mounted with Fluoromount-G (Southern Biotech). Images were taken with a Zeiss LSM880 Airyscan confocal microscope with the Z-stack module. Images were further analyzed with *ImageJ*. For intensity measurements, the integrated density was used. The integrated density is the product of area and mean gray value (gray value: each pixel in an image is one sample representing a specific amount of light) and is therefore more meaningful than only the area or mean gray value. Co-localization analysis was performed with the Coloc2 module in *ImageJ*. Manderson

overlap and Pearson correlation coefficients were used for co-localization quantifications. Both coefficients are mathematically very similar. The Pearson correlation coefficient uses the deviation from the mean. The Manderson overlap coefficient uses absolute intensities and is insensitive to noise (see *ImageJ* web-page www.fiji.sc).

Glycome analysis

Mice were fasted for 24 h. *Quadriceps* muscle tissue was thawed at 4 °C and all steps of protein extraction was executed at 4 °C to prevent protein degradation. The tissue was cut into small pieces with a scalpel and transferred into reaction tubes. Tissue lysis was performed in lysis buffer (50 mM Tris-HCl, 100 mM NaCl, 1 mM EDTA and proteinase inhibitor cocktail). Samples were vortexed vigorously, 30 min incubated on ice and sonicated twice for 45 s (80 % amplitude, 0.5 cycles). Lysates were spun down at 4847 rpm at 4 °C for 10 min and the supernatant was recovered. Protein concentrations were determined using the Pierce BCA Protein Assay Kit (Thermo Scientific) according to the manufacturer´s manual. For *N*-glycan analysis, about 200 µg proteins were dissolved in 40 µl 250 mM phosphate buffer pH 6.5 (250 mM NaH_2PO_4, 250 mM Na_2HPO_4) and SDS was added to a final concentration of 1 %. The protein was denatured by incubation at 95 °C for 5 min. The buffer was diluted to 160 mM with water and Ipegal at a final concentration of 1 %. Next, *N*-glycan release was performed using 1 U of PNGase F (N-Zyme Scientifics) was added to the protein and incubated overnight at 37 °C. *N*-Glycans were subsequently cleaned up, permethylated to neutralize the negative charge of sialic acids and measured by MALDI-TOF mass spectrometry. MALDI-TOF spectra were acquired in *m/z* 1000–5000 region in the positive ion mode [M+Na]$^+$ using 10000 laser shots at a frequency of 100 Hz. Detector gain was set up to 1722 V and the analog offset was 51 mV.

For *O*-glycan analysis, about 200 µg proteins were dissolved in 40 µl 250 mM phosphate buffer pH 6.5 (250 mM NaH_2PO_4, 250 mM Na_2HPO_4) and SDS was added to a final concentration of 1 %. The protein was denatured by incubation at 95 °C for 5 min. The buffer was diluted to 160 mM with water and Ipegal at a final concentration of 1 %. After chemical release with NaOH/NaBH4 *O*-glycans were purified over self-made C18/Dowex H$^+$ column followed by a methanolic desalting step in the vacuum centrifuge and permethylation reaction. The spectra were acquired in *m/z* 300–2000 region in the positive ion mode [M+Na]$^+$. For every spectrum acquisition, 10000 shots were collected. The spectra were acquired at 100 Hz frequency. Detector gain was set up to 1638 V and the analog offset was 51 mV. Glycome analysis was performed by Karina Biskup.

Proximity ligation assay

Proximity ligation assay (PLA) was performed with the Duolink in situ red starter kit mouse/rabbit (DUO92101) according to the manufacturer´s instructions (Sigma) with rabbit GMPPA (Proteintech) and mouse GMPPB (Novus Biologicals) antibodies in a 1:25 dilution.

EM microscopy of human samples

Human AAMR quadriceps and control samples were obtained from Dr. Osvaldo Mutchinick (Mexico). The biopsies were immediately immersed in 2.5 % glutaraldehyde (EMS Cat 16210) for 5 h, followed by two washes in cacodylate buffer (EMS Cat 21300) at pH 7.2 and 0.15 M and post-fixation done in 1 % osmium tetraoxide (EMS Cat 19100) for 45 min, followed by two washes in cacodylate buffer and tissue dehydrated in the following progressive ethyl alcohol concentrations at 30 %, 50 %, 70 %, 80 %, 96 % and 100 % for 20 min each. For an adequate infiltration, muscle samples were changed to propylene oxide (EMS Cat 20401) for 45 min. The infiltration was carried out with epoxy resin diluted in propylene oxide 1:2, 1:1 for 4 h in each solution and pure resin for 8 h. The procedure described was carried out in a Leica EM TP automatic processor. For the polymerization of the resin samples were incubated at 55 °C for 24 h. Processed biopsies were cut in 75 nm thick sections and mounted on 200 mesh copper grids. The contrast was attained with 5 % uranyl acetate (EM Grade) and lead citrate with Reynold's method, and the samples analyzed in a Transmission Electron Microscope FEI model Tecnai BioTwin at 80 kV.

EM microscopy was performed by Braulio Martínez.

EM microscopy of murine sciatic nerve

Mice were perfused transcardially with 4 % PFA and 2.5 % Gluaraldehyde in PBS. Sciatic nerve was removed and post-fixed in 4 % PFA and 2.5 % Gluaraldehyde in PBS overnight. Afterwards, nerves were washed 6 times with 0.1 M cacodylate buffer pH 7.3 and post-fixed in 0.1 M cacodylate buffer containing 2 % osmium and 1 % potassium ferrocyanide for 2 h at 4 °C followed by four washes in 0.1 M cacodylate buffer and 3 times distilled water. Tissue was dehydrated in the following progressive acetone concentrations at 30 %, 50 %, 70 %, 90 % and 95 % for 30 min each and 3 times 100 % for 45 min each. For contrast, 1 % uranyl acetate was added to 50 % acetone. The infiltration was carried out with epoxy resin diluted in acetone 1:3, 1:1, 3:1 for 45 min in each solution and pure resin for 3 h. The polymerization of the resin was made at 60 °C for 48 h. Processed biopsies were cut in 50 nm thick sections (Reichert Ultracut S, Leica) analyzed in a Transmission Electron Microscope JEM 1400 (Jeol) at 80 kV. EM microscopy was conducted by Katrin Buder.

COS-7 cell culture and transfection for immunohistochemistry

COS-7 cells were maintained in DMEM (Invitrogen) supplemented with 10 % FBS (Gibco), penicillin (100 UI/ml) and streptomycin (100 mg/ml) (P/S, Gibco). Cells were plated on coverslips and 24 h later transfected with 1 µg DNA/well/ plasmid construct in 24-well plates with lipofectamine reagent 2000 (Invitrogen) according to the instructions of the manufacturer. 24 h post-transfection cells were fixed for 15 min in 4 % PFA at RT and immunocytochemistry was performed as described above.

Myoblast experiments

For cycloheximide (CHX) experiments, primary myoblasts were seeded in growth medium (F10 medium (Gibco), 20 % FBS (Gibco), 2 % pentamycin/streptomycin (P/S, Gibco), 2.5 ng/ml bFGF (Gibco)) on collagen-coated culture dishes. The following day, cells were treated with differentiation medium (DMEM (Sigma), 2 % HS (Gibco), 2 % P/S (Gibco)) and allowed to differentiate for two days. Then, cells were transfected with 30 pmol siRNAs (for a 6-well plate) against either control (*siScr*) (Dharmacon), *Dystroglycan* (*siDag1*) (Dharmacon) or *Gmppa* (*siGmppa*) (Novus Biologicals). After 3 days, cells were treated with 8 µg/ml cycloheximide for 24 h. Then, cells were harvested with RIPA buffer. After sonication homogenates were centrifuged at 16900 g to remove nuclei and insoluble debris. The supernatant was stored at -80 °C. Myoblast seeding was performed by Henriette Henze.

Sugar content determination

Sugar concentration was determined using the Megazym kit for measuring D-mannose, D-fructose and D-glucose following manufacturer´s instructions.

GDP-mannose measurements

Mice were sacrificed, organs dissected out and immediately frozen in liquid nitrogen. Organ homogenates were run on high-performance liquid chromatography with a modified gradient to enhance separation of NDP-sugars as described previously (Koehler et al. 2013).
GDP-mannose measurements were performed by Takfarinas Kentache.

Statistical analysis

For statistical analysis, raw data were analyzed for normal distribution with the Kolmogorov-Smirnov test or with graphical analysis using the Box-Plot and QQ-Plot. As these tests suggested normal distribution 1-way ANOVA, 2-way ANOVA and T-Test were used with * indicating $p < 0.05$, ** indicating $p < 0.005$ and *** indicating $p < 0.0005$. For all data, the mean with standard error of the mean are shown.

Results

Generation of *Gmppa* KO mice

To unravel the pathophysiology of AAMR syndrome we created a *Gmppa* KO mouse line. For this purpose we selected the ES cell clone EPD0621_7_G03 obtained from EUCOMM harboring a cassette consisting of a β-galactosidase reporter gene (LacZ), a neomycin resistance (NeomR), loxP and Frt sites (Fig. 5a). ES-cells with this clone were injected into donor blastocysts, which were transferred into foster mice. Resulting chimeric mice were analyzed by Southern blot (Fig. 5b, c). Chimeric mice were mated with FLPe-deleter mice (Rodríguez et al. 2000) to remove the LacZ cassette. After mating these mice with Cre-deleter mice (Schwenk et al. 1995) the offspring showed a heterozygous deletion of exon 5. Heterozygous offspring was subsequently mated in order to create homozygous knockout mice. The homozygous offspring was born in the expected Mendelian ratio.

The predicted aberrant *Gmppa* KO transcript leads to a frameshift with premature termination and thus a truncated protein (Fig. 5a). Real time PCR showed a significant reduction of *Gmppa* transcript abundance in *Gmppa* KO mice compared to WT littermates suggesting nonsense-mediated decay of the recombinant transcript (Fig. 5d). As expected, we detected a band of the appropriate size in different WT tissues but not in KO tissues with a commercial polyclonal antibody against the GMPPA protein (Fig. 5e). GMPPB protein bands were detected in *Gmppa* WT and KO tissue lysates at equal amounts (Fig. 5e).
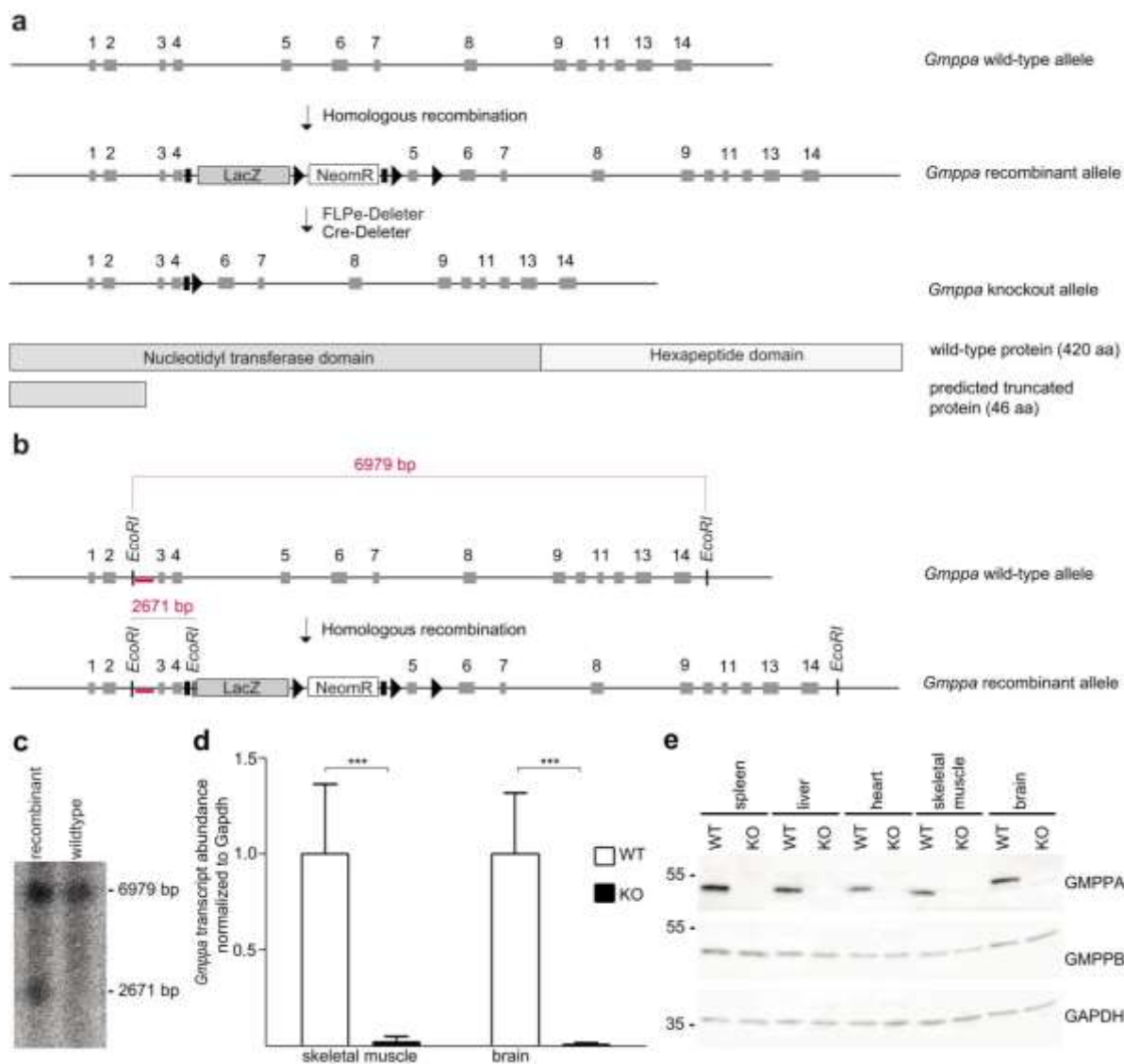
Fig. 5: Targeted disruption of the murine *Gmppa* gene. a) Genomic structure of the *Gmppa* locus and the predicted mutant protein as compared to WT GMPPA. Grey rectangles: exons, black rectangles: Frt sites, black triangles: loxP sites, LacZ: β-galactosidase cassette, NeomR: neomycin fusion cassette. **b)** Genomic structure of the WT and targeted *Gmppa* locus with *Eco*RI restriction sites, location of the Southern probe and the expected Southern blot fragments. Grey rectangles: exons, black rectangles: Frt sites, black triangles: loxP sites, LacZ: β-galactosidase cassette, NeomR: neomycin resistance cassette, red rectangles: probe-binding site. **c)** Southern blot analysis of the *Gmppa* locus of a WT and heterozygous knockout mouse exploiting the *Eco*RI restriction sites and the probe displayed in a). The probe detects a WT fragment at 6979 bp and a recombinant fragment at 2671 bp as expected. **d)** *Gmppa* transcript abundance is decreased in skeletal muscle and brain lysates in KO mice (n=3). **e)** The GMPPA protein can be detected in different tissues of WT mice, but is absent in samples of KO mice. The abundance of GMPPB is not altered in *Gmppa* KO mice. GAPDH served as loading control.

GMPPA interacts with GMPPB

GMPPB catalyzes the formation of GDP-mannose, a key substrate for the glycosylation pathway. GMPPA does not show catalytic activity, but it binds GDP-mannose. Because of

these features, we hypothesized that GMPPA might act as an allosteric feedback inhibitor of GMPPB (Koehler et al. 2013). To confirm our hypothesis that GMPPA serves as a regulatory subunit of GMPPB, we wanted to assess whether human GMPPA interacts with GMPPB. Therefore, we performed co-immunoprecipitation experiments after heterologous expression of Myc-tagged GMPPA and FLAG-tagged GMPPB in HEK-293T cells.

Immunoprecipitation (IP) with agarose beads coupled to an antibody against the FLAG-tag revealed that GMPPB-FLAG and GMPPA-Myc co-precipitate (Fig. 6a). IP with agarose beads coupled to an antibody against the Myc-tag further confirmed that GMPPA-Myc and GMPPB-FLAG interact (Fig. 6b). Notably, the N-terminal disease-associated variant GMPPA Myc G182D co-precipitated with GMPPB-FLAG while the C-terminal disease-associated variant GMPPA-Myc T334P did not (Fig. 6b). In contrast, the mutant protein GMPPB-FLAG D334N with the amino acid substitution in the C-terminal part of GMPPB was able to precipitate GMPPA-Myc (Fig. 6b).

Next, we performed immunoprecipitation experiments with Myc-tagged GMPPA and GMPPB mutant proteins lacking either the C- or the N-terminal part, and FLAG-tagged GMPPA and GMPPB WT constructs. The variant missing the N-terminal part of GMPPA showed an interaction with GMPPB, whereas the variant lacking the C-terminal part of GMPPA did not show any interaction (Fig. 6c). In contrast, the variant missing the N-terminal part of GMPPB did not co-precipitate GMPPA whereas the variant lacking the C-terminal part of GMPPB did co-precipitate GMPPA (Fig. 6d).

Our immunoprecipitation studies showed an interaction of overexpressed GMPPA with GMPPB. To investigate if the interaction is direct or indirect, we performed GST pull-down assays with recombinant GMPPA and GMPPB constructs.

Pointing to a direct interaction between GMPPA and GMPPB recombinant GMPPA-MBP was pulled down with immobilized GMPPB-GST (Fig. 6e).

Fig. 6: GMPPA directly interacts with GMPPB. a) GMPPA-Myc and GMPPB-FLAG co-precipitate upon co-overexpression in HEK-293T cells. **b)** The N-terminal disease-associated variant GMPPA G182D precipitates with GMPPB, while this is not the case for the C-terminal variant GMPPA T334P. **c)** The N-terminal but not the C-terminal GMPPA deletion construct co-precipitates with GMPPB. **d)** The C-terminal but not the N-terminal GMPPB deletion construct co-precipitates with GMPPA. **e)** GST pull-down of recombinant GMPPA and GMPPB points to a direct interaction of GMPPA with GMPPB. GST pull-down assays were performed by Sonnhild Mittag.

In COS-7 cells, we analyzed the localization of heterologous expressed human GMPPA and GMPPB proteins as well as the mutant variants. Both GMPPA and GMPPB showed a diffuse cytoplasmic expression pattern (Fig. 7a) which was altered upon transfection with the GMPPA mutants G182D and T334P (Fig 7b, c). The GMPPA point mutant G182D showed a more clustered staining, while the point mutant GMPPA T334P revealed a dotted staining. For both variants a co-localization with GMPPB was observed, although the co-localization

was more prominent for the G182D variant (Fig. 7b, c). The GMPPB point mutant D334N showed a dotted staining pattern and partially co-localized with GMPPA (Fig. 7d). The variant missing the N-terminal part of GMPPA showed a diffuse cytoplasmic co-localization with GMPPB (Fig. 7e), while the variant missing the C-terminal of GMPPA showed a dotted staining and no co-localization with GMPPB (Fig. 7f). The mutant lacking the C-terminal part of GMPPB revealed a diffuse cytoplasmic co-localization with GMPPA (Fig. 7g), whereas the mutant missing the N-terminal part of GMPPB showed a dotted staining with no co-localization with GMPPA (Fig. 7h).

These data suggest that the C-terminal part of GMPPA is necessary for its localization and its interaction with GMPPB, while the N-terminal part of GMPPB is necessary for its localization and interaction with GMPPA. Therefore, the localization of GMPPA and GMPPB are highly linked and mutations in one protein can affect the localization of the other WT protein.
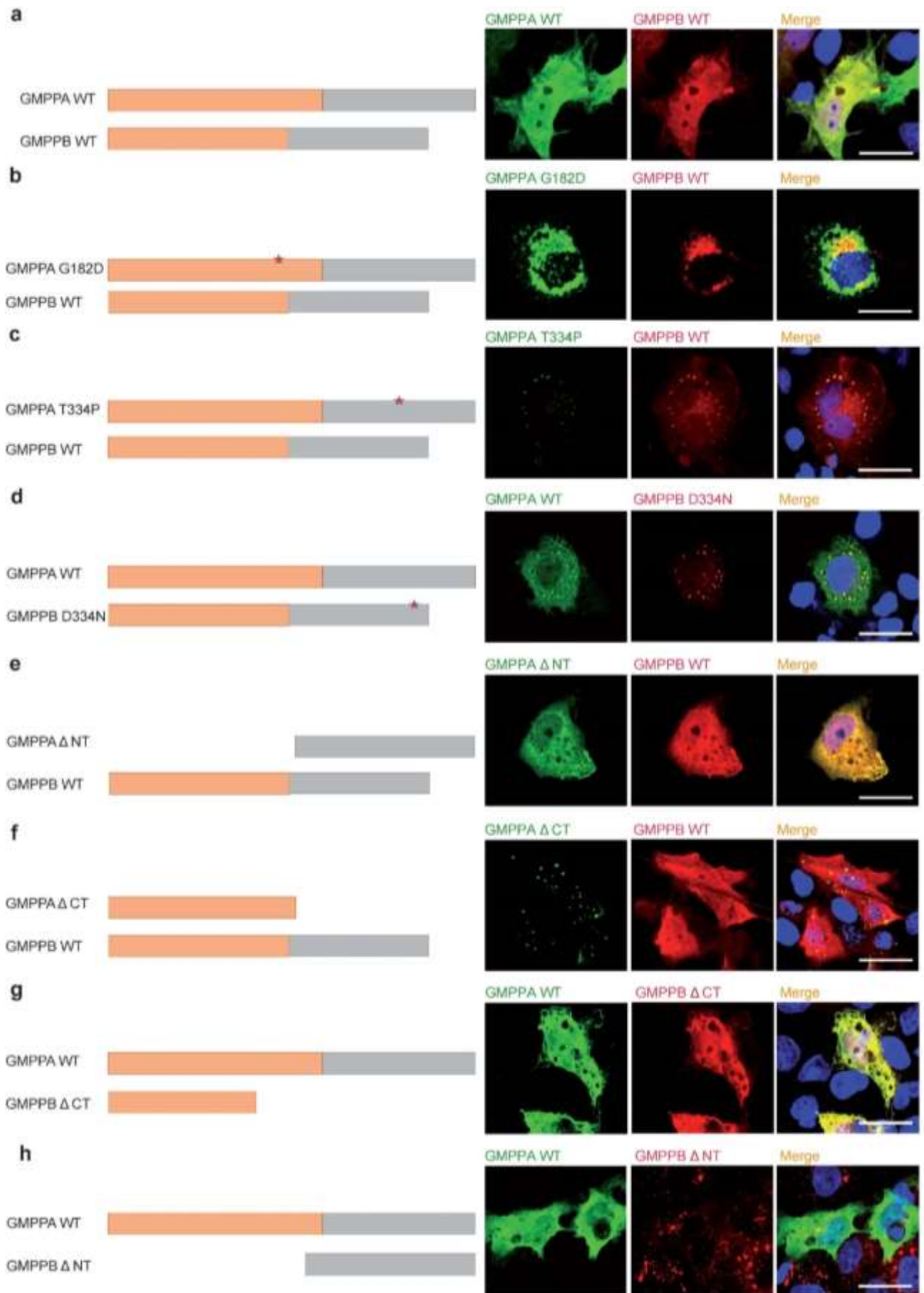
Fig. 7: Localization of WT and mutant GMPPA and GMPPB. GMPPA has a putative GDP-mannose binding domain at the N-terminus (nude) and several hexapeptide domains in the C-terminal part (grey). GMPPB has a nucleotidyl-transferase domain in the N-terminal part (nude) and hexapeptide repeats in the C-terminal part

(grey). GMPPA and GMPPA point mutations are indicated with red asterisks. GMPPA and GMPPB domain mutants are displayed in varying sizes according to the missing domain. WT GMPPA consists of 420 aa and WT GMPPB of 360 aa. **a - h)** Immunostainings of overexpressed WT and mutant GMPPA and GMPPB constructs showing **a)** a diffuse cytoplasmic co-localization of GMPPA and GMPPB WT proteins in COS-7 cells, while **b - d)** the staining pattern of GMPPA and GMPPB variants is altered. **e)** A variant missing the N-terminal part of GMPPA shows a diffuse co-localization with GMPPB in COS-7 cells, while **f)** a variant missing the C-terminal part displays a dotted staining and no co-localization with GMPPB. **g)** A variant missing the C-terminal part of GMPPB reveals a diffuse co-localization with GMPPA in COS-7 cells, whereas **h)** a variant missing the N-terminal part of GMPPB suggests a dotted staining of GMPPB and no co-localization with GMPPA (scale bars: 25 µm).

To confirm a direct interaction of both proteins in native tissue, we performed a proximity ligation assay (PLA) on murine skeletal muscle cross sections (Fig. 8a) and brain sections (Fig. 8b - d) with antibodies directed against either GMPPA or GMPPB.

The fluorescent amplification signal obtained from the oligonucleotide labeled antibodies directed against the primary antibodies, which indicates proximity of the targets of less than 40 nm, was present in WT sections, but not in KO sections (Fig. 8a - d).
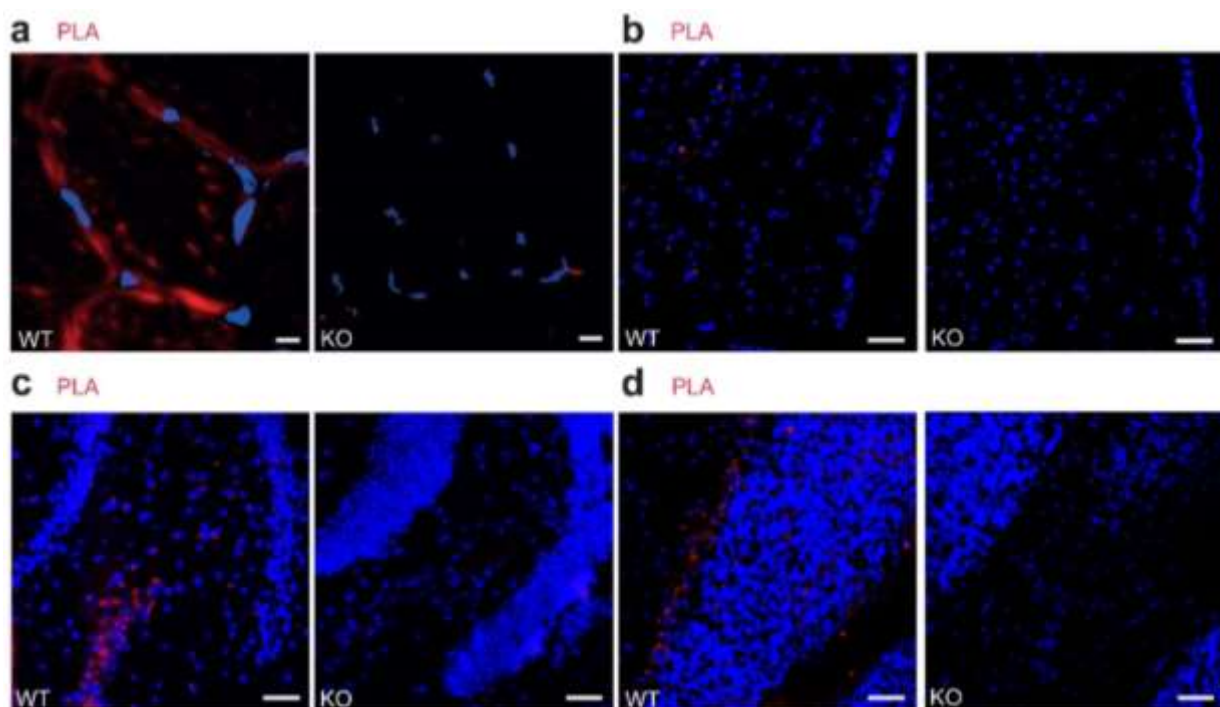
Fig. 8: Visualization of the co-localization of endogenous GMPPA and GMPPB. a - d) Proximity ligation assay (PLA) on murine sections with antibodies directed against GMPPA and GMPPB. **a)** PLA on skeletal muscle cross sections reveals signals in WT but not in KO sections (scale bar: 5 µm). **b - d)** PLA on brain sections shows a staining in WT but not in KO sections in **b)** the cortex, **c)** the CA3 region of the hippocampus and **d)** the Purkinje cell layer in the cerebellum (scale bars: 50 µm).

Gmppa KO mice do not show obvious signs of achalasia or alacrima up to 5 months of age

As patients with mutations in the _GMPPA_ gene show congenital achalasia and alacrima (Koehler et al. 2013, Gold et al. 2017), we asked whether _Gmppa_ KO mice recapitulate these deficits. We could not detect any macroscopic changes of the esophagus (Fig. 9a) in 5-months-old mice. HE staining of longitudinal sections of the stomach and esophagus from 5-months-old WT and KO mice revealed no dilation of the esophagus or a constricted esophageal sphincter (Fig. 9b). Moreover, the HE staining of esophageal cross sections from 5-months-old mice did neither show differences between genotypes (data not shown). HE staining of cross sections of lacrimal glands from 5-months-old mice did not show any differences between WT and KO animals as well (Fig. 9c). However, Laminin staining of cross sections of the lacrimal glands from 5-months-old KO mice showed a blurrier staining compared to WT sections (Fig. 9d). In addition, we detected increased signal intensities with an antibody against Paucimannose in KO lacrimal gland sections suggesting an increased mannosylation of proteins (Fig. 9e).

Laminin stainings of esophageal cross sections did not show any differences between genotypes (Fig. 9f). As in lacrimal gland sections, we detected increased signal intensities for Paucimannose (Fig. 9g) and the glycosylation specific epitope of α-DG (Fig. 9h) suggesting increased protein glycosylation. Excluding a functional relevant achalasia, the body weight of _Gmppa_ knockout mice did not differ at 3 months of age and only decreased at a later age (Fig. 9i, j).
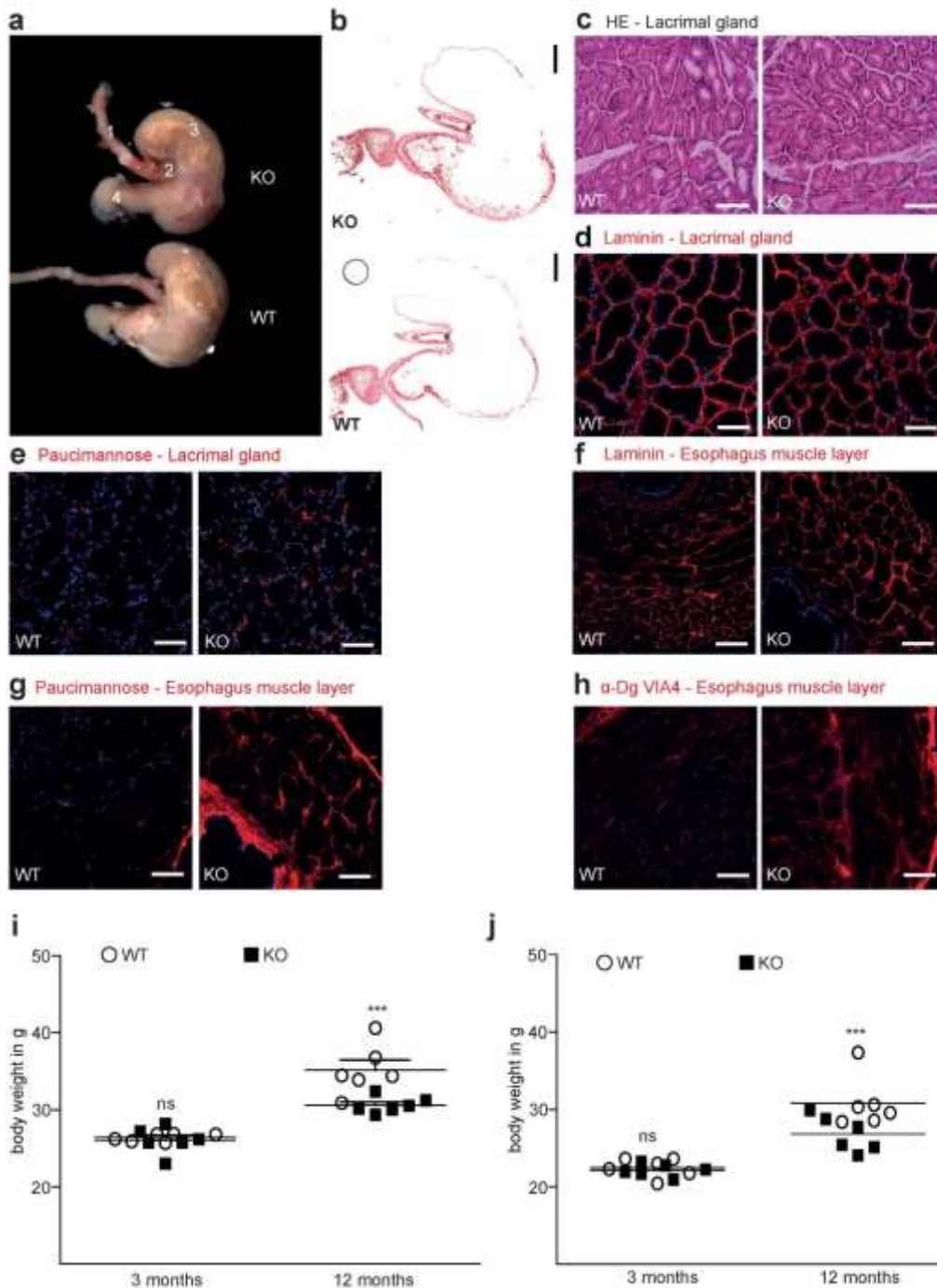
Fig. 9: *Gmppa* **KO mice do not show obvious signs of achalasia or alacrima up to 5 months of age. a)** Macroscopic organization of the stomach (3) with esophagus (1), esophageal sphincter (2) and pylorus (4) of 5-months-old WT and KO mice revealing no obvious changes. **b)** HE stainings of the stomach with esophageal sphincter show no alterations of the esophageal sphincter (indicated by asterix) in 5-months-old KO mice (scale bar: 50 µm). **c)** HE stainings of lacrimal glands from 5-months-old mice reveal no differences between genotypes (scale bar: 20 µm). **d)** Laminin signals appear blurrier in lacrimal gland cross sections of 5-months-old KO animals (scale bar: 20 µm). **e)** Paucimannose signals are increased in KO cross sections of lacrimal glands from 5-months-old mice (scale bar: 20 µm). **f)** Laminin signals are not changed between genotypes on esophageal cross sections, while **g)** Paucimannose and **h)** VIA4 signals are increased (scale bar: 20 µm, n = 3). Body weight does not differ at a young age of **i)** male and **j)** female mice. With increasing age, KO mice show a reduced body weight (n = 6).

Gmppa KO mice show neurological deficits

Patients with mutations in the *GMPPA* gene are mentally handicapped (Koehler et al. 2013, Gold et al. 2017, Benítez et al. 2018). Therefore, we aimed to assess whether *Gmppa* KO mice show cognitive deficits. To assess cognitive functions independent of motor impairment, we performed a *fear-conditioning* analysis. On the first day, we analyzed the freezing time when the mice were sitting in the box at baseline, then with the tone (for 20 s) and when the foot shock was applied (for 2 s at the end of the tone). All mice showed an increased freezing time after the foot shock (Fig. 10a). The next day, the *cued fear-conditioning* was assessed. Therefore, the mouse was placed in another box with different olfactory stimuli and different visual cues. We analyzed the freezing time at baseline (for 180 s), when the tone was applied (for 180 s) and when the tone was shut off (for 60 s). For 3-months-old mice we could not detect significant differences in the freezing time between WT and KO mice, although we observed a trend towards a decreased freezing time in KO mice (Fig. 10b). 12-months-old KO mice showed a significantly diminished freezing time compared to their WT littermates (Fig. 10b), but still showed an increased freezing time when the tone was applied (Fig. 10b) suggesting that older *Gmppa* KO mice were still able to connect the tone with the foot shock. In the third scenario, the *context fear-conditioning*, we put the mice into the same box as the day before with the same olfaction, light and decoration and analyzed the freezing time. Both, young and older KO mice showed a significantly decreased freezing time compared to their WT littermates (Fig. 10c) suggesting that *Gmppa* KO mice were not able to connect the environment with the foot shock applied the day before. While the amygdala is responsible for emotional learning, the hippocampus mediates short and long-term memory. It has been shown that lesions of the amygdala affect both *cued* and *context fear conditioning*, while hippocampal lesions only affect *context* but not *cued fear conditioning* (Phillips et al. 1992). Because we saw major differences between *Gmppa* WT and KO mice in the *context fear-conditioning*, our data are consistent with a compromised hippocampal function. As KO animals were still able to connect the tone with the foot shock, our data suggest a minor decline in amygdala function.
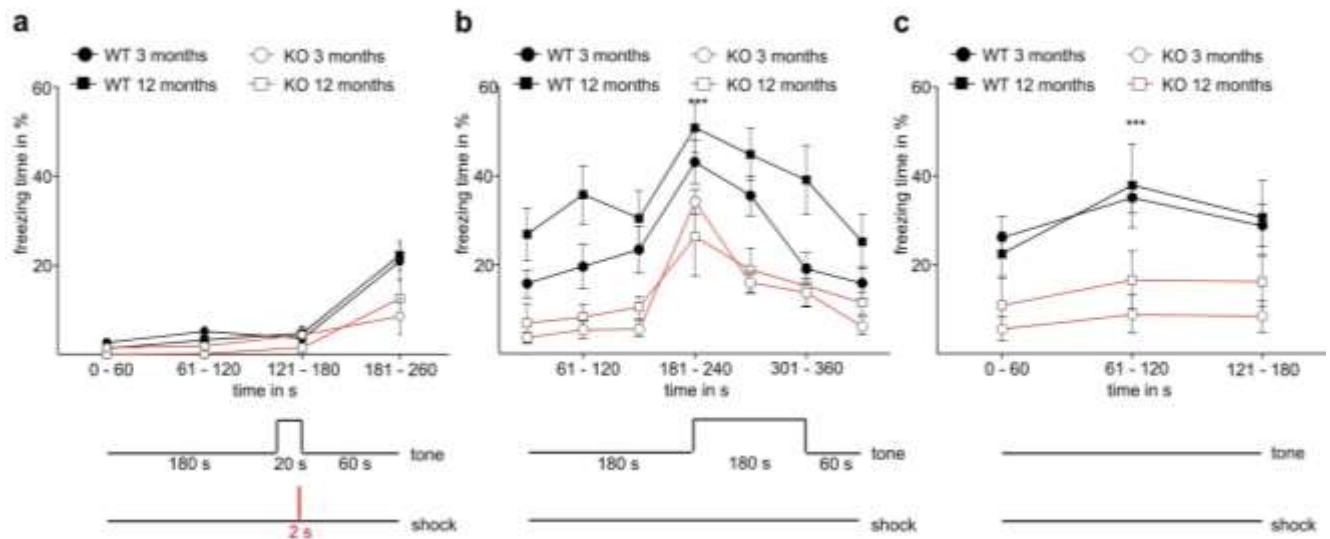
Fig. 10: *Gmppa* **KO mice show impaired memory in the** *fear-conditioning* **analysis. a)** Acquisition at day 1: The freezing time was measured before and after mice got a foot shock for 2 s (red line) paired with a tone for 20 s. **b)** 24 h after the acquisition, the cued test was performed: Mice were placed in a new environment compared to the day before and the freezing time upon tone stimulus was measured. KO mice showed a decreased freezing time compared to WT littermates (n (3 months) = 7 WT and 6 KO, n (12 months) = 8). **c)** After 2 h the context test was performed: Mice were placed in the same environment as the day before and the freezing time was measured. KO mice show a significantly decreased freezing time compared to their WT littermates (n (3 months) = 7 WT and 6 KO, n (12 months) = 8).

Based on these findings we assessed whether long-term potentiation (LTP) is modified in *Gmppa* KO animals. Stimulating electrodes where placed onto Schaffer collaterals (axon collaterals) in the CA3 of the hippocampus to stimulate CA1 pyramidal neurons. Recording electrodes were placed in the CA1 region (Fig. 4). Upon stimulation of the axons, field excitatory postsynaptic potentials (fEPSPs) were measured. Stimulation of the axons with different patterns and frequencies lead to long-lasting changes in postsynaptic potentials. We measured fEPSPs at baseline and after inducing LTP. KO mice showed a significantly decreased field excitatory postsynaptic potential (fEPSP) compared to their WT littermates (Fig. 11) suggesting a disturbed LTP.
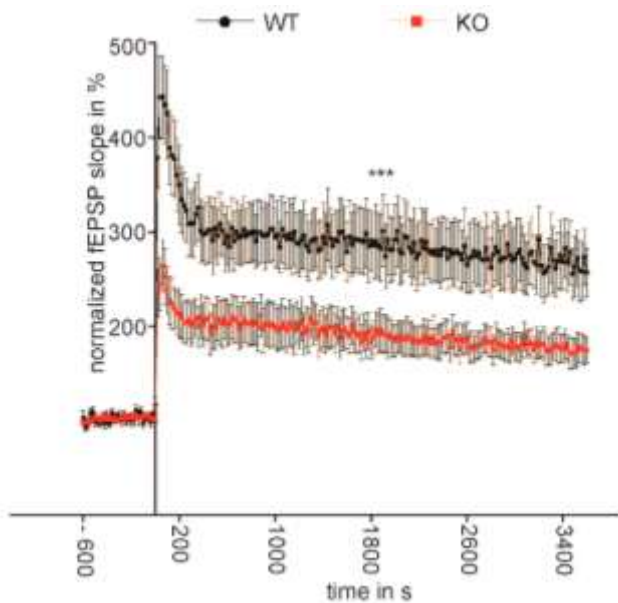
Fig. 11: *Gmppa* KO mice show a decreased long-term potentiation (LTP). *Gmppa* KO mice show a significantly decreased field excitatory postsynaptic potential (fEPSP) compared to their WT littermates (n = 10). LTP measurements were performed by Tanja Herrmann.

We then analyzed the brain weight of *Gmppa* WT and KO mice. In accordance to our previous findings, KO mice showed a significantly decreased brain weight compared to their WT littermates (Fig. 12a). Immunostainings of brain sections revealed increased signals for the glial fibrillary acid protein (GFAP) (Fig. 12b) and thinned cortex layers with less cells in KO sections (Fig. 12c, d) suggesting a cell loss accompanied by activation of astrocytes.
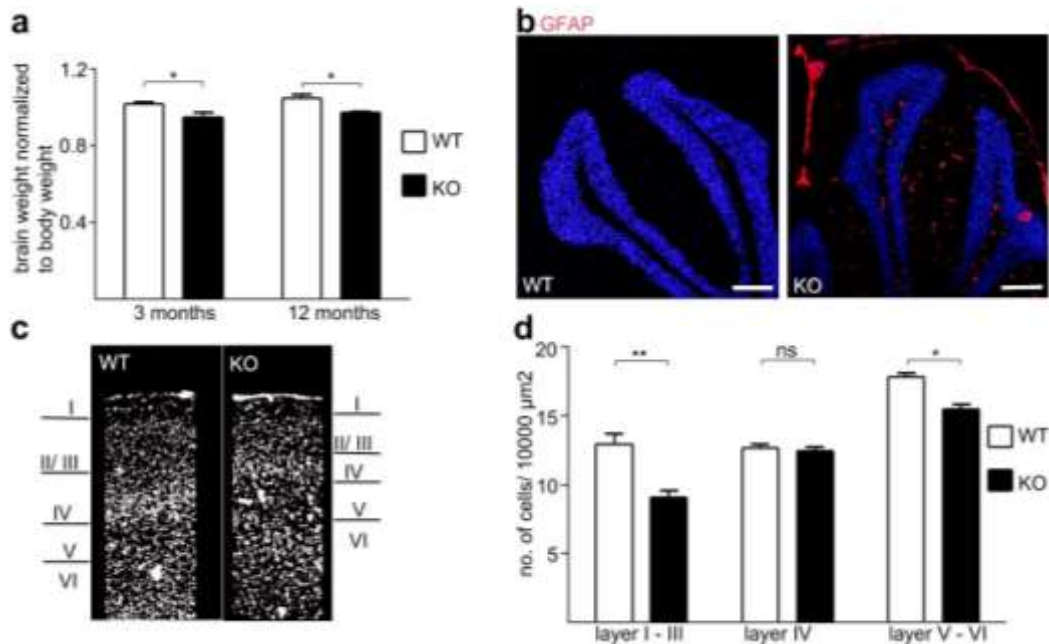
Fig. 12: *Gmppa* KO mice show brain alterations. a) Overall brain weight is reduced in KO mice at young and later ages (n = 6). **b)** Immunohistochemistry on murine sagittal brain sections reveals an increased signal for the

glial fibrillary acid protein (GFAP) in young KO sections (n = 3, scale bar: 200 µm). **c - d)** DAPI staining on sagittal brain sections reveals thinner cortical layers in 3-months-old KO brains (n = 3).

Moreover, *Gmppa* KO mice had a smaller cerebellum (Fig. 13a) and an altered hippocampal structure with a decreased cell number in the CA3 region at 3 months of age (Fig. 13b, c).
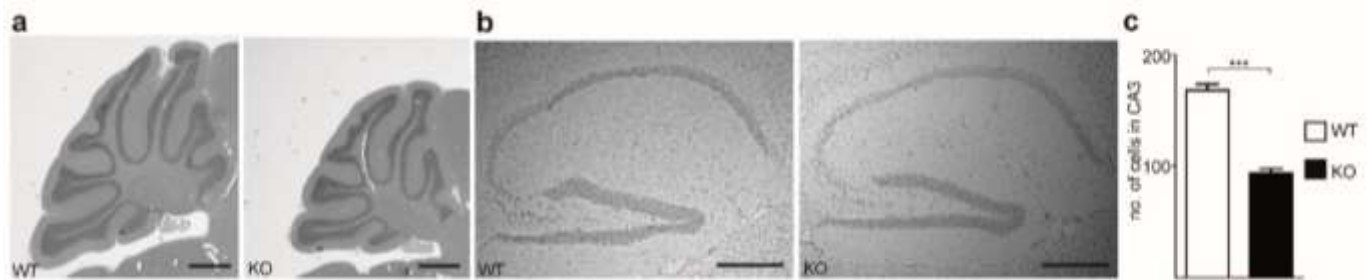
Fig. 13: *Gmppa* **KO mice show altered brain structures.** HE stainings of sagittal brain sections revealed **a)** a smaller cerebellum and (scale bar: 2 mm) **b - c)** less cells in the CA3 region of the hippocampus in 3-months-old KO mice (n = 3, scale bar: 500 µm).

The analysis of the brain of *Gmppa* KO mice is still ongoing.

Gmppa KO mice develop a progressive gait disorder with muscle weakness

Because AAMR patients often develop gait abnormalities (Koehler et al. 2013), we asked whether *Gmppa* KO mice display gait problems. To this end, we performed the *Beam Walk balance test* (Fig. 14a). The walk was analyzed using the FBA. The gait deficit of *Gmppa* KO mice was already visible at 3 months of age and further deteriorated with age (Fig. 14b).

To address the muscle strength of the fore-paws we performed the *Weights test* (Fig. 14c). Compared to WT littermates, the maximal weight held by the fore-paws was reduced in KO mice and further decreased with age (Fig. 14d).

We also performed the *Kondziela´s inverted screen test* (Fig. 14e). At 3 months of age, all mice independent of the genotype were able to hang on the screen for 70 s. Muscle weakness became evident at later ages, when KO mice fell off the screen more rapidly (Fig. 14f).
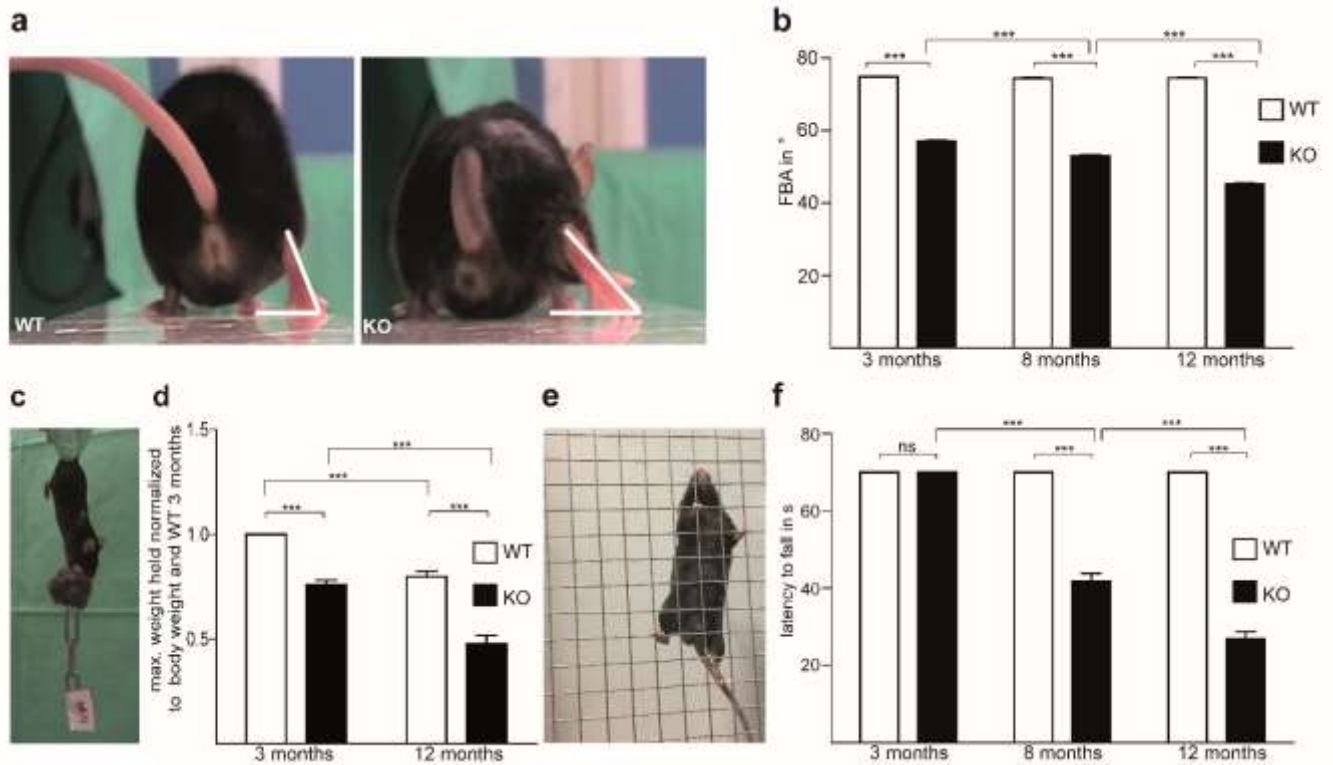
Fig. 14: *Gmppa* **KO mice develop a progressive gait disorder with muscle weakness. a - b)** *Beam Walk balance test*. **a)** Representative single video frames from a WT and a KO mouse 12 months of age walking on a beam at the moment when the toe is lifted. The foot base angle (FBA) is indicated by white lines. **b)** The FBA is decreased in KO compared to WT mice. The FBA decreases over time in KO, but not in WT mice (n = 12). **c - d)** *Weights test*. **c)** Representative image of a mouse holding a weight while lifted on the base of its tail. **d)** WT mice are able to hold more weight compared to their KO littermates and generally this ability decreases over time (n = 12). **e - f)** *Kondziela´s inverted screen test*. **e)** Representative image of a mouse hanging on an inverted screen. **f)** Older KO mice fall off the screen earlier as WT mice (n = 12).

Gmppa KO mice develop a progressive myopathy

To address the origin of the observed motor phenotype we analyzed skeletal muscles in more detail. At 3 months of age we could not detect differences in the muscle weight between WT and KO mice (Fig. 15b). However, at 12 months of age we observed an increased muscle loss for the *Musculus palmaris longus* of the fore-paws and *Musculus tibialis anterior* of the hind-paws (Fig. 15c). HE stainings of skeletal muscle sections revealed an increased number of centralized nuclei (Fig. 15a, d) and a decreased fiber diameter (Fig. 15a, e). These findings are consistent with a myopathic disorder.
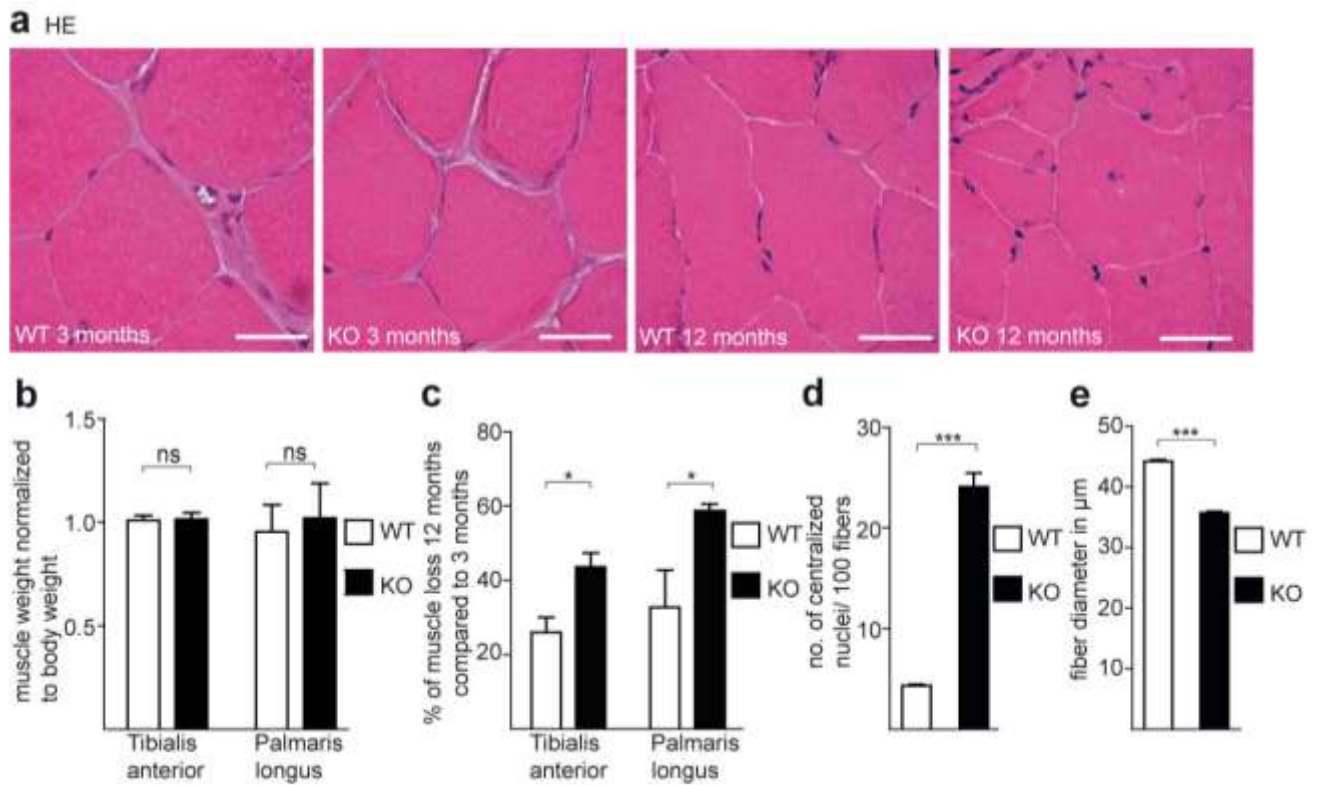
Figure 15: *Gmppa* KO mice develop a progressive myopathy. a) Cross-sectioned *Tibialis anterior* muscle stained with HE from 3-months-old WT and KO mice (n = 3, scale bars: 50 µm). **b)** At 3 months of age the muscle weight of the *Musculus tibialis anterior* and the *Musculus palmaris longus* does not differ between the genotypes (n = 5), while **c)** KO mice show a higher muscle loss compared to WT littermates at 12 months of age (n = 5). **d)** 12-months-old KO mice show more centralized nuclei and **e)** a decreased fiber diameter (n = 3). The fiber diameter was analyzed by Juliane Jung.

As the ECM provides structural and molecular support of skeletal muscle fibers and plays an important role in developmental and regenerative processes, we stained skeletal muscle cross sections for ECM proteins such as Laminin (Fig. 16a), Nidogen (Fig. 16b) and Collagen IV (Fig. 16c). At 3 months of age no obvious differences were noted between WT and KO mice, while at 12 months of age KO mouse sections demonstrated a more clustered staining for Laminin (Fig. 16a), Nidogen (Fig. 16b) and Collagen IV (Fig. 16c) suggesting a disorganization of the ECM upon *Gmppa* disruption. Importantly, overall protein abundance for Laminin, Nidogen and Collagen IV remained unchanged in skeletal muscle lysates as determined by immunoblot analysis (Fig. 16d, e).
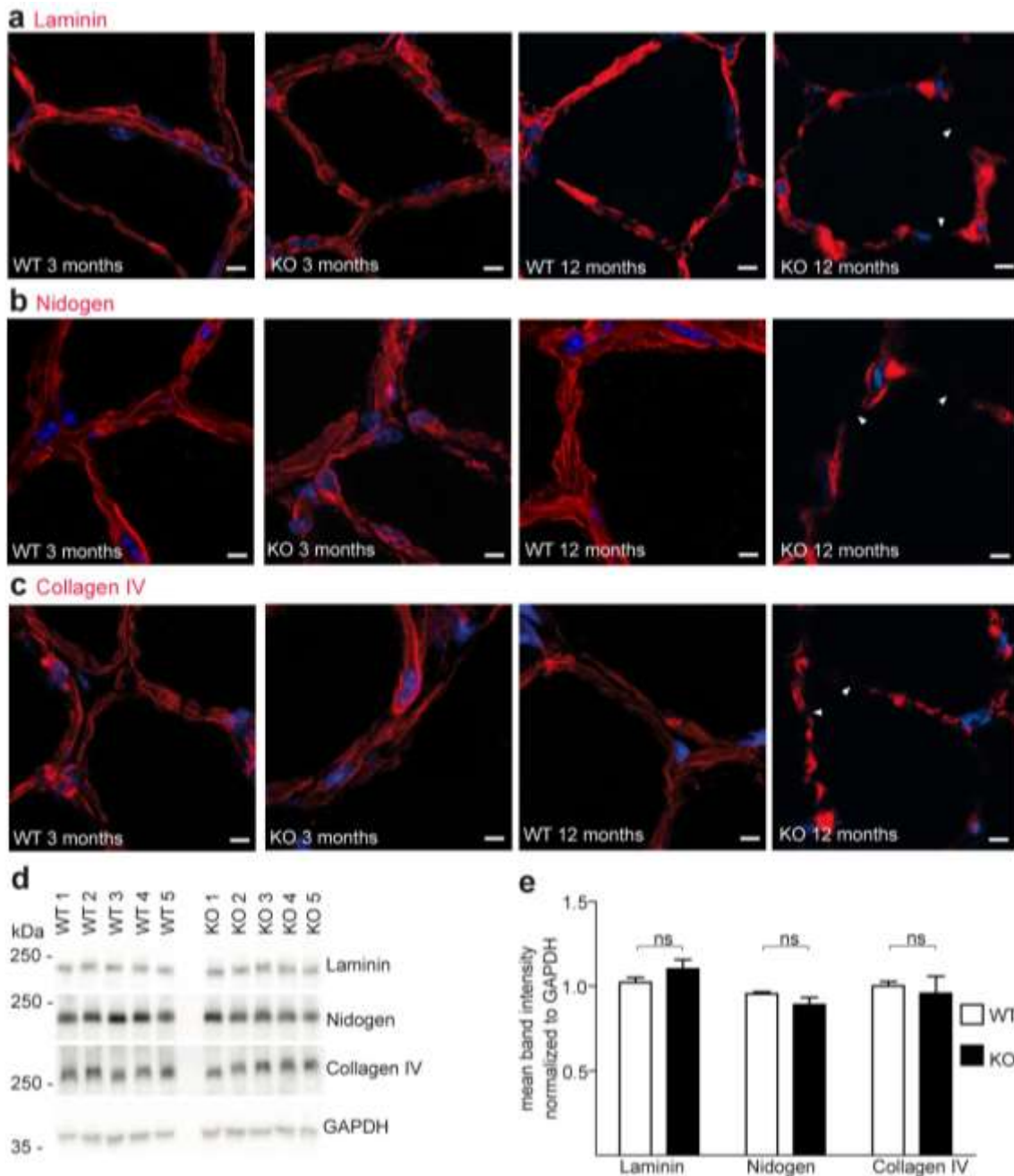
Figure 16: *Gmppa* **KO mice display ECM alterations. a - c)** Immunostaining on cross-sectioned *Tibialis anterior* from 3- and 12-months-old mice. **a)** The Laminin, **b)** Nidogen and **c)** Collagen IV staining is interrupted (marked with arrows) in older KO but not in WT mice (scale bars: 5 µm) while **d - e)** Laminin, Nidogen and Collagen IV levels were not changed. GAPDH served as loading control (n = 5).

As the ECM provides mechanical structure to myofibers and participates in the force transmission from myofiber to tendon, we wanted to assess whether an alteration in ECM protein distribution might lead to a disruption of the sarcolemma. For this purpose, we stained skeletal muscle cross sections with IgG (Fig. 17a), IgM (data not shown) or Albumin (data not shown). No intracellular IgG deposits were visible neither in WT nor in KO sections (Fig. 17a)

suggesting that the sarcolemma was not severely damaged. Similar results were obtained for either IgM or Albumin.

We stained longitudinal skeletal muscle sections for the Z-disc protein α-Actinin (Fig. 17b). The α-Actinin signal was altered in aged KO mice, while there was no difference in young mice (Fig. 17b) pointing to an alteration of the contractile apparatus at later ages. Mass spectrometry analysis of skeletal muscle lysates showed decreased abundance of proteins involved in muscle contraction (e.g. Tropomodulin) and muscle organization (e.g. Actin) as well as Z-disc proteins (e.g. CABZB) while some proteins involved in sugar transport and regulation of sugar transport were increased (e.g. RSC1A1) (Fig. 17c).
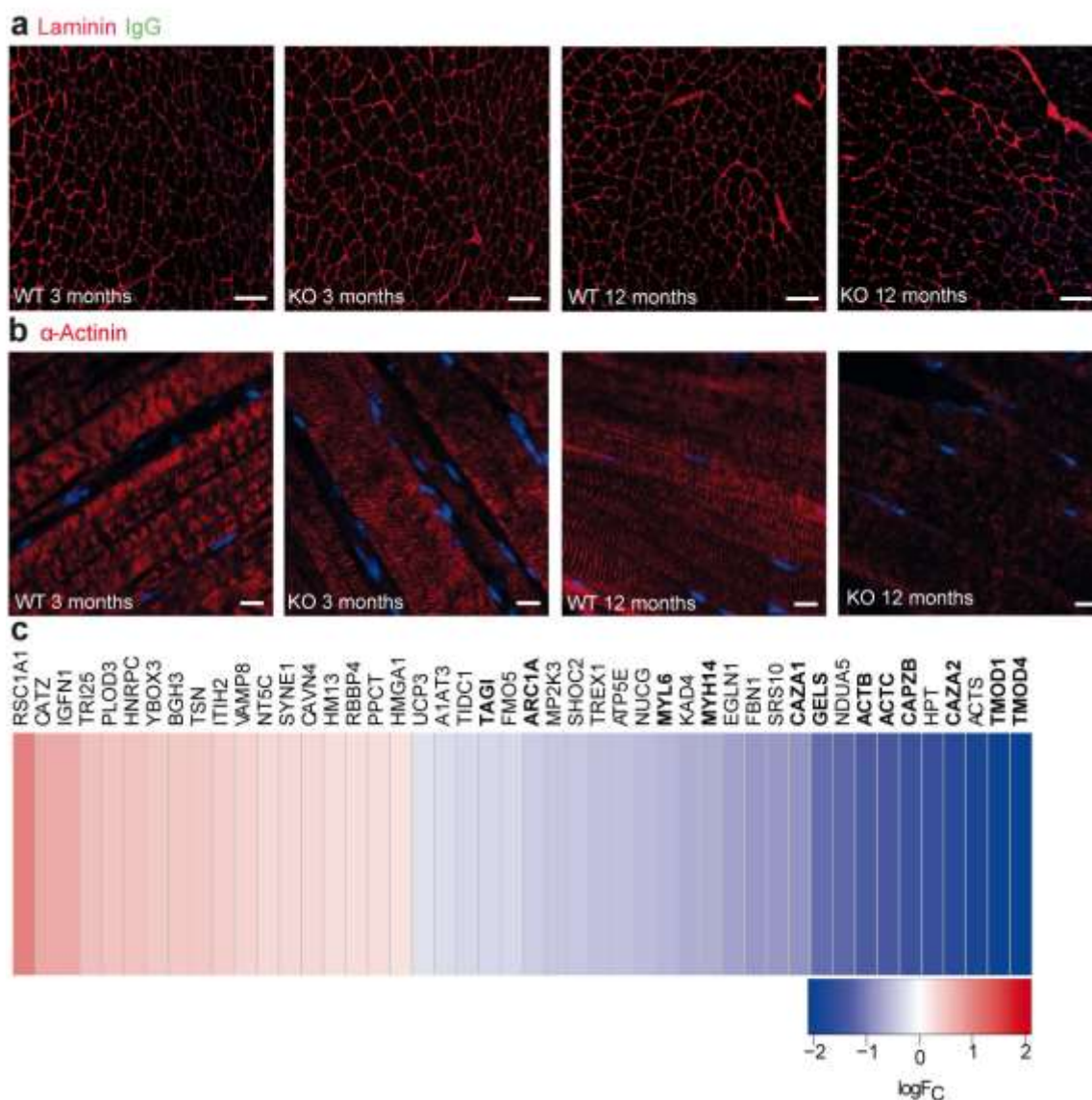
Figure 17: Alterations in skeletal muscle proteins in *Gmppa* KO mice. a) IgG stainings do not show alterations between young and older WT and KO mice (n = 3, scale bars: 100 μm). **b)** α-Actinin stainings of longitudinal skeletal muscle sections of young and old WT and KO mice reveal no differences at 3 months of age, but Z-disc alterations at 12 months of age in KO mice (n = 3, scale bars: 10 μm). **c)** Mass spectrometry analysis: most proteins necessary for muscle organization and contraction are down-regulated (blue colour,

marked in bold letters), signal proteins and peptidoglycan-binding elements are up-regulated (red colour) (n = 5). Mass spectrometry was performed by Svenja Schüler.

To exclude a neurogenic origin of the motor phenotype, we assessed the anatomy of the skeletal muscle and sciatic nerve. We did not detect grouped degenerating muscle fibers (Fig. 17a). Further supporting the notion that the nerve itself is intact, semi-thin sections of the sciatic nerves of 12-months-old WT and KO mice did not show any obvious pathology (data not shown). In agreement, we did not observe differences between aged WT and KO sciatic nerve sections (Fig. 18a) by electron microscopy analysis.

To exclude a major problem in neuromuscular transmission, we performed nerve conduction velocity experiments on aged mice. In agreement with our previous findings, no differences were detected in sensory sum action potentials (SSAPs) and compound muscle action potentials (CMAPs) (Fig. 18b, c).
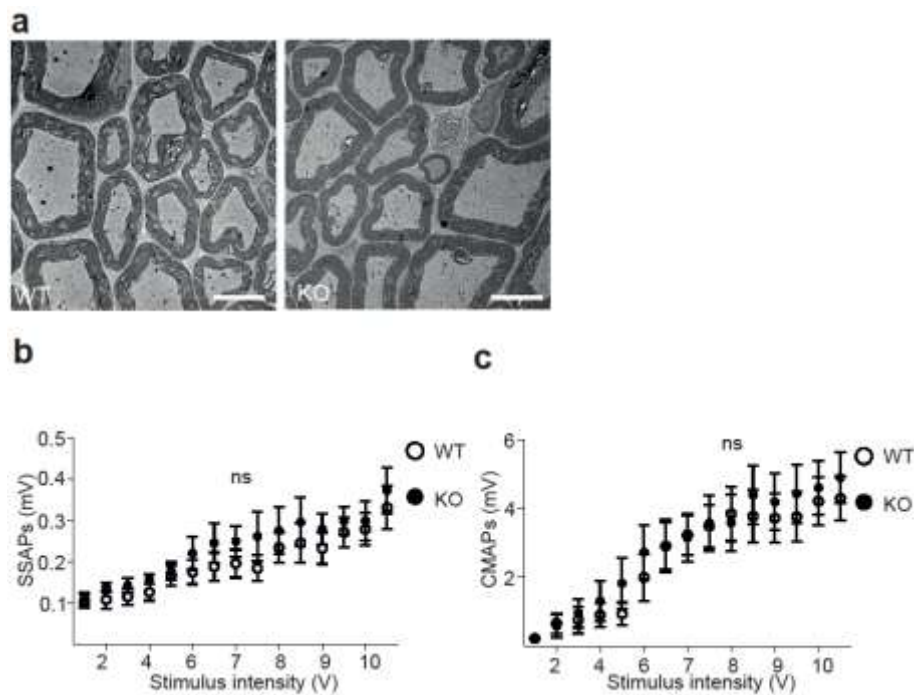
Figure 18: The myopathy in *Gmppa* KO mice is a muscle intrinsic event. a) Electron microscopy of the sciatic nerve from 12-months-old mice does not show obvious differences between the genotypes (n = 3, scale bar: 5 μm). Electron microscopy was performed by Katrin Buder. **b - c)** Amplitudes of **b)** sensory sum action potentials (SSAPs) and of **c)** distal compound muscle action potentials (CMAPs) upon electrical stimulation at the tail root do not differ between genotypes (n = 10). Recordings were performed by Lutz Liebmann.

Loss of GMPPA affects skeletal muscle glycosylation

As GDP-mannose levels were elevated in lymphoblastoid cells from AAMR patients (Koehler et al. 2013), we measured GDP-mannose and serum mannose levels (Sharma et al. 2014).

Notably, we detected diminished serum glucose levels in KO mice, while serum mannose levels were increased (Fig. 19a). In agreement, GDP-mannose levels were increased in several tissues (Fig. 19b), while GDP-fucose, GDP-glucose and GDP-glucosamine levels were unchanged (data not shown).
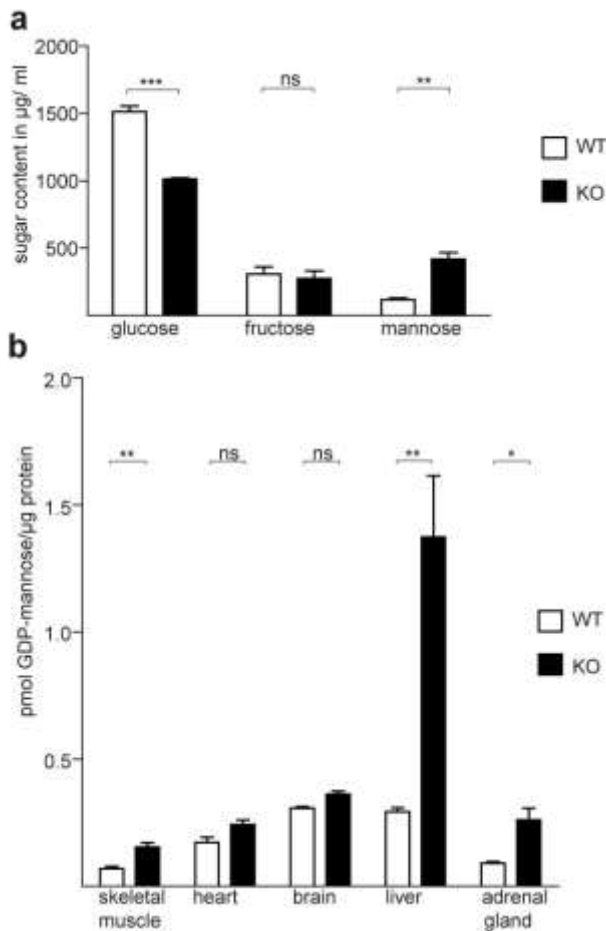

Figure 19: Mannose and GDP-mannose levels are increased in *Gmppa* KO mice. a) Measurement of sugar concentrations in serum from 3-months-old mice revealed lowered glucose and increased mannose serum levels in KO mice (n = 3). **b)** GDP-mannose levels are increased in 8-months-old KO mice (n = 3).

As increased GDP-mannose levels might alter the glycosylation pattern of proteins, we performed immunoblot analysis for several skeletal muscle proteins (Fig. 20a - d). Indeed, Oligomannose and Paucimannose immunoreactivities were increased in young (Fig. 20a, b) and aged (Fig. 20c, d) KO mice. While the signals for the lectin Peanut agglutinin (PNA), which detects non-sialylated Gal-β(1-3)-GalNAc in glycoproteins, were increased (Fig. 20a - d), we did not identify signal differences for the lectin Concanavalin A (Con A), which detects both α-D-mannosyl and α-D-glucosyl residues (Fig. 20a - d).

Because α-DG is an important protein for muscle stability and integrity and is hypoglycosylated in patients with mutations in the *GMPPB* gene (Carss et al. 2013), we assessed its glycosylation in young and aged *Gmppa* KO mice (Fig. 20a - d). With an

antibody directed against the glycosylation specific epitope IIH6C4 of α-DG we observed increased signal intensities and a band shift towards a slightly higher molecular size in KO skeletal muscle lysates (Fig. 20a - d) pointing to a hyperglycosylation of α-DG upon disruption of *Gmppa*.
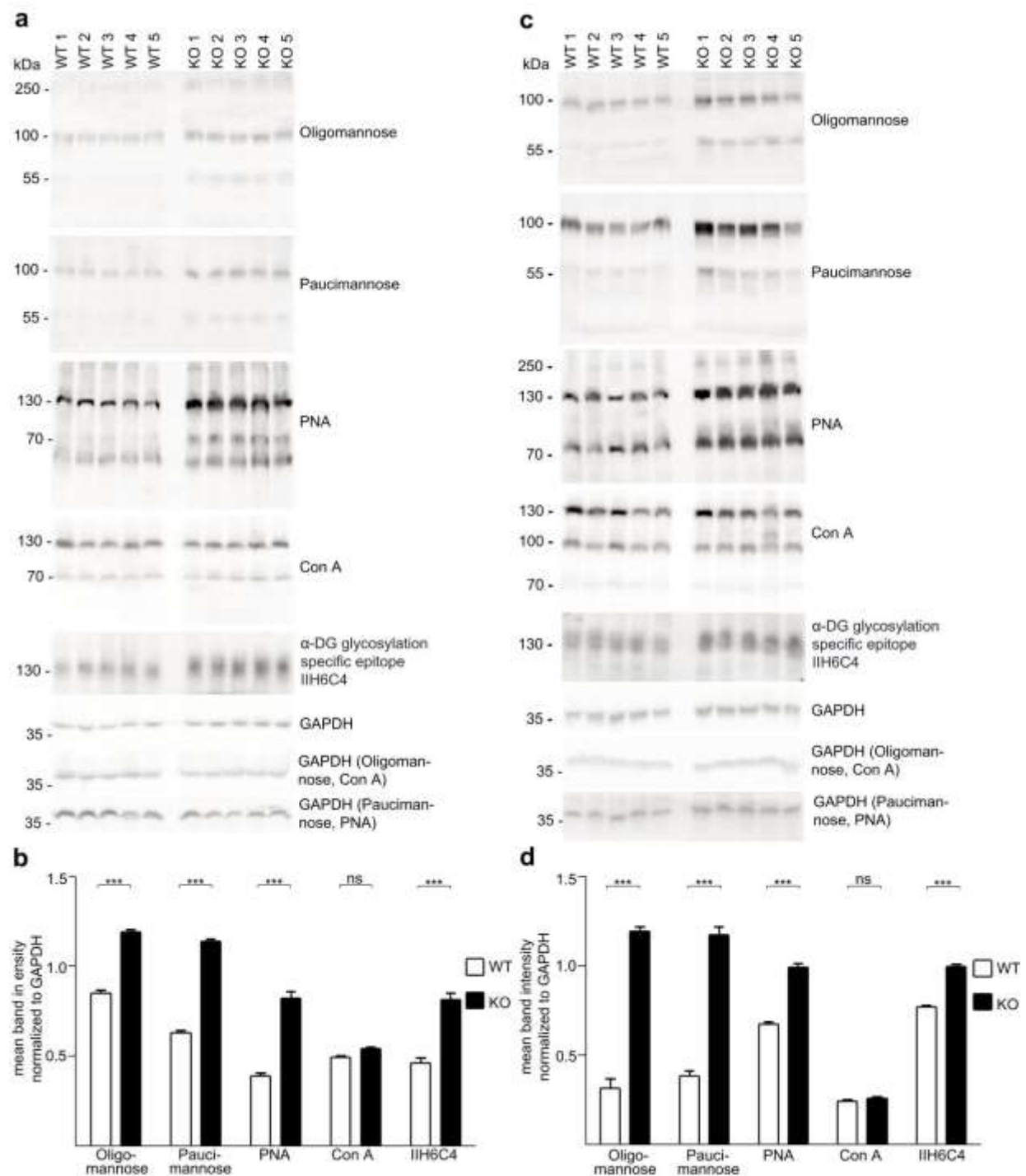

Figure 20: Loss of GMPPA leads to hyperglycosylation of skeletal muscle proteins. a - d) Immunoblot analysis of skeletal muscle lysates obtained from 3- and 12-months-old WT and *Gmppa* KO mice. In KO skeletal muscle lysates the signal intensities for Oligomannose, Paucimannose, PNA and the glycosylation specific α-DG epitope are increased. Con A expression is not changed. GAPDH served as loading control. For

immunoblot analysis of the sugar-binding components, all visible bands on the membranes were evaluated (n = 5).

In agreement, immunostainings of skeletal muscle cross sections from *Gmppa* KO mice showed increased signal intensities for Oligomannose (Fig. 21a), PNA (Fig. 21b) and the glycosylation specific epitope of α-DG (Fig. 21d), while signal intensities did not differ for Con A (Fig. 21c).
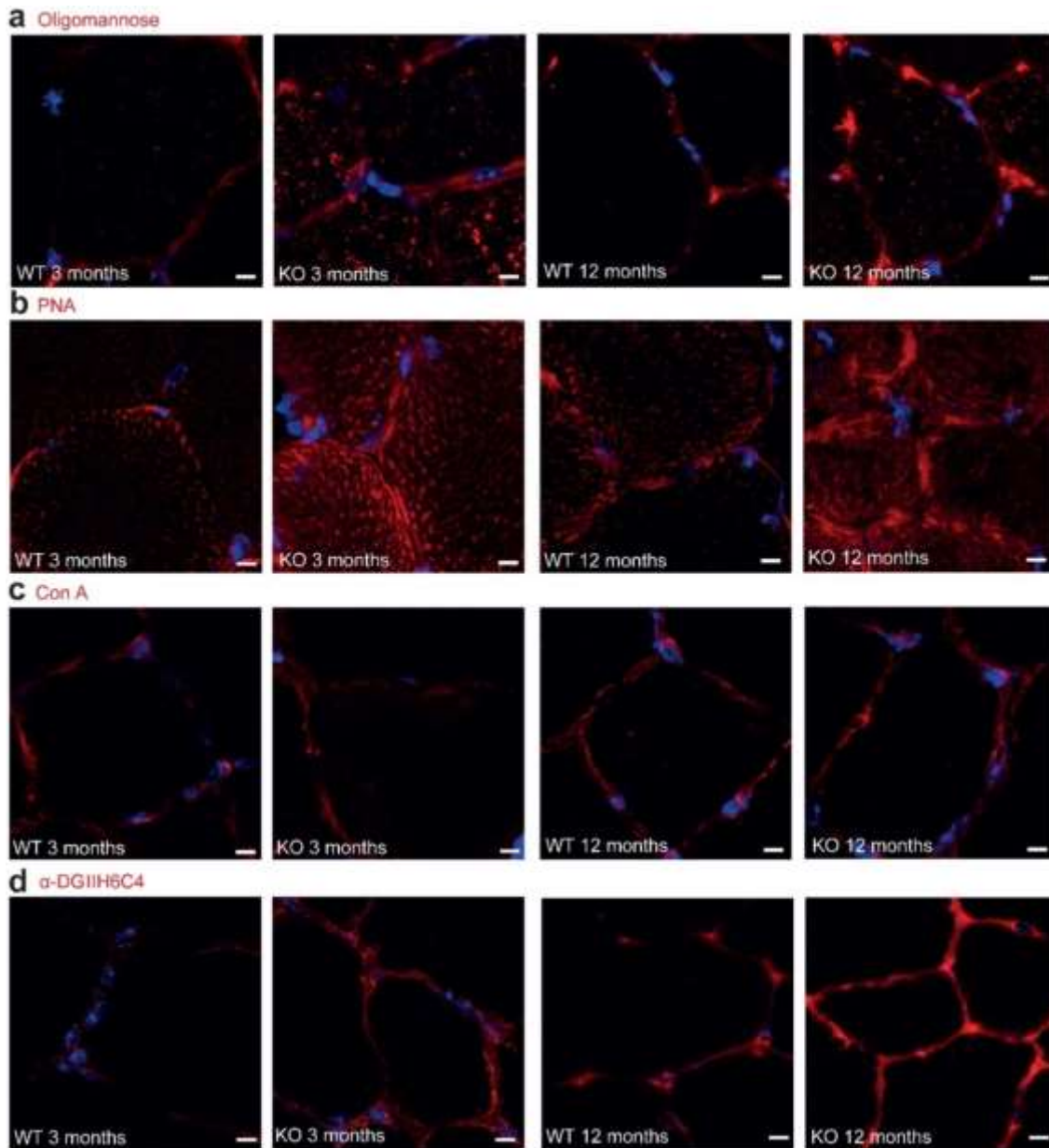

Figure 21: GMPPA loss leads to a hyperglycosylation disorder in skeletal muscle tissue. Immunohistochemistry staining of 3- and 12-months-old WT and KO cross-sections of the *Musculus Tibialis anterior*. **a)** Oligomannose and **b)** PNA stainings are increased in KO sections. **c)** Con A signals are not changed. **d)** The glycosylation specific α-DG epitope IIH6C4 is increased in KO sections. (n = 3, scale bars: 5 µm).

In order to further verify these findings for glycans, we isolated *N*- and *O*-glycans from skeletal muscle tissue for MALDI-TOF analysis.

In agreement with our previous immunoblot and IF findings, we observed elevated high-mannose *N*-glycans (Fig. 22a) and an increase in *O*-glycans carrying more than one mannose residue (Fig. 22b). In accordance with the increased PNA binding in KO lysates (Fig. 20), sialylated structures were reduced in KO tissue (Fig. 22c). In agreement with α-Dg hyperglycosylation upon disruption of *Gmppa*, we identified seven α-DG-related *O*-mannosylated glycans in the pool of glycans extracted from skeletal muscle, all of which were increased in KO samples (Fig. 22d).
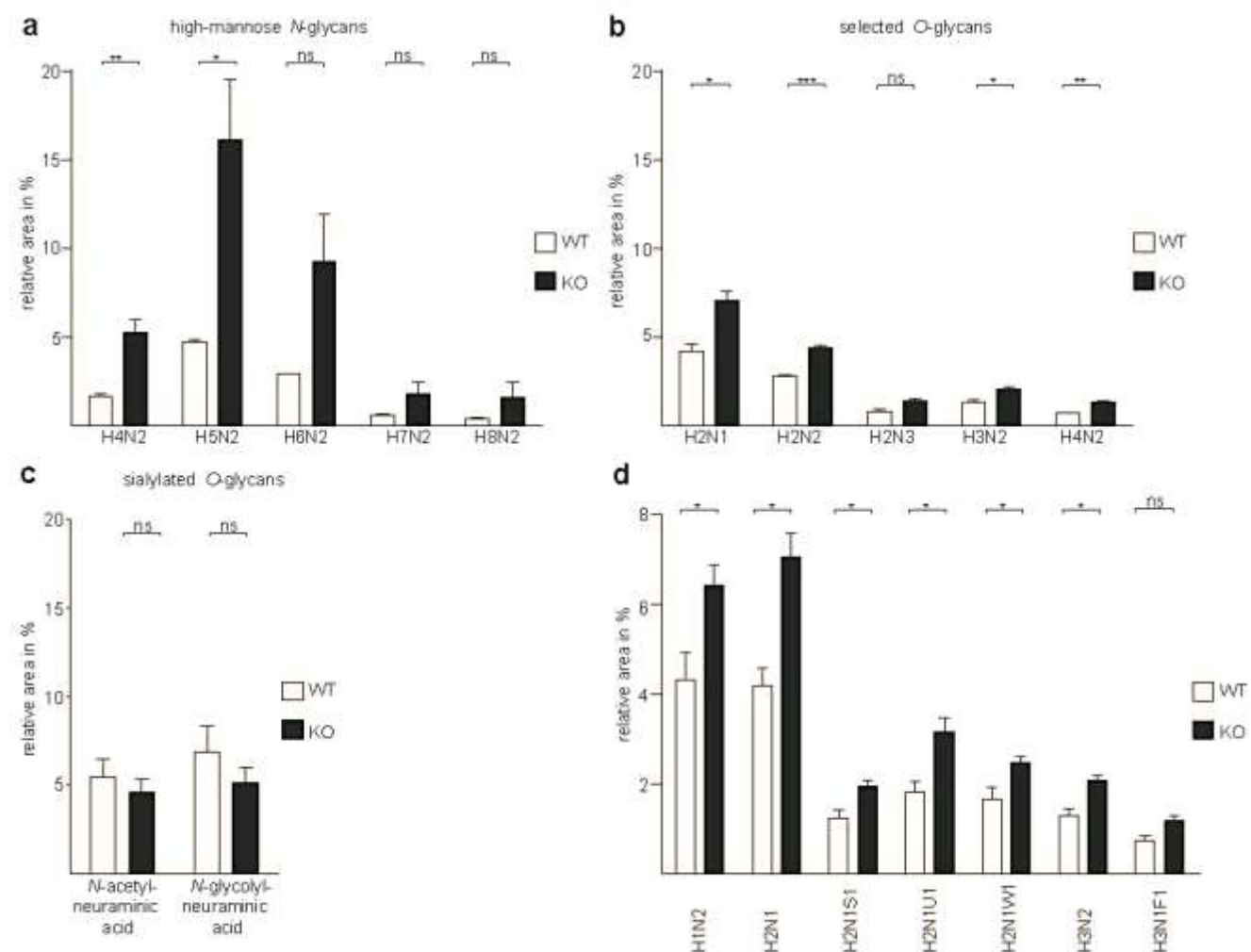
Figure 22: Loss of GMPPA leads to protein hyperglycosylation in skeletal muscle tissue in mice. Glycome analysis of the *Quadriceps* muscle from 5-months-old mice. H = hexose (mannose or galactose), N = *N*-acetylglucosamine, S = *N*-acteylneuraminic acid, U = glucoronic acid, W = glucouronic acid containing one sulphate group. **a - c)** Analysis of selected glycan peaks from MALDI-TOF spectra showing **a)** increased high-mannose *N*-glycans, **b)** increased levels in *O*-mannosylated glycans, **c)** decreased sialylated structures and **d)** increased *O*-mannosylated glycans originating from α-DG in KO tissue (n = 3). Glycome analysis was performed by Karina Biskup.

α-DG hyperglycosylation increases its binding to ECM proteins

It has been demonstrated that hypoglycosylated α-DG shows a decreased binding affinity for ECM ligands, e.g. Laminin (Esser et al. 2012, Endo 2015), and that α-DG hyperglycosylation increases its binding to ECM proteins (Brockington et al. 2010). So, we asked whether the binding of ECM proteins to α-DG is stronger in *Gmppa* KO mice. Therefore, we enriched glycoproteins with Wheat germ agglutinin (WGA) and/or Con A lectins which were then separated by SDS-PAGE. Probing the membranes with antibodies directed against either the glycosylation-specific epitope of α-DG or the α-DG core protein, confirmed an enrichment of glycoproteins and a shift of α-DG towards a higher molecular weight (Fig. 23). Incubation of the membranes with either Laminin or Agrin revealed a significantly increased binding of both proteins (Fig. 23).
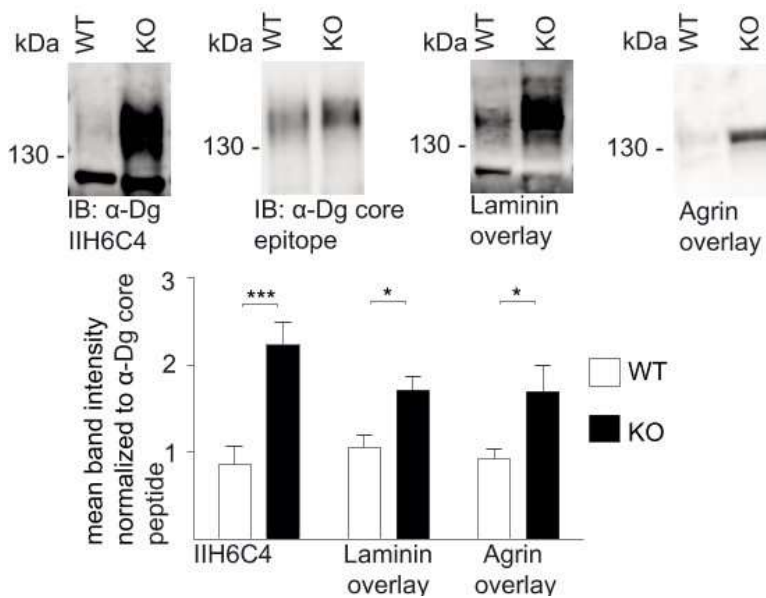

Figure 23: Loss of GMPPA increases its binding to ECM proteins. Laminin and Agrin overlay assay showing an increased binding of hyperglycosylated α-DG to Laminin and Agrin in *Gmppa* KO mice (n = 3). The α-DG core protein served as loading control.

As Agrin contributes to the formation and maintenance of neuromuscular junctions (NMJs) (Sugiyama et al. 1994), we assessed the morphology and innervation of NMJs in young and aged *Gmppa* KO mice (Fig. 24a - c). Notably, young and older KO mice show more fragmented (Fig. 24a, b) and less fully innervated NMJs (Fig. 24a, c) compared to WT littermates.
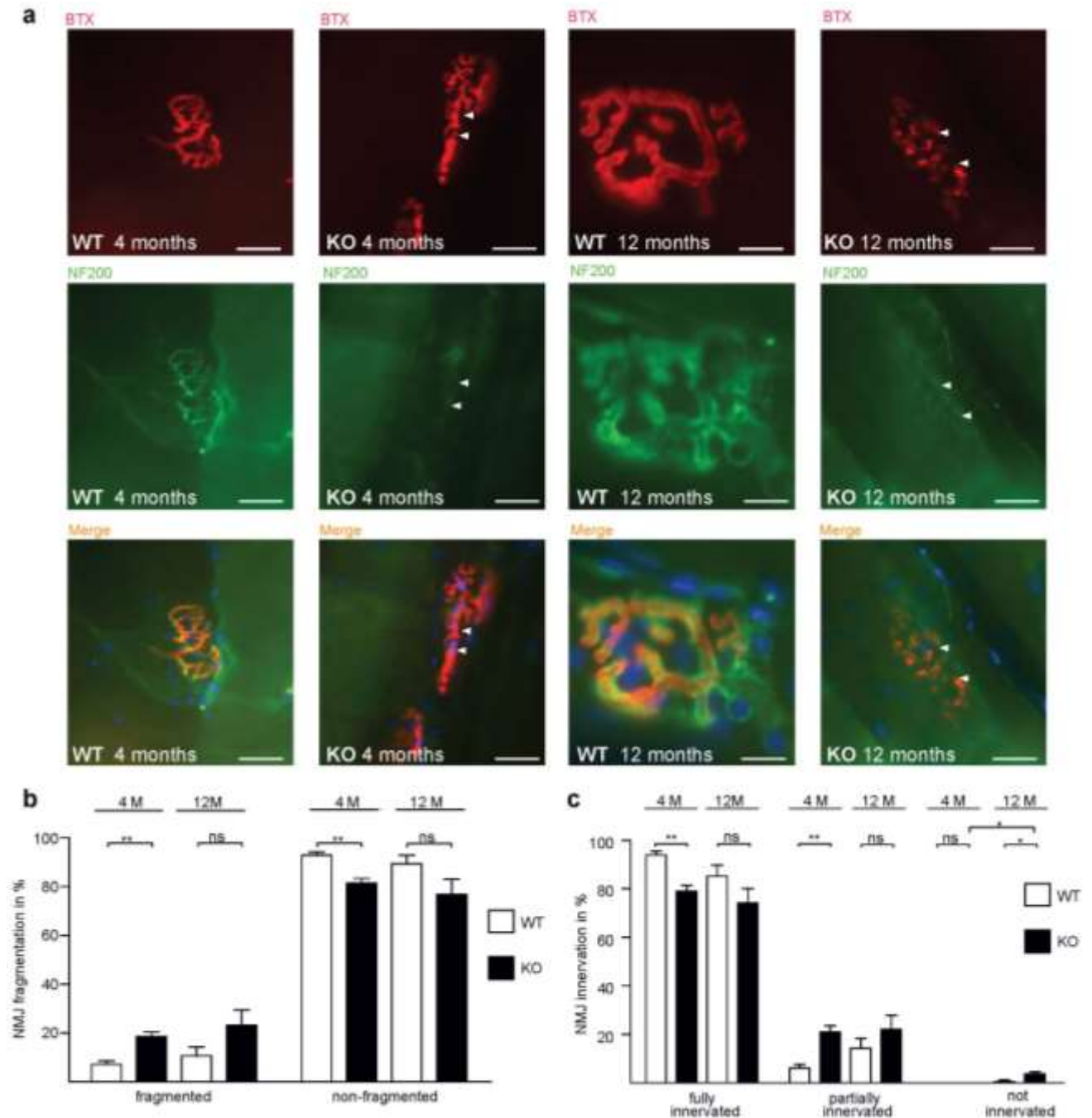
Figure 24: Loss of GMPPA affects the integrity of neuromuscular junctions. a - c) Analysis of neuromuscular junctions (NMJ) stained with α-bungarotoxin (BTX). The nerve fibers innervating NMJs are stained for NF200 (2H3, SV2). In KO mice the ratio of fragmented NMJs is increased and the innervation of NMJs decreased (n = 4, scale bars: 50 µm). NMJs were prepared and analyzed by Julia von Maltzahn.

Gmppa knockdown decreases α-DG stability

As post-translational modifications such as glycosylation may alter protein stability (Baudys et al. 1995), we asked whether the hyperglycosylation of α-DG in *Gmppa* KO mice affects its stability. We tested α-DG protein abundance in skeletal muscle lysates with an antibody directed against the inner core of α-DG. Interestingly, α-DG protein bands were slightly

shifted towards a higher molecular weight and displayed decreased signal intensities in KO mice (Fig. 25a, b, c, d) while β-DG levels were not changed (Fig. 25a, b, c, d). In agreement with this notion, IF revealed reduced signal intensities for α-DG in KO mice while β-DG levels did not differ between genotypes (Fig. 25e, f).
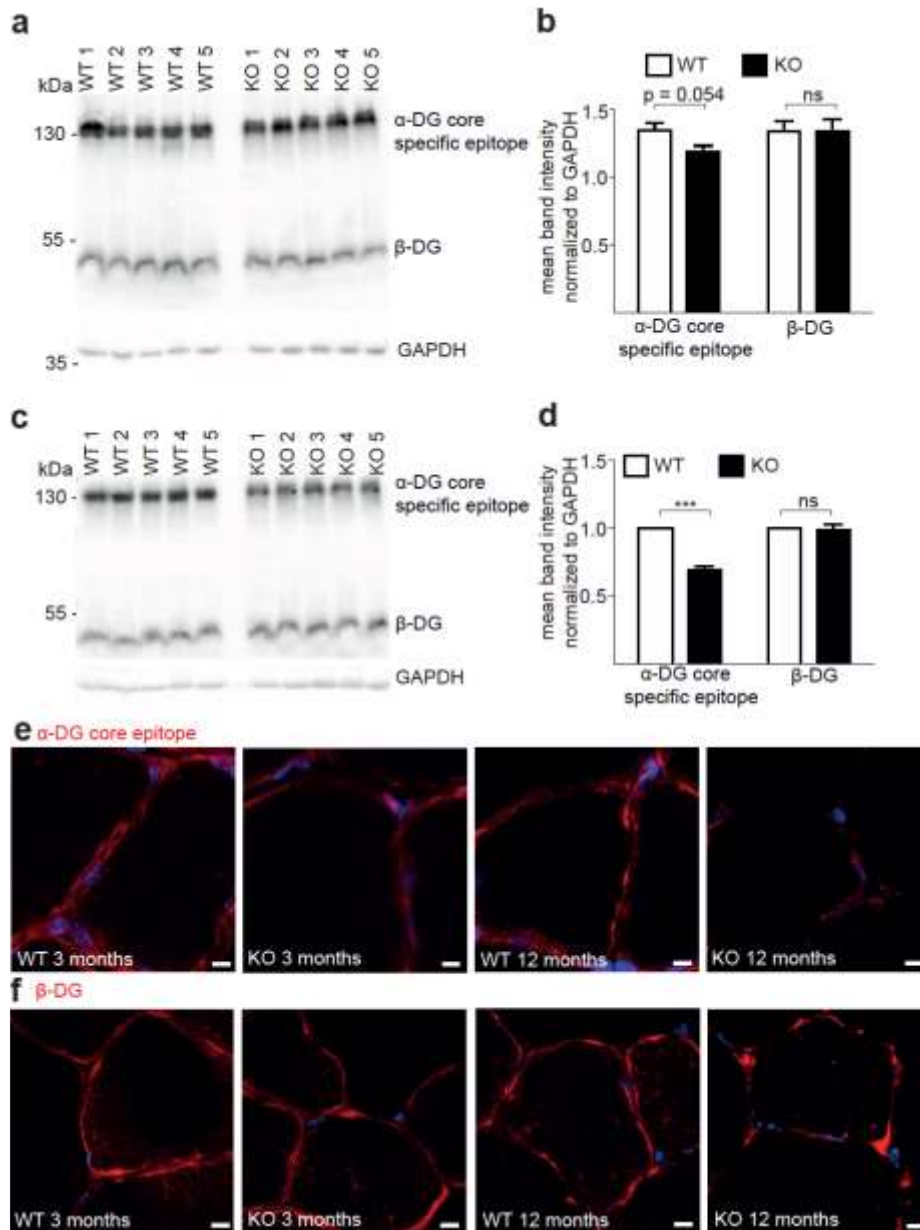

Figure 25: *Gmppa* KO mice display reduced α-DG abundance. a - b) Immunoblot analysis shows reduced core α-DG levels, while β-DG levels are not changed in 3-months- and **c - d)** 12-months-old KO mice (n = 5). GAPDH served as loading control. **e)** IF demonstrates reduced core-α-DG and **f)** unchanged β-DG signals in young and aged mice (n = 3, scale bars: 5 μm).

To address α-DG turnover, we performed *Gmppa* knockdown experiments in murine primary differentiating myoblasts. We employed two knockdown controls in this experiment: a siRNA against *Dystroglycan* (*siDag1*) as a positive control for *Dystroglycan* knockdown and scrambled siRNA (*siScr*) as a negative control. Briefly, myoblasts were seeded and treated

next day with differentiation medium. After two days in differentiation medium, cells were transfected with siRNA. After 3 days we blocked protein translation with cycloheximide (CHX) and assessed α-DG abundance 24 h afterwards by immunoblot analysis. Ubiquitin served as a control for successful translation stop, as in CHX-treated cells Ubiquitin levels were decreased (Fig. 26a, b). *Dystroglycan* and *Gmppa* knockdown was successful as evident from Western blot analysis of lysates obtained from siRNA-treated cells (Fig. 26a, b). Consistent with a shorter half-life of hyperglycosylated α-DG, α-DG levels were reduced upon knockdown of *Gmppa*, which further decreased in CHX-treated cells (Fig. 26a, b) about 47 %. In control cells (*siScr*) α-DG levels decreased about 24 % after CHX treatment.

Because glycosylation starts at the endoplasmic reticulum (ER) and only correctly post-translationally modified proteins are transported to the Golgi (Hirai et al. 2018), we asked whether BIP, a major ER chaperone and ER stress sensor (Bravo et al. 2013), might be up-regulated in *Gmppa* knockdown myoblasts. As BIP levels did not differ between the different knockdown conditions (Fig. 26c, d), a major ER stress upon loss of GMPPA is unlikely.

Because the glycosylation process continues in the Golgi, we also studied the abundance of different Golgi marker proteins. Interestingly, the *cis*Golgi protein GM130, the Golgi protein GLG1 as well as the *trans*Golgi protein TGN38 showed higher signal intensities (Fig. 26c, d) pointing to a secondary alteration of the Golgi. Moreover, ERK signaling was strongly activated (Fig. 26c, d).
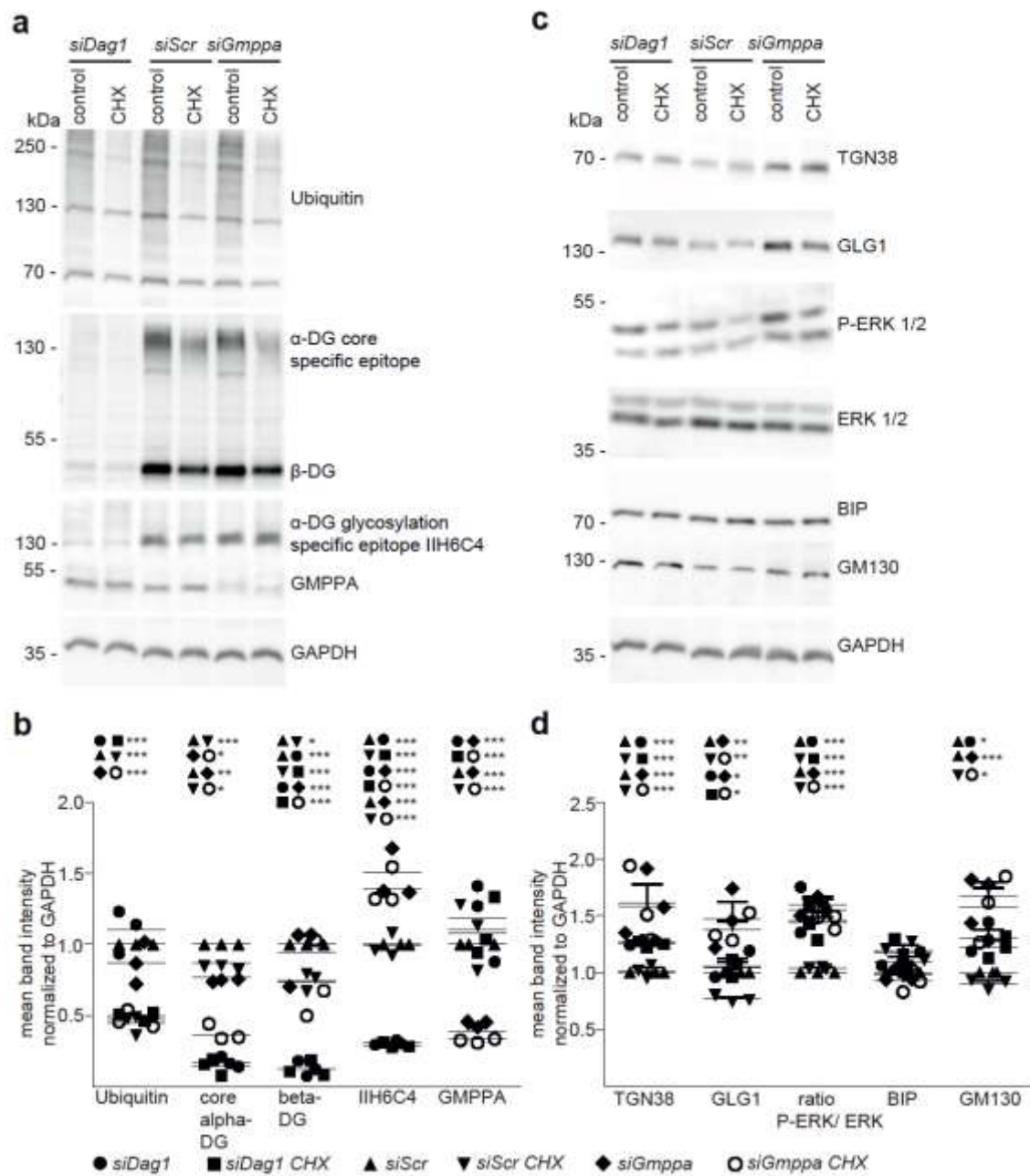
Figure 26: *Gmppa* knockdown decreases GMPPA stability. a - b) Immunoblot analysis shows efficient knockdown of *Dystroglycan* (*Dag1*) and *Gmppa*. Cycloheximide (CHX) treatment results in diminished Dystroglycan levels with core-α-DG expression being significantly lower in *Gmppa* knockdown than compared to control (*siScr*) cells. Ubiquitin served as control for efficient CHX treatment. GAPDH served as loading control (n = 3). **c - d)** Immunoblot analysis shows that *Dystroglycan* and *Gmppa* knockdown leads to an increase in TGN38, GLG1, GM130 and ERK activation whereas BIP is not changed (n = 3, not significant values are not shown).

As we observed altered abundances of Golgi proteins, we wondered whether the Golgi structure within the skeletal muscle is normal. Therefore, we stained murine skeletal muscle fibers with the *cis*Golgi marker GM130, the *trans*Golgi marker TGN38 and the Golgi marker GLG1.

Notably, the Golgi, especially the TGN appeared more fragmented in skeletal muscle fibers of KO mice as evidenced by an increased number of GLG1- and TGN38-positive structures (Fig. 27a - d) and a reduced overlap between different Golgi-markers (Fig. 27a - e). Moreover, we observed a higher integrated signal density for TGN38 in KO fibers (Fig. 27 a - e).

Taken together, disruption of *Gmppa* does not cause ER stress but results in structural alterations of the Golgi apparatus.
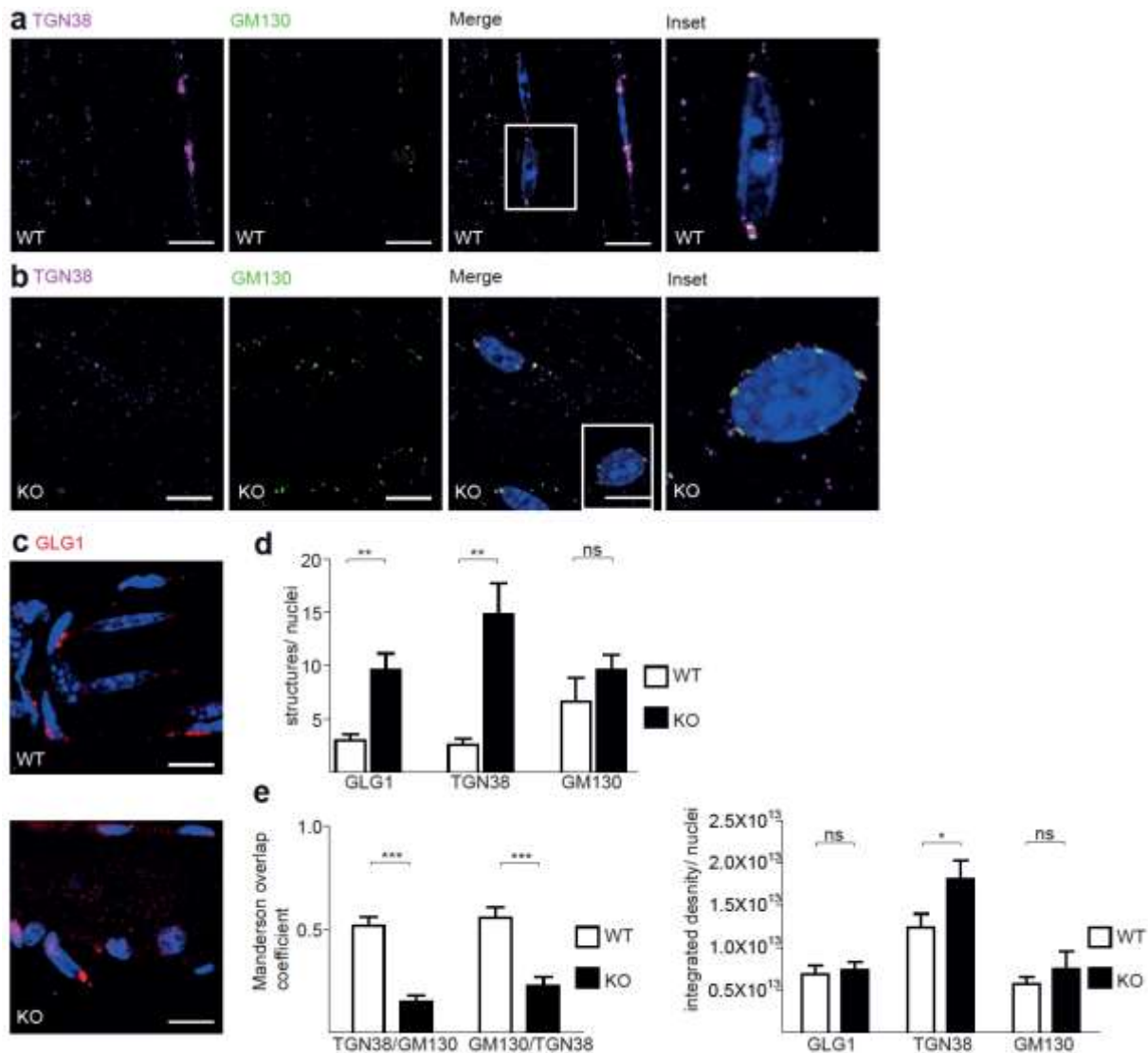

Figure 27: Loss of GMPPA affects Golgi-associated proteins. (a,b) Representative images of skeletal muscle fibers from 5-months-old mice stained for TGN38 and GM130. **a)** WT fibers show a Golgi staining with partial overlap of TGN38 with GM130 (scale bars: 10 µm). **b)** KO fibers do not show an obvious overlap of the *cis*Golgi protein GM130 with the *trans*Golgi protein TGN38 (scale bars: 10 µm). **c)** Representative images of skeletal muscle fibers from 5-months-old mice stained for GLG1 (scale bars: 10 µm). **d)** GLG1 and TGN38 staining reveal more *trans*Golgi fragments in KO fibers, whereas *cis*Golgi GM130 fragments are not changed between genotypes (n = 3 per genotype). **e)** Manderson overlap coefficient reveals a partial overlap of GM130 with TGN38 in WT fibers. In KO fibers this overlap coefficient is significantly reduced (n = 3). The integrated density is increased for TGN38 stainings in KO fibers, while it is not changed for GLG1 and GM130 (n = 3).

α-DG is hyperglycosylated in AAMR patients

Our findings in *Gmppa* KO mice prompted us to ask whether patients with mutations in the *GMPPA* gene might show similar alterations in skeletal muscle.

From two previously described patients with *GMPPA* mutations (Benítez et al. 2018) we were able to obtain skeletal muscle biopsies. Control samples were obtained from the Telethon Biobank. Consistent with our findings in *Gmppa* KO mice, both patients displayed increased glycosylation of α-DG (Fig. 28a, b), while the core protein of α-DG was diminished (Fig. 28c). As in *Gmppa* KO mice, β-DG abundance was not altered between patient and control samples (Fig. 28d). Further, we observed discontinuous Laminin signals in both patients (Fig. 28e) similar to our findings in *Gmppa* KO mice. Moreover, α-Actinin signals were altered in patients compared to control samples suggesting Z-disc alterations (Fig. 28f). Electron microscopy analysis revealed disarrayed filaments and loss of the continuity of the Z-discs (Fig. 28g).
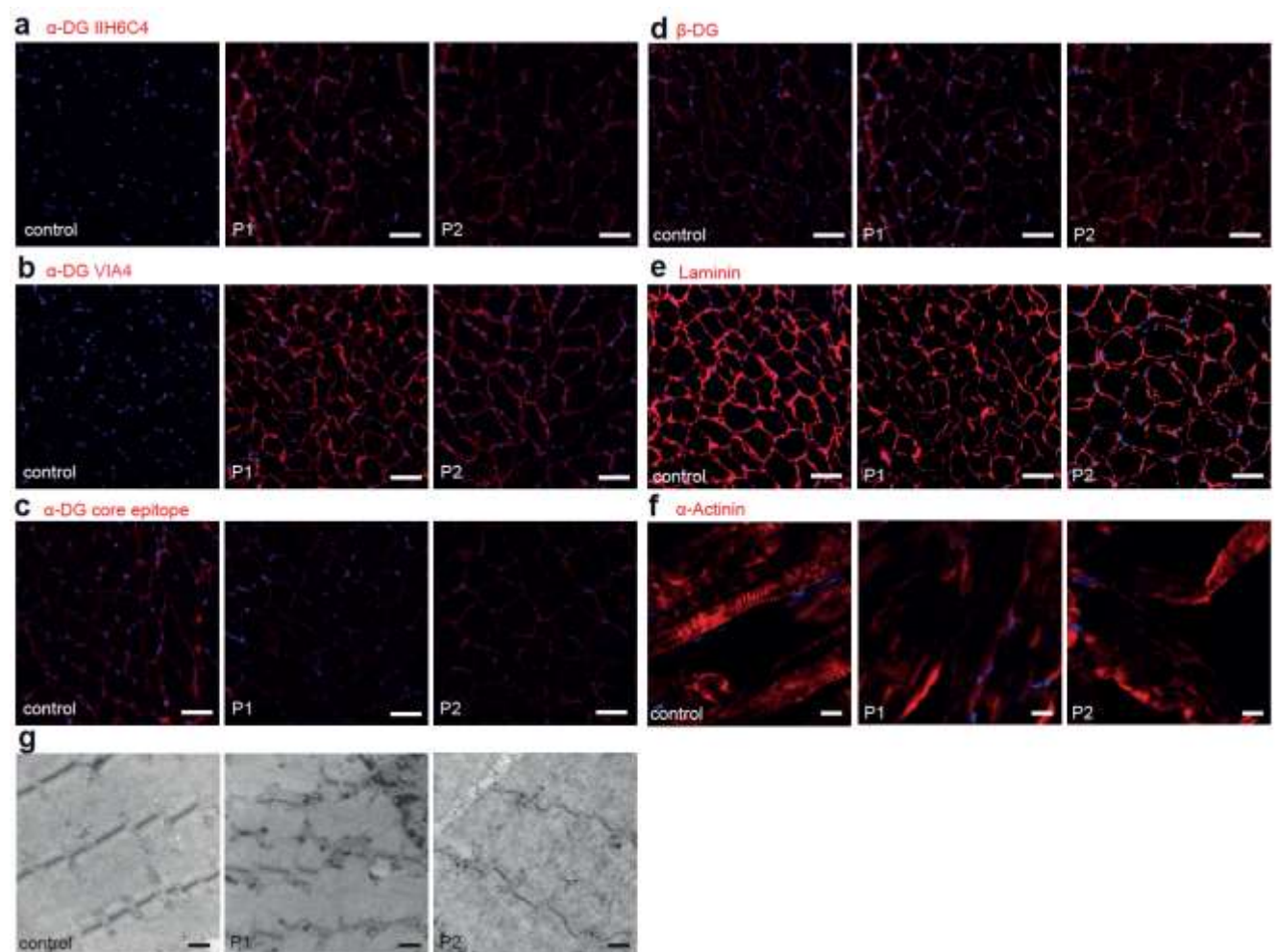

Figure 28. AAMR patients show hyperglycosylation and Z-disc alterations. a - e) Immunostaining of *Quadriceps* cross-sections (scale bars: 50 μm) showing an increase in the glyosylation specific α-DG epitopes **a)** IIH6C4 and **b)** VIA4. **c)** Core α-DG levels are reduced whereas **d)** β-DG levels are not changed. **e)** Laminin levels are unchanged but reveal an interrupted staining pattern in both patients compared to the control. **f)** α-Actinin staining is altered in patient longitudinal skeletal muscle sections (scale bars: 10 μm). **g)** Electron

microscopy analysis reveals disarrayed fibers and loss of the continuity of the Z-lines in both siblings (scale bar: 500 nm). Electron microscopy was performed by Braulio Martínez.

Immunoblot analysis of skeletal muscle lysates revealed diminished GMPPA levels in both patients (Fig. 29). In agreement with our data from *Gmppa* KO mice, band intensities for Oligomannose, Paucimannose, and PNA were increased in patient samples, while Con A signals were unchanged (Fig. 29). With antibodies directed against the glycosylation specific epitopes IIH6C4 and VIA4 of α-DG we observed a band shift towards a higher molecular weight and increased signal intensities in patient samples (Fig. 29) pointing towards a hyperglycosylation of α-DG. With an antibody against the core protein of α-DG we observed a band shift to a slightly higher molecular weight and decreased band intensity for both patients (Fig. 29). In accordance to our myoblast knockdown findings, the *trans*Golgi protein TGN38 was upregulated in patient samples (Fig. 29).
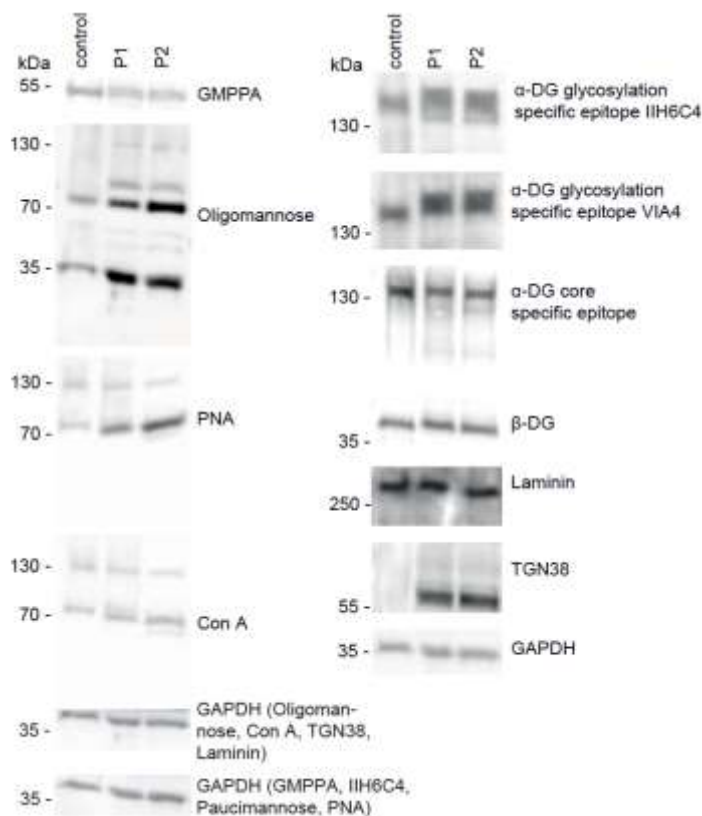

Figure 29: Protein hyperglycosylation in skeletal muscle of AAMR patients. Immunoblot stainings showing reduced signal intensities for GMPPA in both sisters as well as increased signal intensities for Oligomannose, PNA and the glycosylation specific α-DG epitopes, while Con A staining is unchanged. Core α-DG levels are decreased, while β-DG and Laminin levels are not changed. The *trans*-Golgi protein TGN38 is increased. GAPDH served as loading control.

A mannose-depleted diet rescues the motor phenotype in *Gmppa* KO mice

As *Gmppa* KO mice display elevated mannose and GDP-mannose levels, we asked whether a mannose-free diet might prevent the progress of the disease. Therefore, *Gmppa* WT and KO mice were fed either with mannose-depleted food with reduced glucose and fructose content (treated) or with normal food (untreated) starting from postnatal day 14 (P14) up to 8 months of age. Notably, the FBA did not deteriorate in the *Beam Walk balance test* in treated KO mice compared to untreated KO mice (Fig. 30a, b). In the *Kondziela´s inverted screen test*, the latency until the mice fell off the wire mesh was almost normalized in treated KO mice (Fig. 30c). Comparison of skeletal muscle proteins of mannose-restricted or unrestricted KO mice with those of unrestricted WT mice by mass spectrometry showed that levels of many proteins either up- or down-regulated in untreated KO mice were largely normalized by dietary intervention (Fig. 30d).
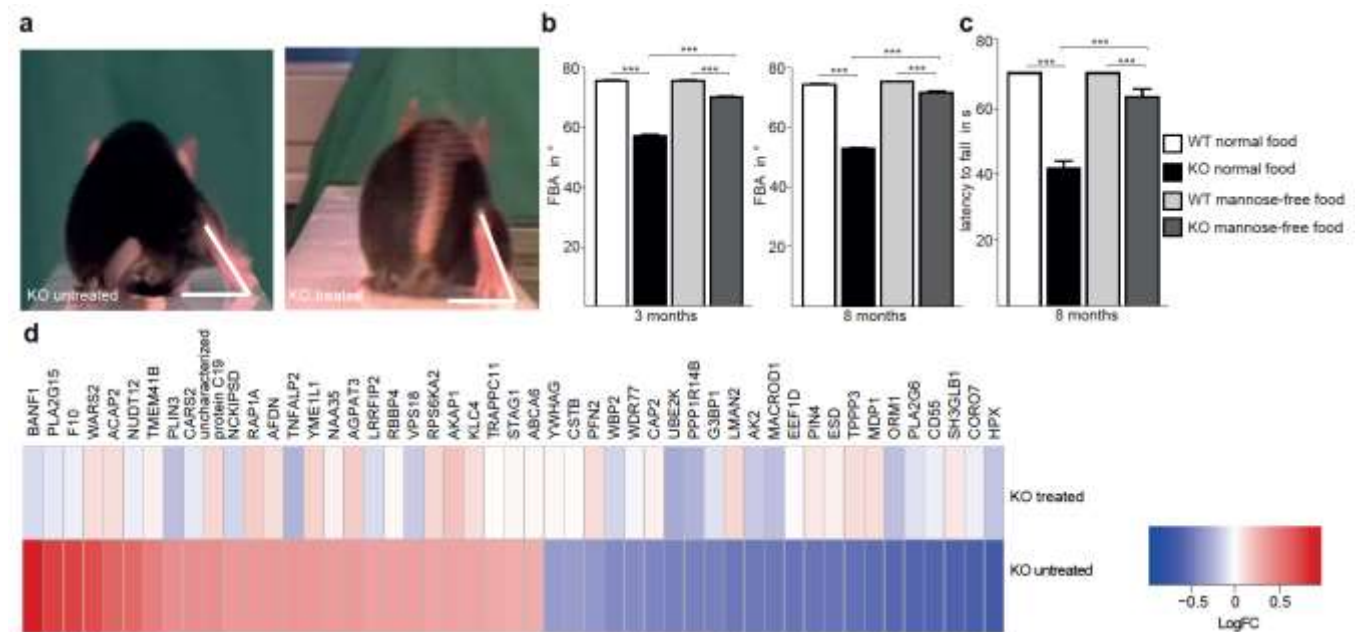

Figure 30: A mannose-depleted diet largely rescues the myopathy in *Gmppa* KO mice. a - b) *Beam Walk balance test*. **a)** Representative video frames from an untreated KO and a treated KO mouse (8 months of age) walking on a beam at the moment when the toe is taken off. The foot base angle (FBA) is indicated in white lines. **b)** In treated mice, the difference in the FBA between WT and KO mice is decreased compared to untreated animals and does not increase with age (n = 11). **c)** *Kondziela´s inverted screen test*. In treated mice, the difference in the latency to fall between WT and KO mice is decreased compared to untreated animals (n = 11). **d)** Mass spectrometry analysis showing proteins which are altered in the untreated KO but normalized in the treated KO animals compared to the WT littermates (n = 5, up-regulated proteins are indicated in red, down-regulated proteins are shown in blue). Mass spectrometry was performed by Svenja Schüler.

Our immunoblot analysis revealed almost normalized signal intensities for Oligomannose, Paucimannose and PNA in skeletal muscle lysates dissected from KO mice treated with mannose-depleted food (Fig. 31a, b). Moreover, the respective bands for the glycosylation

specific epitope of α-DG were slightly shifted towards lower molecular weight and the signal intensity in treated KO mice was decreased compared to untreated KO mice. The abundance of the core α-DG was almost normalized (Fig. 31a, b).

Moreover, we performed immunoblot analysis for the ER stress marker protein BIP and selected Golgi proteins. In accordance to our previous findings in myoblasts, BIP levels did not differ between genotypes and treatments (Fig. 31c, d). However, the *trans*Golgi protein TGN38 and the Golgi protein GLG1, which were up-regulated in untreated KO mice, were normalized upon treatment (Fig. 31c, d). In contrast to our findings in myoblast knockdown experiments, the *cis*Golgi protein GM130 was not altered in *Gmppa* KO mice (Fig. 31c, d).
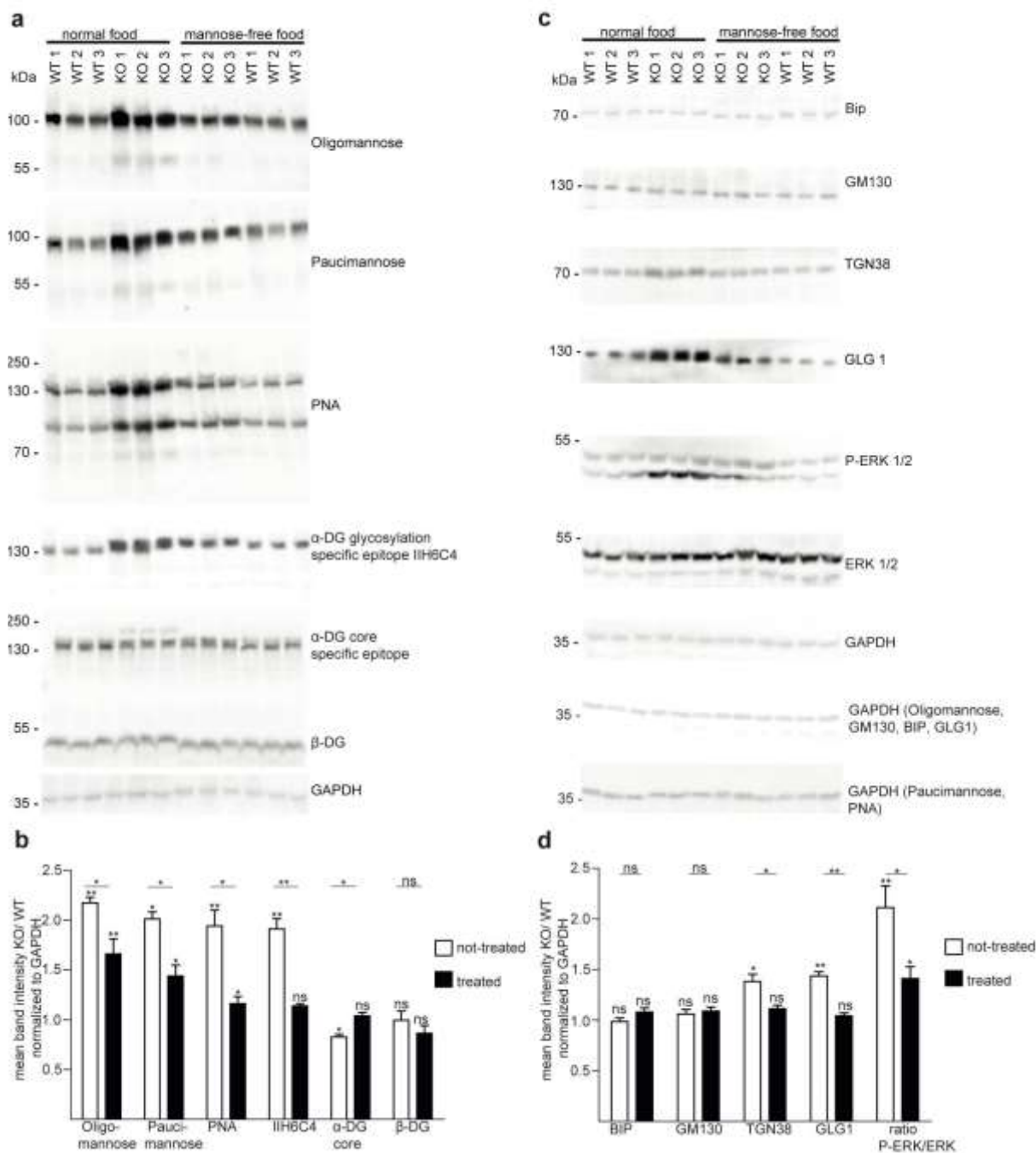

Figure 31: A mannose-depleted diet rescues the protein hyperglycosylation in *Gmppa* KO mice. a - b) Immunoblot analysis shows increased signals for Oligomannose, Paucimannose, PNA and the glycosylation-

specific α-DG epitope IIH6C4 in untreated KO mice, which are normalized by the mannose-depleted diet. α-DG core-protein levels are decreased in untreated KO mice and rescued by the mannose-depleted diet. β-DG levels are unchanged. For immunoblot analysis of the lectin as well as Oligomannose and Paucimannose stainings, all bands were quantified (n = 3). **c - d)** Immunoblot analysis reveals unchanged protein levels for BIP and GM130. TGN38, GLG1, and P-ERK levels are increased in untreated KO mice and decrease with therapy. GAPDH served as loading control (n = 3).

Discussion

Glycosylation is the most frequent post-translational modification. Perturbations of glycosylation can lead to severe diseases also known as congenital disorders of glycosylation (CDGs) which can affect a wide variety of organs and body functions.

Up to date roughly 400 genes are known to be involved in the glycosylation pathway, but only 130 genes are currently associated with glycosylation disorders. So, glycosylation disorders are rare diseases and are generally characterized by hypoglycosylation. A well-studied and more common glycosylation defect is caused by mutations in the gene encoding Phosphomannomutase 2 (PMM2). It occurs with a prevalence of 1/20,000 and is therefore the most prevalent glycosylation disorder (Freeze et al. 2014). PMM2 converts mannose-6-phosphate into mannose-1-phosphate, which is the substrate for GMPPB. Mutations in the *PMM2* gene lead to a decreased PMM2 activity and thus result in lower mannose-1-phosphate levels and hypoglycosylation. Affected individuals show gait ataxia, developmental delay, hypotonia and strabismus among other symptoms (Péanne et al. 2017, Jaeken 2013).

Recently, it has been reported that mutations in the *GMPPB* gene also cause a glycosylation disorder (Carss et al. 2013). GMPPB converts Mannose-1-phosphate and GTP into GDP-mannose, the initial molecule for *N*-linked glycosylation and *O*-linked mannosylation (Freeze et al. 2012) which is of special relevance for α-DG. In agreement, it has been shown that GMPPB mutations result in the hypoglycosylation of α-DG.

Our group identified mutations in the *GMPPA* gene in a syndromic disorder which is characterized by gait abnormalities, achalasia, alacrima, and mental retardation (AAMR-syndrome) (Koehler et al. 2013, Barišić et al. 2011, Engel et al. 2015). Up to now, the function of GMPPA remained unclear, because it lacks enzymatic activity compared with GMPPB (Jin et al. 2005). This thesis aimed to elucidate the underlying mechanisms and to envisage potential therapeutic strategies.

Localization and interaction of GMPPA and GMPPB

GMPPA lacks enzymatic activity due to an insertion of 2 amino acids within its catalytic pocket, but is still able to bind GDP-mannose, the product of GMPPB. Therefore, GMPPA may rather serve as an allosteric feedback inhibitor of GMPPB (Koehler et al. 2013, Szumilo et al. 1993, Jin et al. 2005).

In overexpression Co-IP studies in HEK-293T cells we could show that human GMPPA and GMPPB interact. By GST pull-down assays with recombinant proteins we further resolved that this interaction is direct. While some disease-associated mutations in GMPPA impair this interaction, other mutations do not. For instance, we could show that the disease associated GMPPA variant with the amino acid substitution T334P, which locates to the C-terminal part

of the protein, does not interact with GMPPB, whereas a variant with the amino acid substitution G182D, which locates to the N-terminal part of GMPPA, still interacts with GMPPB. Interestingly, mutations in the C-terminal part of GMPPB such as the amino acid exchange D334N do not affect the interaction between both proteins.

These data imply that the C-terminal part of GMPPA and the N-terminal part of GMPPB are necessary for the interaction between both proteins. Therefore, we generated GMPPA and GMPPB domain mutants. Notably, a GMPPA mutant missing the N-terminal part of the protein still interacted with GMPPB, while the GMPPA variant lacking the C-terminal part did not interact with GMPPB. In contrast, a GMPPB variant missing the N-terminal part of the protein did not interact with GMPPA, whereas a GMPPB variant lacking the C-terminal part interacted with GMPPA.

Immunofluorescence stainings for heterologous expressed GMPPA WT and mutant variants as well as GMPPB WT and mutant proteins corroborated our Co-IP findings. Moreover, we saw an altered staining pattern upon transfection of COS-7 cells with GMPPA and GMPPB point mutant constructs. The domain mutant missing the N-terminal part of GMPPA and the mutant missing the C-terminal part of GMPPB showed the same diffuse cytoplasmic staining as already observed for the WT constructs. The domain mutant lacking the C-terminal part of GMPPA as well as the mutant missing the N-terminal part of GMPPB, however, showed an irregular staining pattern and no co-localization with the corresponding WT construct.

Taken together, these findings suggest that the C-terminal part of GMPPA and the N-terminal part of GMPPB mediate interaction of the two proteins. Moreover, GST pull-down suggest a direct interaction of GMPPA with GMPPB.

Because we observed just a faint band when pulling down GMPPA-MBP with immobilized GMPPB-GST and a very intense band when pulling down GMPPA-MBP with immobilized GMPPA-GST, we suggest that GMPPA is preferentially forming homodimers in a solution without additional GDP-mannose. Moreover we suggest that we would see an increased interaction of GMPPA with GMPPB in the presence of elevated GDP-mannose levels.

To confirm the interaction of GMPPA with GMPPB for the endogenous proteins *in vivo*, we performed a proximity-ligation-assay on murine tissue sections. The PLA assay clearly showed interaction between GMPPA and GMPPB. The specificity of the PLA assay was verified on *Gmppa* KO sections.

Although these data suggest that GMPPA acts as an allosteric feedback inhibitor of GMPPB, they do not prove this hypothesis. To this end, one could address whether GMPPB activity changes with increasing or decreasing GDP-mannose levels, when the GMPPA WT protein is present. Whether GMPPB activity changes with GMPPA mutant proteins remains elusive. To address these questions, GMPPB enzyme activity assays with increasing or decreasing

GDP-mannose levels in the presence of GMPPA WT or mutant proteins should be performed.

Symptoms of *Gmppa* KO mice and human patients

Disruption of the *Gmppa* gene in mice partially recapitulated muscle weakness and gait abnormalities as observed in patients. However, we could neither detect obvious indications for achalasia such as changes of the lower esophageal sphincter nor obvious hints to assume that tear production was reduced. However, in IF stainings we detected a more blurry Laminin signal in lacrimal gland cross sections from 5-months-old KO mice suggesting mild alterations of the ECM. In addition, we detected increased signal intensities with an antibody against Paucimannose in KO mice suggesting an increased mannosylation of glycoproteins in the lacrimal gland. Increased signal intensities for Paucimannose were also evident in cross sections of the esophagus of KO mice. Signals for the glycosylation specific epitope of α-DG were increased as well. As we could not detect structural alterations in skeletal muscle before 12 months of age, one should look for structural changes in the esophagus and lacrimal glands at later stages of life. Of note, we neither performed esophageal motility studies nor assessed tear production, two methods that are used to assess esophageal and lacrimal gland function in human patients, because of technical limitations.

In accordance with the clinical presentation of human patients (Koehler et al. 2013, Gold et al. 2017, Benítez et al. 2018), *Gmppa* KO mice display cognitive defects. In mice, these deficits include decreased freezing times in the *cued* and *context fear conditioning* test and decreased field excitatory postsynaptic potentials in LTP measurements. These learning and memory difficulties often reflect structural and functional brain alterations. Indeed, we found an increased amount of activated astrocytes, indicated by increased GFAP signals, and a reduction of the thickness of cortical layers in 3-months-old KO mice. This may either indicate neuron loss or a decreased neurogenesis in development. In addition, we observed a smaller size of the cerebellum and fewer pyramidal neurons in the CA3 region of the hippocampus in KO animals. Consistent with this notion, *Gmppa* KO mice exhibited a reduced brain weight. Because we found a hyperglycosylation of α-DG in skeletal muscle, we suggest that α-DG and also other proteins which may play a role for neurogenesis or neuronal homeostasis may be hyperglycoslyated. Furthermore, as hyperglycosylation decreases the half-life of α-DG in skeletal muscle and myoblasts this may result in a decrease of overall α-DG abundance. In fact, mice lacking Dystroglycan show disarrayed cortex layering and a reduced LTP (Moore et al. 2002) similar to our findings in *Gmppa* KO mice. Patients with reduced expression of

glycosylated Dystroglycan exhibit severe brain malformations with cortical dysplasia, neuronal migration defects, epilepsy and a defect of neuromuscular transmission (Chan et al. 2010, Barišić et al. 2011, Carss et al. 2013, Engel et al. 2015). Dystroglycan-deficient mice did not show changed paired-pulse facilitation suggesting that presynaptic transmitter release was not changed. Whether this also applies for *Gmppa* KO mice is still elusive. Moreover, several studies showed that abnormal glycosylation during brain development, especially *O*-mannosylation, can lead to severe cognitive impairment (Freeze et al. 2012, Liu et al. 2006). In conclusion, whether GMPPA has a function in brain development is still unclear,but it appears likely.

Similar to human patients with *GMPPA* mutations (Koehler et al. 2013, Gold et al. 2017, Benítez et al. 2018), *Gmppa* KO mice show gait abnormalities. Notably, these gait abnormalities become more severe with age and are accompanied by a progressive muscle weakness. *Gmppa* KO mice show a significantly decreased muscle weight compared to WT littermates. In addition, we found more centralized nuclei and a reduced fiber diameter in skeletal muscle tissue of aged KO mice, altogether indicating a myopathy. Thus, gait abnormalities in patients may be also related to a skeletal muscle pathology.

Notably, ECM proteins, e.g. Laminin, showed a more clustered and disrupted distribution pointing to a reorganization of the ECM upon *Gmppa* disruption. This does not dramatically impair sarcolemma stability as shown by the lack of intracellular IgG deposits in skeletal muscle section of aged KO mice. To further assess whether the ECM alterations affect the stability of the sarcolemma, it would be interesting to assess skeletal muscle viability under challenged conditions, e.g. after forced running on a treadmill. Interestingly, the protein abundance of the Z-disc protein CAPZB was reduced and the distribution of the Z-disc protein α-Actinin was altered in KO mice. As the sarcomere and the ECM are important for force generation and contractility, it would be of great interest to perform force measurements on isolated muscle fibers. Importantly, histological examinations of skeletal muscle specimen obtained from two AAMR patients with *GMPPA* mutations (Benitez et al. 2018) confirmed these findings.

To exclude a neurogenic origin of the observed myopathy, we measured SSAPs and CMAPs in response to electrical stimulation of peripheral nerves in WT and KO mice. SSAPs and CMAPs were not changed between genotypes arguing against a neurogenic component. Moreover, we could not detect any structural differences of sciatic nerves between genotypes by electron microscopy. These findings indicate that the observed muscle phenotype likely is

skeletal muscle intrinsic. Of note, we did not look for SSAPs and CMAPs or at the sciatic nerve morphology at later stages of life.

Molecular mechanisms underlying AAMR syndrome

AAMR patients have elevated GDP-mannose levels in lymphoblastoid cells (Koehler et al. 2013). In agreement with this, we found increased GDP-mannose levels in several tissues of *Gmppa* KO mice including skeletal muscle.

It has been reported that low GDP-mannose levels correlate with low serum mannose levels (Sharma et al. 2014). As we found elevated GDP-mannose levels in *Gmppa* KO mice, we wondered whether we will find elevated serum mannose levels in KO mice. Indeed, *Gmppa* KO mice displayed increased serum mannose levels. Potentially, elevated serum mannose levels result from mannose release from the degradation of hypermannosylated proteins.

Of note, glucose and mannose are taken up into the cell by the same transporter molecules (Thorens and Mueckler 2010) and thus increased mannose levels may impair glucose uptake into the cell and thus glucose metabolism (Gonzalez et al. 2018).

Interestingly, serum glucose levels were decreased in KO mice. In accordance with reduced serum glucose levels in KO mice, we found an increased abundance of RSC1A1 protein by mass spectrometry. RSC1A1 inhibits the expression of the sodium/glucose symporter by lowering its incorporation into the cell membrane at low intracellular glucose levels (Kroiss et al. 2006).

We propose that increased mannose levels in the blood of *Gmppa* KO mice may lead to an increased influx of mannose into the cells. In cells, increased mannose supply may further stimulate the generation of GDP-mannose, because control of GMPPB by GMPPA is missing leading to hyperglycosylation of proteins and lipids. Hyperglycosylation might lead to protein degradation, glycan trimming and thus release of free mannose. Most of free mannose released by intracellular glycan processing exits the cells via a nocodazole-sensitive transporter into the blood (Sharma and Freeze 2011). This mannose efflux may explain elevated serum mannose levels in *Gmppa* KO mice. Intracellular released mannose cannot enter directly glycosylation again (Sharma and Freeze 2011, Sharma et al. 2014). So, if more mannose is needed due to an increased GDP-mannose generation in KO mice, it has to derive from glucose. Of note, glucose conversion into mannose is lowering the glucose pool and may explain decreased serum glucose levels.

Increased GDP-mannose levels might cause glycosylation imbalances. Notably, we observed increased reactivities for Paucimannose and Oligomannose in KO skeletal muscle lysates. The Paucimannose antibody detects three mannose residues in a "V-shaped" arrangement

and the Oligomannose antibody detects 5-9 mannose residues which are not further decorated. Thus, this approach is limited to several mannosylated proteins, but gives no insights into proteome-wide glycosylation imbalances.

In skeletal muscle of *Gmppa* KO mice and AAMR patients we also detected increased reactivities for PNA, which detects non-sialylated Gal-β(1-3)-GalNAc (Morran et al. 2017, Lotan et al. 1975), but not for Con A, which detects both α-D-mannosyl and α-D-glucosyl residues (Morran et al. 2017, Mega et al. 1992) on glycoproteins and glycolipids. Notably, the glycome analysis is consistent with an increase in high-mannose *N*-glycans and *O*-glycans carrying more than one mannose residue and less sialylated structures detected in KO lysates. Performing glycome analysis in skeletal muscle requires the absence of glycogen as it masks the relevant mass peaks in the MALDI-TOF spectra. For this purpose we had to fast the mice for 24 h before organ removal. Although glycogen levels were lowered with that protocol, still some relevant *O*-glycan peaks were masked by residual intracellular glycogen stores. We also tried to separate glycogen from other skeletal muscle proteins by SDS-PAGE prior to glycome analysis, but results were not satisfying and we are still trying to improve the protocols.

We found increased reactivities and a shift of the band to a slightly higher molecular weight with an antibody directed against the glycosylation specific epitope of α-DG, which points to the hyperglycosylation of α-DG both in *Gmppa* KO mice as well as in patients. We tried to verify the data with glycome analysis after pull-down of α-DG with WGA coupled beads. Unfortunately, obtained protein amounts were not sufficient for glycome analysis.

In accordance to previous studies (Brockington et al. 2010) we could show that α-DG hyperglycosylation leads to an increased binding of α-DG to the ECM proteins Laminin and Agrin. It has been shown that this binding depends on the repeating disaccharide [-3-xylose-alpha1,3-glucuronic acid-beta1-], which is attached by LARGE (Inamori et al. 2012, Yoshida-Moriguchi et al. 2010). LARGE mutations are reported for some forms of muscular dystrophies (Longman et al. 2003). Transgenic overexpression of LARGE in mice resulted in α-DG hyperglycosylation and thereby increased Laminin binding. Therefore, it was proposed that LARGE overexpression might be a therapeutic strategy for dystroglycanopathies (Brockington et al. 2010). In view of the myopathic phenotype of *Gmppa* KO mice, however, this strategy might come with side effects. Notably, α-DG hyperglycosylation increases its turnover and thus decreases its overall abundance, which likely contributes to the detrimental effects of the loss of GMPPA on NMJ and skeletal muscle integrity. Of note, as α-DG is heavily glycosylated under normal conditions (Stalnaker et al. 2011), hyperglycosylation of α-DG may mask the core protein epitope hindering the core α-DG of proper binding and thus

leading to decreased α-DG core protein bands in KO tissue. Therefore, de-glycosylation experiments would be of great interest.

Agrin binds to the Muscle-specific kinase (MUSK) and to α-DG, which are both critical for NMJ formation and maintenance (Barik et al. 2012). These two proteins are required for neuromuscular innervation (Lefebvre et al. 2007). Therefore, increased Agrin-binding to α-DG may reduce Agrin-binding to Musk and therefore impair MUSK signaling. Thus, the partially fragmented motor endplates in *Gmppa* KO mice may be a consequence of aberrant interaction of Dystroglycan and Agrin. Abnormalities of NMJs are a common finding especially in myopathies, which are caused by alterations of the Dystrophin-Dystroglycan complex (Gawor et al. 2018). Upon loss of Dystroglycan expression NMJs are still formed, but fail to undergo the developmental remodeling from plaque to the typical pretzel like shape in the adult (Shi et al. 2012).

Notably, α-DG hyperglycosylation decreases its protein stability and increases α-DG turnover as shown in myoblast experiments. A previous study reported that the hypoglycosylation of α-DG destabilizes the protein (Palmieri et al. 2017). In light of our data, we propose that improper glycosylation, either hypo- or hyperglycosylation, reduces α-DG protein stability.
We did not observe increased Dystroglycan retention in the ER or the Golgi due to hyperglycosylation, although Golgi marker protein abundance, such as TGN38 or GLG1 were increased in immunoblot analysis in *Gmppa* KO mice and patients suggesting an effect on the Golgi compartment. Recently, it has been reported that the Golgi compartment showed an altered distribution in Duchenne muscular dystrophy, a disease caused by disruption of Dystrophin, which interacts with Dystroglycan (Percival et al. 2007). In accordance with these findings, we could detect altered *trans*Golgi structures upon loss of GMPPA. Some CDGs are due to deficiencies in subunits of the Conserved oligomeric golgi (COG) complex affecting glycosylation in the Golgi (Zeevart et al. 2007). So, we propose that our observed changes in Golgi proteins and structure may be a direct consequence of hyperglycosylation within the Golgi and may further impact on glycosylation processes within the Golgi. Of note, we did not investigate whether these glycosylation specific Golgi alterations impact on Golgi stress and Golgi-Phagy. We neither analyzed if other ER stress-related proteins, besides BIP, are altered in *Gmppa* KO mice and if transport processes between Golgi, ER and lysosomes are affected.
Since α-DG has been shown to be part of a signal transduction pathway involving GRB2 (Russo et al. 2000), a mediator of the Ras-related signal pathway, α-DG hyperglycosylation may also activate ERK signaling thus explaining ERK activation either upon knockdown of

Gmppa in myoblasts or in *Gmppa* KO skeletal muscle lysates. Several studies reported ERK activation in skeletal muscle or myotubes during regeneration after injury. Briefly, satellite cells are activated by factors released by the muscle, enter the cell cycle, proliferate, migrate and are submitted to myogenesis. In all these processes, ERK signaling takes place (Krauss 2010, Cuenda and Cohen 1999, Yeow et al. 2002, Perdiguero et al. 2007, Segalés et al. 2016). So, ERK activation in *Gmppa* KO mice and myotubes might be due to an altered regeneration in skeletal muscle. For analysis of muscle regeneration, one might look for regeneration marker proteins, such as PAX7 or developmental MHC.

Therapeutic strategy

As patients with mutations in the gene encoding Phosphomannose Isomerase benefit from oral mannose supplementation (Niehues et al. 1998), we considered that a mannose-depleted diet might improve symptoms in *Gmppa* KO mice and patients. Mechanistically we assumed that a mannose-depleted food with reduced glucose and fructose levels will lead to a reduced amount of serum mannose resulting in lower mannose-1-phosphate levels and thus a decreased substrate amount for GMPPB leading to decreased GDP-mannose abundance. This hypothesis still needs to be further addressed by measuring tissue levels of mannose, mannose-1-phosphate and GDP-mannose.

To test our hypothesis, we fed *Gmppa* KO and WT mice with a mannose-depleted diet with a reduced amount of glucose and fructose starting at P14 up to 8 months of age. Indeed, α-DG hyperglycosylation as well as general skeletal muscle tissue hyperglycosylation, especially hypermannosylation, were almost normalized to normal levels. Motor performance and muscle strength were significantly improved and did not decline with age. Therefore, we claim that the AAMR syndrome may be a treatable condition and that the severity of clinical symptoms possibly depends on dietary habits. Whether ECM, Z-disc and NMJ alterations observed in 12-months-old *Gmppa* KO mice are corrected with a mannose-free diet for 12 months is under investigation. If initiation of the diet at a later stage of the disease shows similar effects, is as of yet unclear and requires future studies. Up to now, it is not known whether a mannose-free diet during pregnancy may be effective to prevent muscle and cognitive impairments in KO mice. We did not address if a mannose-enriched diet worsens the observed symptoms in *Gmppa* KO mice. So far, there are no studies considering whether and to which extent a mannose-free diet or a mannose-enriched diet alters glycosylation in WT mice and/or humans.

Conclusions and perspectives

We established a *Gmppa* KO mouse model to study the function of GMPPA and to elucidate the pathophysiology of AAMR syndrome.

We show that GMPPA directly interacts with the N-terminal domain of GMPPB via its C-terminal domain and that *Gmppa* KO mice as well as patients exhibit elevated GDP-mannose levels. This suggests that GMPPA might act as an allosteric feedback inhibitor of GMPPB. However, data on the allosteric feedback mechanism are still missing. GMPPB activity assays with recombinant proteins, changing GDP-mannose levels and GMPPA WT and mutant proteins will provide more insight into the potential feedback mechanism of GMPPA.

Gmppa KO mice do not show obvious signs of swallowing difficulties or reduced tear production compared to human patients. However, we do see increased mannosylation in lacrimal gland and esophageal sphincter sections as well as structural changes in the Laminin signal in the lacrimal gland. These findings suggest that disease-related events are taking place in both tissues. Future studies will elucidate whether swallowing difficulties or reduced tear production as well as structural changes appear in old (15-18 months) or geriatric (24 months) KO mice and if these symptoms are treatable with a mannose-free diet. These studies might include esophageal motility studies and assessment of tear production in mice.

Gmppa KO mice display cognitive impairments and a decreased neuronal density in the cortex. Until now, we do not know whether brain development is affected in *Gmppa* KO mice due to altered glycosylation. Future studies will focus on the GMPPA function in brain development and aging. For this purpose, Tamoxifen-inducible knockout mouse models might be useful. For instance, Tamoxifen-treatment of either adolescent or middle-aged mice will highlight developmental and age-related changes.

Loss of GMPPA leads to Golgi alterations, but does not obviously affect the ER. Since we addressed just some Golgi-associated proteins and proteins involved in ER stress, future studies might address whether and under which conditions the ER stress response as well the Golgi stress response are activated upon loss of GMPPA.

Gmppa KO mice show a progressive gait disorder with progressive muscle weakness due to protein hyperglycosylation. In addition, we demonstrated that a mannose-depleted diet rescues the observed motor phenotype and the hyperglycosylation. Up to date, we do not know whether we might rescue the observed ECM, sarcomere and NMJ alterations in skeletal muscle with a mannose-free diet. Therefore, a mannose-depleted diet for at least 12 months upon P14 is essential. Further studies might address whether a mannose-depleted diet starting at later stages of life might show a similar beneficial effect. Furthermore, it is of

great interest to study whether initiation of treatment during pregnancy will be even more effective to prevent the myopathy and possibly also cognitive defects in *Gmppa* KO mice.

Mannose supplementation may aggravate the phenotype of *Gmppa* KO mice.

Conditional KO mice would be also helpful to verify whether the observed myopathy in *Gmppa* KO mice is only due a muscle intrinsic pathology by means of a skeletal muscle-specific KO mouse using the Myf5Cre line.

As GMPPA is important for skeletal muscle function, future studies will focus on the impact of GMPPA in heart function. Until now, we did not observe premature death in *Gmppa* KO mice, but cardiac complications in CDGs have been reported (Marques-da-Silva et al. 2017).

Because AAMR patients show the same muscle alterations and cognitive impairments as *Gmppa* KO mice, future studies will address whether a mannose-free or mannose-reduced diet is also beneficial for human patients.

Finally, our findings stipulate the idea that symptoms of patients with a GMPPB-related disorder might profit from dietary mannose supplementation.

References

Aguilan JT, Sundaram S, Nieves E, Stanley P. Mutational and functional analysis of Large in a novel CHO glycosylation mutant. Glycobiology. 2009; 19:971–86. doi: 10.1093/glycob/cwp074. PMID: 19470663

Banerjee DK, Zhang Z, Baksi K, Serrano-Negrón JE. Dolichol phosphate mannose synthase: a Glycosyltransferase with Unity in molecular diversities. Glycoconj J. 2017 Aug;34(4):467-479. doi: 10.1007/s10719-017-9777-4. PMID: 28616799

Bareja A, Holt JA, Luo G, Chang C, Lin J, Hinken AC, Freudenberg JM, Kraus WE, Evans WJ, Billin AN. Human and mouse skeletal muscle stem cells: convergent and divergent mechanisms of myogenesis. PLoS One. 2014 Feb 28;9(2):e90398. doi: 10.1371/journal.pone.0090398. PMID: 24587351

Barik A, Xiong WC, and Mei L, MuSK: A Kinase Critical for the Formation and Maintenance of the Neuromuscular Junction. J Clin Invest. 2013 Dec;123(12):5190-202. doi: 10.1172/JCI66039. PMID: 24200689

Barišić N, Chaouch A, Müller JS, Lochmüller H. Genetic heterogeneity and pathophysiological mechanisms in congenital myasthenic syndromes. Eur J Paediatr Neurol. 2011 May;15(3):189-96. doi: 10.1016/j.ejpn.2011.03.006. PMID: 21498094

Bartels MF, Winterhalter PR, Yu J, Liu Y, Lommel M, Möhrlen F, Hu H, Feizi T, Westerlind U, Ruppert T, Strahl S. Protein O-Mannosylation in the Murine Brain: Occurrence of Mono-O-Mannosyl Glycans and Identification of New Substrates. PLoS One. 2016 Nov 3;11(11):e0166119. doi: 10.1371/journal.pone.0166119. PMID: 27812179

Baudys M, Uchio T, Mix D, Wilson D, Kim SW. Physical stabilization of insulin by glycosylation. J Pharm Sci. 1995 Jan;84(1):28-33. doi:10.1002/jps.2600840108. PMID: 7714739

Benítez EO, Morales JJ, Muñoz LA, Hübner CA, Mutchinick OM. A Novel GMPPA Mutation in Two Adult Sisters with Achalasia, Alacrima, Short Stature, Dysmorphism, and Intellectual Disability. Mol Syndromol. 2018 Feb;9(2):110-114. doi: 10.1159/000485908. PMID: 29593478

Bennett EP, Mandel U, Clausen H, Gerken TA, Fritz TA, Tabak LA. Control of mucin-type O-glycosylation: A classification of the polypeptide GalNAc-transferase gene family. Glycobiology 22: 736-756. doi: 10.1093/glycob/cwr182. PMID: 22183981

Braitenberg V, Atwood RP. Morphological observations on the cerebellar cortex. J Comp Neurol. 1958 Feb;109(1):1-33. PMID: 13563670

Bravo R, Parra V, Gatica D, Rodriguez AE, Torrealba N, Paredes F, Wang ZV, Zorzano A, Hill JA, Jaimovich E, Quest AF, Lavandero S. Endoplasmic reticulum and the unfolded protein response: dynamics and metabolic integration. Int Rev Cell Mol Biol. 2013; 301:215-90. doi: 10.1016/B978-0-12-407704-1.00005-1. PMID: 23317820

Breloy I, Hanisch FG. Functional Roles of O-Glycosylation. Molecules. 2018 Nov 23;23(12). pii: E3063. doi: 10.3390/molecules23123063. PMID: 30477085

Brockington M, Torelli S, Prandini P, Boito C, Dolatshad NF, Longman C, Brown SC, Muntoni F. Localization and functional analysis of the LARGE family of glycosyltransferases: significance for muscular dystrophy. Hum Mol Genet. 2005 Mar 1;14(5):657-65. doi: 10.1093/hmg/ddi062. PMID: 15661757

Brockington M, Torelli S, Sharp PS, Liu K, Cirak S, Brown SC, Wells DJ, Muntoni F. Transgenic overexpression of LARGE induces α-dystroglycan hyperglycosylation in skeletal and cardiac muscle. PLoS One. 2010 Dec 28;5(12):e14434. doi: 10.1371/journal.pone.0014434. PMID: 21203384

Brosch M, Yu L, T. Hubbard, J. Choudhary, Accurate and sensitive peptide identification with Mascot Percolator. J Proteome Res. 2009 Jun;8(6):3176-81. doi: 10.1021/pr800982s. PMID: 19338334

Cantagrel V, Lefeber DJ. From glycosylation disorders to dolichol biosynthesis defects: a new class of metabolic diseases. J Inherit Metab Dis. 2011 Aug;34(4):859-67. doi: 10.1007/s10545-011-9301-0. PMID: 21384228

Carss KJ, Stevens E, Foley AR, Cirak S, Riemersma M, Torelli S, et al. Mutations in GDP-mannose pyrophosphorylase B cause congenital and limb-girdle muscular dystrophies

associated with hypoglycosylation of α-dystroglycan. Am J Hum Genet. 2013;93:29–41. doi: 10.1016/j.ajhg.2013.05.009. PMID: 23768512

Chan YM, Keramaris-Vrantsis E, Lidov HG, Norton JH, Zinchenko N, Gruber HE, Thresher R, Blake DJ, Ashar J, Rosenfeld J, Lu QL. Fukutin-related protein is essential for mouse muscle, brain and eye development and mutation recapitulates the wide clinical spectrums of dystroglycanopathies. Hum Mol Genet. 2010 Oct 15;19(20):3995-4006. doi: 10.1093/hmg/ddq314. PMID: 20675713

Cohen NJ, Ryan J, Hunt C, Romine L, Wszalek T, Nash C. Hippocampal system and declarative (relational) memory: Summarizing the data from functional neuroimaging studies. Hippocampus. 1999;9(1):83-98. doi: 10.1002/(SICI)1098-1063(1999)9:1<83::AID-HIPO9>3.0.CO;2-7. PMID: 10088903

Cuenda A, Cohen P. Stress-activated protein kinase-2/p38 and a rapamycin-sensitive pathway are required for C2C12 myogenesis. J Biol Chem. 1999 Feb 12;274(7):4341-6. doi: 10.1074/jbc.274.7.4341. PMID: 9933636

Deacon. Measuring the strength of mice. J Vis Exp. 2013; (76): 2610. doi: 10.3791/2610. PMID: 23770643

Deyst KA, Bowe MA, Leszyk JD, Fallon JR. The alpha-dystroglycan-beta-dystroglycan complex. Membrane organization and relationship to an agrin receptor. J Biol Chem. 1995 Oct 27;270(43):25956-9. PMID: 7592785

Di Stasio E, Sciandra F, Maras B, Di Tommaso F, Petrucci TC, Giardina B, Brancaccio A. Structural and functional analysis of the N-terminal extracellular region of beta-dystroglycan. Biochem Biophys Res Commun. 1999 Dec 9;266(1):274-8. PMID: 10581202

Dobson CM, Hempel SJ, Stalnaker SH, Stuart R, Wells L. O-Mannosylation and human disease. Cell Mol Life Sci. 2013 Aug;70(16):2849-57. doi: 10.1007/s00018-012-1193-0. PMID: 23115008

Endo T. Glycobiology of α-dystroglycan and muscular dystrophy. J. Biochem. Volume 157, Issue 1, 1 January 2015, Pages 1–12. doi: 10.1093/jb/mvu066. PMID: 25381372

Endo T. Mammalian O-mannosyl glycans: Biochemistry and glycopathology. Proc Jpn Acad Ser B Phys Biol Sci. 2019;95(1):39-51. doi: 10.2183/pjab.95.004. PMID: 30643095

Engel AG, Shen XM, Selcen D, Sine SM;. Congenital myasthenic syndromes: pathogenesis, diagnosis, and treatment. Lancet Neurol. 2015 Apr; 14(4): 420–434. doi: 10.1016/S1474-4422(14)70201-7. PMID: 25792100

Ervasti JM, Campbell KP. A role for the dystrophin-glycoprotein complex as a transmembrane linker between laminin and actin. J Cell Biol. 1993 Aug;122(4):809-23. doi: 10.1083/jcb.122.4.809. PMID: 8349731

Ervasti JM, Burwell AL, Geissler AL. Tissue-specific heterogeneity in alpha-dystroglycan sialoglycosylation. Skeletal muscle alpha-dystroglycan is a latent receptor for Vicia villosa agglutinin b4 masked by sialic acid modification. J Biol Chem. 1997;272:22315–22321. doi: 10.1074/jbc.272.35.22315. PMID: 9268382

Esapa CT, Bentham GR, Schröder JE, Kröger S, Blake DJ. The effects of post-translational processing on dystroglycan synthesis and trafficking. FEBS Lett. 2003 Dec 4;555(2):209-16. doi: 10.1016/s0014-5793(03)01230-4. PMID: 14644417

Esser AK, Miller MR, Huang Q, Meier MM, Beltran-Valero de Bernabé D, Stipp CS, Campbell KP, Lynch CF, Smith BJ, Cohen MB, Henry MD. Loss of LARGE2 disrupts functional glycosylation of α-dystroglycan in prostate cancer. J Biol Chem. 2013 Jan 25;288(4):2132-42. doi: 10.1074/jbc.M112.432807. PMID: 23223448

Fanselow MS, Poulos AM. 2005. The neuroscience of mammalian associative learning. Annu Rev Psychol. 2005;56:207-34. doi: 10.1146/annurev.psych.56.091103.070213. PMID: 15709934

Freeze HH, Eklund EA, Ng BG, Patterson MC. Neurology of inherited glycosylation disorders. Lancet Neurol. 2012 May;11(5):453-66. doi: 10.1016/S1474-4422(12)70040-6. PMID: 22516080

Holzfeind PJ, Grewal PK, Reitsamer HA, Kechvar J, Lassmann H, Hoeger H, Hewitt J, Bittner, RE. Skeletal, cardiac and tongue muscle pathology, defective retinal transmission,

and neuronal migration defects in the Large myd mouse. Hum. Mol. Genet. 2002,11,2673–2687. doi: 10.1093/hmg/11.21.2673. PMID: 12354792

Freeze HH, Chong JX, Bamshad MJ, . Ng BG. Solving Glycosylation Disorders: Fundamental Approaches Reveal Complicated Pathways. Am J Hum Genet. 2014 Feb 6; 94(2): 161–175. doi: 10.1016/j.ajhg.2013.10.024. PMID: 24507773

Frontera and Ochalo. Skeletal Muscle: A Brief Review of Structure and Function. Calcified Tissue International · October 2014. doi: 10.1007/s00223-014-9915-y. PMID: 25294644

Gawor M, Prószyński TJ. The molecular cross talk of the dystrophin-glycoprotein complex. Ann N Y Acad Sci. 2018 Jan;1412(1):62-72. doi: 10.1111/nyas.13500. Epub 2017 Oct 25. PMID: 29068540

Gold WA, Sobreira N, Wiame E, Marbaix A, Van Schaftingen E, Franzka P, Riley LG, Worgan L, Hübner CA, Christodoulou J, Adès LC. A novel mutation in GMPPA in siblings with apparent intellectual disability, epilepsy, dysmorphism, and autonomic dysfunction. Am J Med Genet A. 2017 Aug;173(8):2246-2250. doi: 10.1002/ajmg.a.38292. PMID: 28574218

Gee SH, Blacher RW, Douville PJ, Provost PR, Yurchenco PD, Carbonetto S. Laminin-binding protein 120 from brain is closely related to the dystrophin-associated glycoprotein, dystroglycan, and binds with high affinity to the major heparin binding domain of laminin. J Biol Chem. 1993 Jul 15;268(20):14972-80. PMID: 8325873

Gonzalez PS, O'Prey J, Cardaci S, Barthet VJA, Sakamaki JI, Beaumatin F, Roseweir A, Gay DM, Mackay G, Malviya G, Kania E, Ritchie S, Baudot AD, Zunino B, Mrowinska A, Nixon C, Ennis D, Hoyle A, Millan D, McNeish IA, Sansom OJ, Edwards J, Ryan KM. Mannose impairs tumour growth and enhances chemotherapy. Nature. 2018 Nov;563(7733):719-723. doi: 10.1038/s41586-018-0729-3. PMID: 30464341

Grady RM, Grange RW, Lau KS, Maimone MM, Nichol MC, Stull JT, Sanes JR. Role for alpha-dystrobrevin in the pathogenesis of dystrophin-dependent muscular dystrophies. Nat. Cell Biol. 1999 1, 215-220. PMID: 10559919

Heinze I, Bens M, Calzia E, Holtze S, Dakhovnik O, Sahm A, Kirkpatrick JM, Szafranski K, Romanov N, Holzer K, Singer S, Ermolaeva M, Platzer M, Hildebrandt T, Ori A. Species comparison of liver proteomes reveals links to naked mole-rat longevity and human aging. BMC Biol. 2018 Aug 2;16(1):82. doi: 10.1186/s12915-018-0547-y. PMID: 30068331

Hikida RS. Aging changes in satellite cells and their functions. Curr Aging Sci. 2011 Dec;4(3):279-97. PMID: 21529324

Hirai KE, de Sousa JR, Silva LM, Junior LBD, Furlaneto IP, Carneiro FRO, de Souza Aarão TL, Sotto MN, Quaresma JAS. Endoplasmic Reticulum Stress Markers and Their Possible Implications in Leprosy's Pathogenesis. Dis Markers. 2018 Dec 16;2018:7067961. doi: 10.1155/2018/7067961. PMID: 30647798

Inamori K, Yoshida-Moriguchi T, Hara Y, Anderson ME, Yu L, Campbell KP. Dystroglycan function requires xylosyl- and glucuronyltransferase activities of LARGE. Science. 2012 Jan 6;335(6064):93-6. doi: 10.1126/science.1214115. PMID: 22223806

Irintchev A, Simova O, Eberhardt KA, Morellini F, Schachner M. Impacts of lesion severity and tyrosine kinase receptor B deficiency on functional outcome of femoral nerve injury assessed by a novel single-frame motion analysis in mice. Eur J Neurosci. 2005 Aug;22(4):802-8. doi: 10.1111/j.1460-9568.2005.04274.x. PMID: 16115204

Jaeken J. Congenital disorders of glycosylation. Handb Clin Neurol. 2013;113:1737-43. doi: 10.1016/B978-0-444-59565-2.00044-7. PMID: 23622397

Jin X, Ballicora MA, Preiss J, Geiger JH. Crystal structure of potato tuber ADP-glucose pyrophosphorylase. EMBO J. 2005 Feb 23;24(4):694-704. doi: 10.1038/sj.emboj.7600551. PMID: 15692569

Jung D, Yang B, Meyer J, Chamberlain JS, Campbell KP. Identification and characterization of the dystrophin anchoring site on beta-dystroglycan. J Biol Chem. 1995 Nov 10;270(45):27305-10. PMID: 7592992

Kanagawa M, Saito F, Kunz S, Yoshida-Moriguchi T, Barresi R, Kobayashi YM, Muschler J, Dumanski JP, Michele DE, Oldstone MB and Campbell KP. Molecular recognition by LARGE

is essential for expression of functional dystroglycan. Cell. 2004 Jun 25;117(7):953-64. doi: 10.1016/j.cell.2004.06.003. PMID: 15210115

Kinoshita T, Inoue N. Dissecting and manipulating the pathway for glycosylphos-phatidylinositol-anchor biosynthesis. Curr Opin Chem Biol. 2000 Dec;4(6):632-8. PMID: 11102867

Koehler K, Malik M, Mahmood S, Gießelmann S, Beetz C, Hennings JC, Huebner AK, Grahn A, Reunert J, Nürnberg G, Thiele H, Altmüller J, Nürnberg P, Mumtaz R, Babovic-Vuksanovic D, Basel-Vanagaite L, Borck G, Brämswig J, Mühlenberg R, Sarda P, Sikiric A, Anyane-Yeboa K, Zeharia A, Ahmad A, Coubes C, Wada Y, Marquardt T, Vanderschaeghe D, Van Schaftingen E, Kurth I, Huebner A, Hübner CA. Mutations in GMPPA cause a glycosylation disorder characterized by intellectual disability and autonomic dysfunction. Am J Hum Genet. 2013 Oct 3;93(4):727-34. doi: 10.1016/j.ajhg.2013.08.002. PMID: 24035193

Krauss RS. Regulation of promyogenic signal transduction by cell-cell contact and adhesion. Exp Cell Res. 2010 Nov 1; 316(18): 3042–3049. doi: 10.1016/j.yexcr.2010.05.008. PMID: 20471976

Kroiss M, Leyerer M, Gorboulev V, Kühlkamp T, Kipp H, Koepsell H. Transporter regulator RS1 (RSC1A1) coats the trans-Golgi network and migrates into the nucleus. American Journal of Phisiology. 2006. doi.org/10.1152/ajprenal.00067.2006

Lefebvre JL, Jing L, Becaficco S, Franzini-Armstrong C, Granato M. Differential requirement for MuSK and dystroglycan in generating patterns of neuromuscular innervation. PNAS February 13, 2007 104 (7) 2483-2488. doi: 10.1073/pnas.0610822104. PMID: 17284594

Liu J, Ball SL, Yang Y, Mei P, Zhang L, Shi H, Kaminski HJ, Lemmon VP, Hu H. A genetic model for muscle-eye-brain disease in mice lacking protein O-mannose 1,2-N-acetylglucosaminyltransferase (POMGnT1). Mech Dev. 2006 Mar;123(3):228-40. doi: 10.1016/j.mod.2005.12.003. PMID: 16458488

Longman C, Brockington M, Torelli S, Jimenez-Mallebrera C, Kennedy C, Khalil N, Feng L, Saran RK, Voit T, Merlini L, Sewry CA, Brown SC, Muntoni F. Mutations in the human LARGE gene cause MDC1D, a novel form of congenital muscular dystrophy with severe

mental retardation and abnormal glycosylation of alpha-dystroglycan. Hum Mol Genet. 2003 Nov 1;12(21):2853-61. doi: 10.1093/hmg/ddg307. PMID: 12966029

Lotan R, Skutelsky E, Danon D, Sharon N. 1975. The purification, composition, and specificity of the anti-T lectin from peanut (Arachis hypogaea). J Biol Chem. 1975 Nov 10;250(21):8518-23. PMID: 811657

Macaluso F, Myburgh KH. Current evidence that exercise can increase the number of adult stem cells. J Muscle Res Cell Motil. 2012 Aug;33(3-4):187-98. doi: 10.1007/s10974-012-9302-0. PMID: 22673936

Marques-da-Silva D, Francisco R, Webster D, Dos Reis Ferreira V, Jaeken J, Pulinilkunnil T. Cardiac complications of congenital disorders of glycosylation (CDG): a systematic review of the literature. J Inherit Metab Dis. 2017 Sep;40(5):657-672. doi: 10.1007/s10545-017-0066-y. PMID: 28726068

Martin PT. Dystroglycan glycosylation and its role in matrix binding in skeletal muscle. Glycobiology. 2003 Aug;13(8):55R-66R. doi: 10.1093/glycob/cwg076. PMID:12736199

Martínez-Duncker I, Díaz-Jímenez DF, Mora-Montes HM. Comparative Analysis of Protein Glycosylation Pathways in Humans and the Fungal Pathogen Candida albicans. Int J Microbiol. 2014;2014:267497. doi: 10.1155/2014/267497. PMID: 25104959

McAlister GC, Nusinow DP, Jedrychowski MP, Wühr M, Huttlin EL, Erickson BK, Rad R, Haas W, Gygi SP. MultiNotch MS3 enables accurate, sensitive, and multiplexed detection of differential expression across cancer cell line proteomes. Anal Chem. 2014 Jul 15;86(14):7150-8. doi: 10.1021/ac502040v. PMID: 24927332

McMorran BJ, Miceli MC, Baum LG. Lectin-binding characterizes the healthy human skeletal muscle glycophenotype and identifies disease-specific changes in dystrophic muscle. Glycobiology. 2017 Dec 1;27(12):1134-1143. doi: 10.1093/glycob/cwx073. PMID: 28973355

Mega T, Oku H, Hase S. Characterization of carbohydrate-binding specificity of concanavalin A by competitive binding of pyridylamino sugar chains. J Biochem. 1992 Mar;111(3):396-400. PMID: 1587804

Michele DE, Kabaeva Z, Davis SL, Weiss RM, Campbell KP. Dystroglycan matrix receptor function in cardiac myocytes is important for limiting activity-induced myocardial damage. Circ Res. 2009;105:984–993. doi: 10.1161/CIRCRESAHA.109.199489. PMID: 19797173

Moore SA, Saito F, Chen J, Michele DE, Henry MD, Messing A, Cohn RD, Ross-Barta SE, Westra S, Williamson RA, Hoshi T, Campbell KP. Deletion of brain dystroglycan recapitulates aspects of congenital muscular dystrophy. Nature. 2002 Jul 25;418(6896):422-5. doi: 10.1038/nature00838. PMID: 12140559

Niehues R, Hasilik M, Alton G, Körner C, Schiebe-Sukumar M, Koch HG, Zimmer KP, Wu R, Harms E, Reiter K, von Figura K, Freeze HH, Harms HK, Marquardt T. Carbohydrate-deficient glycoprotein syndrome type Ib. Phosphomannose isomerase deficiency and mannose therapy. J Clin Invest. 1998 Apr 1;101(7):1414-20. PMID: 9525984

Ning B, Elbein AD. Cloning, expression and characterization of the pig liver GDP-mannose pyrophosphorylase. Evidence that GDP-mannose and GDP-Glc pyrophosphorylases are different proteins. Eur J Biochem. 2000 Dec;267(23):6866-74. doi: 10.1046/j.1432-1033.2000.01781.x. PMID: 11082198

Palmieri V, Bozzi M, Signorino G, Papi M, De Spirito M, Brancaccio A, Maulucci G, Sciandra F. α-Dystroglycan hypoglycosylation affects cell migration by influencing β-dystroglycan membrane clustering and filopodia length: A multiscale confocal microscopy analysis. Biochim Biophys Acta Mol Basis Dis. 2017 Sep;1863(9):2182-2191. doi: 10.1016/j.bbadis.2017.05.025. PMID: 28572004

Patnaik SK, Stanley P. Mouse large can modify complex N- and mucin O-glycans on alphadystroglycan to induce laminin binding. The Journal of biological chemistry. 2005; 280:20851–9. doi: 10.1074/jbc.M500069200 PMID: 15788414

Péanne R, de Lonlay P, Foulquier F, Kornak U, Lefeber DJ, Morava E, Pérez B, Seta N, Thiel C, Van Schaftingen E, Matthijs G, Jaeken J. Congenital disorders of glycosylation (CDG): Quo vadis? Eur J Med Genet. 2018 Nov;61(11):643-663. doi: 10.1016/j.ejmg.2017.10.012. PMID: 29079546

Percival JM, Gregorevic P, Odom GL, Banks GB, Chamberlain JS, Froehner SC. rAAV6-microdystrophin rescues aberrant Golgi complex organization in mdx skeletal muscles. Traffic. 2007 Oct;8(10):1424-39. doi: 10.1111/j.1600-0854.2007.00622.x. PMID:17714427

Perdiguero E, Ruiz-Bonilla V, Serrano AL, Munoz-Canoves P. Genetic deficiency of p38alpha reveals its critical role in myoblast cell cycle exit: the p38alpha-JNK connection. Science. 2006 Jul 28;313(5786):533-6. doi: 10.1126/science.1127677. PMID: 16873666

Ritchie ME, Phipson B, Wu D, Hu Y, Law CW, Shi W, Smyth GK. Limma powers differential expression analyses for RNA-sequencing and microarray studies. Nucleic Acids Res. 2015 Apr 20;43(7):e47. doi: 10.1093/nar/gkv007. PMID: 25605792

Rodríguez CI, Buchholz F, Galloway J, Sequerra R, Kasper J, Ayala R, Stewart AF, Dymecki SM. High-efficiency deleter mice show that FLPe is an alternative to Cre-loxP. Nat Genet. 2000 Jun;25(2):139-40. doi: 10.1038/75973. PMID: 10835623

Russo K, Di Stasio E, Macchia G, Rosa G, Brancaccio A, Petrucci TC. Characterization of the beta-dystroglycan-growth factor receptor 2 (Grb2) interaction. Biochem Biophys Res Commun. 2000 Jul 21;274(1):93-8. doi:10.1006/bbrc.2000.3103. PMID: 10903901

Schmitz-Hübsch T, du Montcel ST, Baliko L, Berciano J, Boesch S, Depondt C, Giunti P. Scale for the assessment and rating of ataxia: development of a new clinical scale Neurology. 2006 Jun 13;66(11):1717-20. doi: 10.1212/01.wnl.0000219042.60538.92. PMID: 16769946

Schwenk F, Baron U, Rajewsky K. A cre-transgenic mouse strain for the ubiquitous deletion of loxP-flanked gene segments including deletion in germ cells. Nucleic Acids Res. 1995 Dec 25;23(24):5080-1. doi: 10.1093/nar/23.24.5080. PMID:8559668

Segalés J, Perdiguero E, Muñoz-Cánoves P. Regulation of Muscle Stem Cell Functions: A Focus on the p38 MAPK Signaling Pathway. Front Cell Dev Biol. 2016 Aug 30;4:91. doi: 10.3389/fcell.2016.00091. PMID: 27626031

Sharma V and Freeze HH. Mannose Efflux from the Cells A POTENTIAL SOURCE OF MANNOSE IN BLOOD. J Biol Chem. 2011 Mar 25; 286(12): 10193–10200. doi: 10.1074/jbc.M110.194241. PMID: 21273394

Sharma V, Ichikawa M, Freeze HH. MANNOSE METABOLISM: MORE THAN MEETS THE EYE. Biochem Biophys Res Commun. 2014 Oct 17; 453(2): 220–228. doi: 10.1016/j.bbrc.2014.06.021. PMID: 24931670

Shi L, Fu AK, Ip NY. Molecular mechanisms underlying maturation and maintenance of the vertebrate neuromuscular junction. Trends Neurosci. 2012 Jul;35(7):441-53. doi: 10.1016/j.tins.2012.04.005. PMID: 22633140

Shipp S. Structure and function of the cerebral cortex. Curr Biol. 2007 Jun 19;17(12):R443-9. doi: 10.1016/j.cub.2007.03.044. PMID: 17580069

Smith DR, Gallagher M, Stanton ME. Genetic background differences and nonassociative effects in mouse trace fear conditioning. Learn Mem. 2007 14, 597-605. doi: 10.1101/lm.614807. PMID: 17823243

Spiro RG. Protein glycosylation: nature, distribution, enzymatic formation, and disease implications of glycopeptide bonds. Glycobiology. 2002 Apr;12(4):43R-56R. doi: 10.1093/glycob/12.4.43r. PMID: 12042244

Stalnaker SH, Stuart R, Wells L. Mammalian O-mannosylation: unsolved questions of structure/function. Curr. Opin. Struct. Biol. 2011b;21:603–609. doi: 10.1016/j.sbi.2011.09.001. PMID: 21945038

Stanley P, Schachter H, Taniguchi N. Chapter 8 N-glycans. Essentials of Glycobiology. 2nd edition. Cold Spring Harbor (NY): Cold Spring Harbor Laboratory Press; 2009. https://www.ncbi.nlm.nih.gov/books/NBK1917/

Sugiyama J, Bowen DC, Hall ZW. Dystroglycan binds nerve and muscle agrin. Neuron. 1994 Jul;13(1):103-15. PMID: 8043271

Szumilo T, Drake RR, York JL, Elbein AD. GDP-mannose pyrophosphorylase. Purification to homogeneity, properties, and utilization to prepare photoaffinity analogs. J Biol Chem. 1993 Aug 25;268(24):17943-50. PMID: 7688733

Thorens B, Mueckler M. Glucose transporters in the 21st Century. Am J Physiol Endocrinol Metab. 2010 Feb;298(2):E141-5. doi: 10.1152/ajpendo.00712.2009. PMID: 20009031

Traini M, Kumaran R, Thaysen-Andersen M, Kockx M, Jessup W, Kritharides L. N-glycosylation of human sphingomyelin phosphodiesterase acid-like 3A (SMPDL3A) is essential for stability, secretion and activity. Biochem J. 2017 Mar 8;474(7):1071-1092. doi: 10.1042/BCJ20160735. PMID: 28104755

Vasconcelos-Dos-Santos A, Oliveira IA, Lucena MC, Mantuano NR, Whelan SA, Dias WB, Todeschini AR. Biosynthetic Machinery Involved in Aberrant Glycosylation: Promising Targets for Developing of Drugs Against Cancer. Front Oncol. 2015 Jun 25;5:138. doi: 10.3389/fonc.2015.00138. eCollection 2015. PMID: 26161361

Wu X, Steet RA, Bohorov O, Bakker J, Newell J, Krieger M, Spaapen L, Kornfeld S, Freeze, HH. Mutation of the COG complex subunit gene COG7 causes a lethal congenital disorder. Nat Med. 2004 May;10(5):518-23. doi: 10.1038/nm1041. PMID: 15107842

Wible. Hippocampal Physiology, Structure and Function and the Neuroscience of Schizophrenia: A Unified Account of Declarative Memory Deficits, Working Memory Deficits and Schizophrenic Symptoms. Behav Sci (Basel). 2013 Jun; 3(2): 298–315. doi: 10.3390/bs3020298. PMID: 25379240

Wilkins JT, Krivickas LS, Goldstein R, Suh D, Frontera WR. Contractile properties of adjacent segments of single human muscle fibers. Muscle Nerve. 2001 Oct;24(10):1319-26. PMID: 11562911

Wong CH. Protein glycosylation: new challenges and opportunities. J Org Chem. 2005 May 27;70(11):4219-25. doi: 10.1021/jo050278f. PMID: 15903293

Yeow K, Cabane C, Turchi L, Ponzio G, Dérijard B. Increased MAPK signaling during in vitro muscle wounding. Biochem Biophys Res Commun. 2002 Apr 26;293(1):112-9. doi: 10.1016/S0006-291X(02)00190-0. PMID: 12054571

Yoshida-Moriguchi T, Yu L, Stalnaker SH, Davis S, Kunz S, Madson M, Oldstone MB, Schachter H, Wells L, Campbell KP. O-mannosyl phosphorylation of alpha-dystroglycan is required for laminin binding. Science. 2010 Jan 1;327(5961):88-92. doi: 10.1126/science.1180512. PMID: 20044576

Yoshida-Moriguchi T, Campbell KP. Matriglycan: a novel polysaccharide that links dystroglycan to the basement membrane. Glycobiology 2015 25, 702–713. doi: 10.1093/glycob/cwv021. PMID: 25882296

Zeevaert R, Foulquier F, Jaeken J, Matthijs G. Deficiencies in subunits of the Conserved Oligomeric Golgi (COG) complex define a novel group of Congenital Disorders of Glycosylation. Mol Genet Metab. 2008 Jan;93(1):15-21. Epub 2007 Sep 29. doi: 10.1016/j.ymgme.2007.08.118. PMID: 17904886

Ehrenwörtliche Erklärung

Hiermit erkläre ich, dass mir die Promotionsordnung der Medizinischen Fakultät der Friedrich-Schiller-Universität bekannt ist,

ich die Dissertation selbst angefertigt habe und alle von mir benutzten Hilfsmittel, persönlichen Mitteilungen und Quellen in meiner Arbeit angegeben sind,

mich folgende Personen bei der Auswahl und Auswertung des Materials sowie bei der Herstellung des Manuskripts unterstützt haben: Prof. Dr. Christian Hübner, Prof. Dr. Otmar Huber, Prof. Dr. Rüdiger Horstkorte, Prof. Dr. Ingo Kurth, Dr. Sonnhild Mittag, Dr. Julia von Maltzahn, Dr. Juliane Jung, Dr. Lutz Liebmann, Dr. Christopher Hennings, Tanja Herrmann, Henriette Henze, Svenja Schüler, Katrin Buder, Katrin Schorr, Johanna Fischer und Sebastian Gießelmann.

die Hilfe eines Promotionsberaters nicht in Anspruch genommen wurde und dass Dritte weder unmittelbar noch mittelbar geldwerte Leistungen von mir für Arbeiten erhalten haben, die im Zusammenhang mit dem Inhalt der vorgelegten Dissertation stehen,

dass ich die Dissertation noch nicht als Prüfungsarbeit für eine staatliche oder andere wissenschaftliche Prüfung eingereicht habe und,

dass ich die gleiche, eine in wesentlichen Teilen ähnliche oder eine andere Abhandlung nicht bei einer anderen Hochschule als Dissertation eingereicht habe.

Ort, Datum   Unterschrift des Verfassers

In Gedenken an

Irmgard Schwarze,

Werner Franzka

und

Klaus Thiergart